LBNL-44865

ERNEST ORLANDO LAWRENCE
BERKELEY NATIONAL LABORATORY

The High Temperature Superconductor $YBa_2Cu_3O_{7-\delta}$: Symmetry of the Order Parameter, and Gradiometers for Biomagnetic Applications

Konstantin A. Kouznetsov

Materials Sciences Division

December 1999

Ph.D. Thesis

LOAN COPY
Circulates
For 4 weeks

7th Street Warehouse
Lawrence Berkeley National Laboratory

LBNL-44865

Copy 2

DISCLAIMER

This document was prepared as an account of work sponsored by the United States Government. While this document is believed to contain correct information, neither the United States Government nor any agency thereof, nor the Regents of the University of California, nor any of their employees, makes any warranty, express or implied, or assumes any legal responsibility for the accuracy, completeness, or usefulness of any information, apparatus, product, or process disclosed, or represents that its use would not infringe privately owned rights. Reference herein to any specific commercial product, process, or service by its trade name, trademark, manufacturer, or otherwise, does not necessarily constitute or imply its endorsement, recommendation, or favoring by the United States Government or any agency thereof, or the Regents of the University of California. The views and opinions of authors expressed herein do not necessarily state or reflect those of the United States Government or any agency thereof or the Regents of the University of California.

LBNL-44865

The High Temperature Superconductor $YBa_2Cu_3O_{7-\delta}$: Symmetry of the Order Parameter, and Gradiometers for Biomagnetic Applications

Konstantin Alexander Kouznetsov
(Ph.D. Thesis)

Department of Physics
University of California, Berkeley

and

Materials Sciences Division
Ernest Orlando Lawrence Berkeley National Laboratory
University of California
Berkeley, California 94720

December 1999

This work was supported by the Director, Office of Science, Office of Basic Energy Sciences, Materials Sciences Division, of the U.S. Department of Energy under Contract No. DE-AC03-76SF00098.

The High Temperature Superconductor $YBa_2Cu_3O_{7-\delta}$: Symmetry of the Order Parameter, and Gradiometers for Biomagnetic Applications

by

Konstantin Alexander Kouznetsov

M.S. (Illinois Institute of Technology) 1995
Diploma (Moscow Institute of Physics and Technology) 1993

A dissertation submitted in partial satisfaction of the
requirements for the degree of
Doctor of Philosophy

in

Physics

in the

GRADUATE DIVISION
of the
UNIVERSITY of CALIFORNIA at BERKELEY

Committee in charge:

Professor John Clarke, Chair
Professor T. Van Duzer
Professor A. Zettl

1999

The High Temperature Superconductor $YBa_2Cu_3O_{7-\delta}$: Symmetry of the Order Parameter, and Gradiometers for Biomagnetic Applications

Copyright © 1999

by

Konstantin Alexander Kouznetsov

The U.S. Department of Energy has the right to use this document
for any purpose whatsoever including the right to reproduce
all or any part thereof.

Abstract

The High Temperature Superconductor $YBa_2Cu_3O_{7-\delta}$: Symmetry of the Order Parameter, and Gradiometers for Biomagnetic Applications

by

Konstantin Alexander Kouznetsov
Doctor of Philosophy in Physics

University of California at Berkeley

Professor John Clarke, Chair

The cuprate $YBa_2Cu_3O_{7-\delta}$ is the material that drives the majority of the technological applications of high transition temperature (T_c) superconductors, particularly in the area of superconducting electronics. Despite the widespread use of high-T_c superconducting materials in a variety of applications, the nature of the superconducting state in these materials remains unknown since their discovery more than a decade ago. Many properties of the high-T_c superconductors are determined by their order parameter, which is a wavefunction describing the superconducting condensate. The symmetry of the order parameter in cuprates has been the subject of intensive investigation, leading to conflicting sets of results. Some experiments supported conventional, s-wave symmetry of the order parameter, while others indicated an unconventional, d-wave symmetry.

The first part of this thesis is an experimental study of the symmetry of the order parameter in $YBa_2Cu_3O_{7-\delta}$. A new class of phase sensitive experiments is described that involve Josephson tunneling along the c-axis of twinned crystals of $YBa_2Cu_3O_{7-\delta}$. These experiments showed that an s-wave component must *reverse* sign across the twin boundary, providing *direct* evidence for a mixed, s+d symmetry of the order parameter in $YBa_2Cu_3O_{7-\delta}$, and thereby reconciling two conflicting sets of previous findings and establishing the dominant d-wave pairing symmetry.

The second part of the thesis focuses on practical applications of $YBa_2Cu_3O_{7-\delta}$ in superconducting electronics. We introduce a novel Superconducting QUantum Interference Device (SQUID) gradiometer. The principle of operation of these long baseline high-T_c

SQUID gradiometers is based on the inductive coupling of the input coil of a planar flux transformer to the pickup up loop of a directly coupled magnetometer. The long baseline of the gradiometer, 48 mm, and the intrinsic balance of better than 1 part in 100 make it an ideal candidate for operation in biomagnetic systems in an unshielded environment. We demonstrate a practical multichannel SQUID system for MagnetoCardioGraphy. Using this system, we are able to detect magnetic signals from the human heart in an unshielded environment, thereby demonstrating the applicability of our technology to practical applications. Our gradiometers are readily manufacturable devices that could be used in clinical applications in the near future.

To Audrey

Contents

List of Figures vi

List of Tables x

I Direct Evidence for a Mixed Symmetry of the Order Parameter in $YBa_2Cu_3O_{7-\delta}$ 1

1 Background 2
- 1.1 Superconductivity . . . 2
- 1.2 Quasiparticle tunneling and Josephson effect . . . 6

2 High Temperature Superconductors 8
- 2.1 Probes of the magnitude of the order parameter . . . 12
- 2.2 Phase sensitive experiments in an a-b plane . . . 13
- 2.3 Phase sensitive experiments along c-axis . . . 16

3 Concept of the experiment 19

4 Experiment 24
- 4.1 $YBa_2Cu_3O_{7-\delta}$ Crystals . . . 24
- 4.2 Fabrication of Josephson Junctions . . . 28
- 4.3 Measurements . . . 33
- 4.4 Experimental Results . . . 36

5 Discussion and Conclusions 43
- 5.1 Effects of trapped magnetic flux . . . 43
- 5.2 Self-field effects . . . 44
- 5.3 Nonuniform current density distribution . . . 45
- 5.4 Time reversal symmetry breaking at the twin boundary . . . 47
- 5.5 Experiments on twinned textures . . . 50
- 5.6 Conclusions . . . 52

II High-T_c Gradiometers for Biomagnetic Applications **54**

6 Superconducting QUantum Interference Devices: principles of operation **55**

7 SQUID gradiometers for biomagnetic applications **59**

8 High-T_c SQUIDs for unshielded operation **63**

9 Gradiometers: principles of operation **68**
9.1 First-order gradiometer 68
9.2 Second-order gradiometer 70
9.3 Practical considerations for gradiometer fabrication 72

10 Gradiometers: practical realizations **74**
10.1 Mechanical first-order gradiometer 75
10.2 Mechanical second-order gradiometer 80
10.3 First-order flipchip gradiometer 84

11 Multichannel system for MagnetoCardioGraphy **91**
11.1 System description 91
11.2 System calibration and performance 94

12 MagnetoCardioGraphy in an unshielded environment **103**

13 Conclusions and future directions **109**

Bibliography **111**

List of Figures

1.1 (a) Pairing of superconducting electrons via the exchange of a phonon. (b) In the superconducting ground state, the magnitude of the order parameter $\Delta(\mathbf{k})$ is constant along any direction on the Fermi surface. (c) The density of states of Pb determined from tunneling experiments showing the absence of states below the superconducting energy gap; from [1] 3

1.2 Schematic diagrams illustrating tunneling processes in a superconductor-insulator-superconductor ($S - I - S$) tunnel junction. (a) The bias voltage is zero, $V = 0$, and only Cooper pairs can tunnel between the two superconductors. (b) For $V > 2\Delta/e$, quasiparticles can tunnel from filled states below $E_F - \Delta$ in one superconductor into empty states above $E_F + \Delta$ in the other. (c) Resulting $I - V$ characteristic for current-biased junction showing a supercurrent at zero voltage bias. For $I > I_c$, the junction switches to the quasiparticle branch; from [2]. $V > 2\Delta/e$. 5

2.1 Unit cell of $YBa_2Cu_3O_{7-\delta}$. 9

2.2 Four basis states of the order parameter in a two-dimensional tetragonal lattice; from [3]. 11

2.3 (a) Schematic diagram of the corner SQUID experiment (a), and (b) the magnetic interference pattern expected for a $d_{x^2-y^2}$ superconductor, from Ref. [4], where the critical current and flux are in units of I_0 and Φ_0, respectively. 15

2.4 (a) Schematic diagram of the c-axis tunneling experiment, and (b) the magnetic field interference pattern expected in a presence of a substantial s-wave component, where the critical current and flux are in units of I_0 and Φ_0, respectively, Ref. [5]. 17

3.1 Schematic diagram of a c-axis tunneling experiment on a Josephson junction (hatched) grown across a twin boundary (dashed line). For the YBCO order parameter shown the s-wave component changes sign across the boundary . 21

3.2 (a) Magnetic field interference pattern expected for a symmetric junction for a magnetic field applied along the twin boundary. (b) Fraunhofer pattern expected for an asymmetric junction for a field applied perpendicularly to the twin boundary. Here, the critical current and flux are in units of I_0 and Φ_0, respectively. 22

4.1 Nemarsky photograph of a heavily twinned $YBa_2Cu_3O_{7-\delta}$ crystal. Twin domains of opposite orientation are seen as areas of different contrast (white and gray). 25
4.2 Nemarsky photograph of a single crystal of $YBa_2Cu_3O_{7-\delta}$ used in the experiment. Note two large area twin domains separated by a single twin boundary. 27
4.3 Steps in the fabrication procedure. (a) mounting of the crystal, (b) SiO evaporation, (c) evaporation of the Ag/PbIn counterelectrode. (d) shows a crossection of the junction. 29
4.4 Nemarsky photograph of junction B1. The twin boundary runs vertically through the center of the photograph. The Ag/PbIn strip is the horizontal white region. 31
4.5 Nemarsky photograph of junctions B2a (right) and B2b (left), fabricated on the same crystal, whose photograph is shown in Fig. 4.2. The counterelectrodes are the two vertical white strips. The twin boundary in junction B2a is covered by the Ag/PbIn film on the right. 32
4.6 Schematic diagram of the experiment. 34
4.7 $I_c(\mathbf{B})$ for junction SD2 (γ=0.47). The magnetic field is applied parallel to the twin boundary. Inset: I-V characteristic at 1.3 K and 0.0413 mT. . . . 37
4.8 (a) $I_c(\mathbf{B})$ for junction B2a (γ=0.4) for fields applied perpendicularly $B(90°)$ and parallel $B(0°)$ to the twin boundary. (b) $I_c(\mathbf{B})$ for junction B2b grown on a a single twin domain, showing conventional, Fraunhofer-like behavior for two orthogonal field directions $B(90°)$ and $B(0°)$. 38
4.9 $I_c(\mathbf{B})$ for junction B2a (γ=0.4) for ten values of angle ϕ relative to the twin boundary (TB). Successive plots are offset vertically by 30 μA. Center inset: Computed values of I_c/I_0 vs Φ/Φ_0 for a junction with a sign reversal of the s-wave component and γ=0.4. Successive plots are offset vertically by 0.3. . 41

5.1 $I_c(\mathbf{B})$ for junction B2a, solid line in (a) and (b), for a field parallel to the twin boundary. Simulated $I_c(\mathbf{B})$ for a uniform junction with γ=0.4, dashed line in (a). Simulated $I_c(\mathbf{B})$ assuming a current density in one domain is three times higher than in the other, dashed line in (b). 46
5.2 Simulated $I_c(\mathbf{B})$ patterns for a symmetric junction in which the relative phase of the s- and d-wave components rotates from 0 to π over the length ξ on either side of the boundary. (a), (b) and (c) correspond to ξ/L=0, 0.05 and 0.5, respectively. Here, L is the total junction length. 48
5.3 (a) $I_c(\mathbf{B})$ for a junction fabricated across two twin textures indicating Frauuhofer-like patterns for both parallel (solid circles) and perpendicular (open circles) fields. (b) another example of $I_c(\mathbf{B})$ in a texture bounadry junction; this pattern displays a local minimum at $B = 0$. 51

6.1 Schematic diagram of the flux-locked electronics used to operate a dc-SQUID. 56
6.2 Flux modulation scheme for SQUID with (a) $\Phi_{qs} = N\Phi_0$ and (b) $\Phi_{qs} = (N + 1/4)\Phi_0$. 57

7.1 Schematic diagram of the wire-wound first-order gradiometer; from [6]. . . . 61

8.1 Noise spectra of slotted-washer SQUID and directly coupled magnetometer cooled in a zero field in a shielded environment. 66

9.1 Schematic diagrams of first-order gradiometer (a) and flux transformer used in the practical device (b). 69
9.2 Schematic diagrams of symmetric second-order gradiometer (a) and practical transformer coil (b). 71

10.1 Calibration of first-order gradiometer in a uniform field; (a) magnitude of the signal $\|S\|$ and (b) signal S from the magnetometer vs the relative horizontal separation of the centers of the magnetometer pickup loop and the input loop of the flux transformer (arbitrary zero). Dashed line in (a) is the magnitude of a 100 Hz perpendicular magnetic field. 77
10.2 Signal from the magnetometer vs separation from two parallel wires (circles). The solid line is the response expected from the ideal first-order gradiometer. The dashed line in inset is the gradiometer response with $C_x^{(0)} = 0.01$. . . . 79
10.3 Calibration of the second-order gradiometer in a uniform field; (a) magnitude of the signal $\|S\|$ and (b) the signal S from the magnetometer vs the vertical separation between the magnetometer and the flux transformer (arbitrary zero). Dashed line in (a) is the magnitude of a 100 Hz perpendicular magnetic field. 81
10.4 Signal S from the magnetometer vs separation from two parallel wires. The line assumes that the deviation from the slope of -4 arises solely from the common mode in the first-gradient with $C_{xz}^{(1)} = 1.4 \times 10^{-2}$. 83
10.5 Photograph of first-order flipchip gradiometer showing details of the trimming grid. 85
10.6 Response of the first-order gradiometer to uniform field, and coupling constant α as a function of the separation between the magnetometer and the flux transformer. 86
10.7 Noise spectra of (a) unshielded magnetometer (gray) and gradiometer (black), and (b) shielded directly coupled magnetometer used in gradiometer. 88
10.8 Magnitude (a) and phase (b) of the frequency response of the flip-chip gradiometer to a uniform field measured in a styrofoam flask (circles) and in a biomagnetic dewar (squares). 89

11.1 Schematic diagram (a) and a photograph (b) of the five channel system. . 92
11.2 Attenuation of 6 Hz signal in the x direction (upper trace) by hardware gradiometer without (middle trace) and with (lower trace) subtraction of reference magnetometer. 95
11.3 Cancellation of low frequency signal produced by the motion of the elevator. Uncorrelated random telegraph signal in the gradiometer channel cannot be eliminated using references. 97
11.4 Cancellation of the uniform field signal using an adaptive algorithm. Frequency of the applied signal is swept from 1 to 50 Hz. 99

11.5 Calibration of the software second-order gradiometer with two parallel wires. Solid and open circles in (a) are signals of lower and upper first-order gradiometers, respectively. The lines in (a) demonstrate effects of $C_z^{(0)} \approx -3 \times 10^{-3}$ and $C_z^{(0)} \approx -1.6 \times 10^{-3}$ in the simulated response of first-order gradiometers. Squares in (b) correspond to the second-order gradiometer formed in software. The line in (b) assumes $C_z^{(0)} \approx -1.4 \times 10^{-3}$ and $C_{xz}^{(1)} \approx 1.13 \times 10^{-2}$ for the second derivative device. 100
11.6 Unshielded noise spectra as measured by hardware first-order gradiometer (gray) and second-order gradiometer balanced in software (black). 102

12.1 Measurement of magnetocardiogram in an unshielded environment in the presence of a 10 nT interfering signal. Signals from x, y and z references are divided by 100. Bandwidth 0.3-47 Hz, notch filters at 60 and 180 Hz, no averaging. 105
12.2 Unshielded magnetocardiogram detected in 0.3-47 Hz bandwidth without averaging. 106
12.3 Unshielded magnetocardiogram averaged 119 times; bandwidth 0.3-47 Hz. . 107

List of Tables

4.1 Parameters of junctions fabricated at UCB. 35
4.2 Parameters of junctions fabricated at UCSD. 36

8.1 The electrical and magnetic properties of slotted-washer SQUIDs on 30° bicrystals. 65
8.2 The electrical and magnetic properties of directly coupled magnetometers on 24° bicrystals. 65

Acknowledgements

I am indebted to my advisor, Professor John Clarke, for taking me on as a graduate student and providing guidance and support throughout my Ph.D. program. His ability to know which studies are interesting, as well as to provide focus and guidance in solving complicated issues form the foundation of the successful experimental research in his group.

My thanks go to Beth Chen with whom I shared all ups and downs of the project on the symmetry of the order parameter in high-T_c materials. Her hard work and dedication have been absolutely essential to the successful outcome of this experiment. I thank Safi Bahcall for sharing ideas and providing theoretical support to the experiment.

In the course of the project on gradiometers for MagnetoCardioGraphy I was privileged to work closely with Achim Kittel, Robert McDermott, Byungdu Oh, Joerg Borgmann, Sherry Cho and Vladimir Gorgadze. I would like acknowledge the contributions of Achim Kittel and Robert McDermott at the most challenging stages of this project. Special thanks go to Joerg Borgmann, who spent only six months in our lab, but provided very important expertise in software and biomagnetic (MCG) measurements. I would like to thank Sherry Cho and Vladimir Gorgadze for their efforts in continuing the MCG project and taking it to the next level in the near future. Additionally, I thank Sherry for her indispensable contribution and help in all aspects of our high-T_c SQUID efforts. I would like to thank Gene Dantsker for his help at the outset of the MCG project.

The success of both projects would have been impossible without our collaborators outside UC Berkeley. I would like to thank Prof. Dynes of UC San Diego and his graduate students Guoping Sun and Andy Katz for fruitful and stimulating collaboration on the first project. I thank Prof. Ginsberg and his group at the University of Illinois at Urbana-Champaign for providing high quality crystals of $YBa_2Cu_3O_{7-\delta}$ used in our experiments.

I thank Vladimir Matiasevic and his group at Conductus, Inc. for providing the thin films of $YBa_2Cu_3O_{7-\delta}$ on 4 inch wafers that we used to fabricate our gradiometers. I thank Andrei Matlashov and Robin Cantor for help with the SQUID electronics. Special thanks go to Roger Koch for numerous discussions and help with data analysis of our MCG data. I would like to thank Jiri Vrba for valuable discussions on system integration.

I would like to acknowledge the expertise and help from the Machine Shop staff and the Electronics Shop staff in the Physics Department, and from the Microfabrication Laboratory staff at the EECS Department, UC Berkeley.

All the work in this thesis is concerned with high-temperature superconductors, which was the subject of my research for the last eight and a half years. I would like to thank Artem Tsvetkov, John Zasadzinski and, particularly, Liam Coffey for introducing me to this subject prior to my arrival at UC Berkeley.

The thesis itself is the reflection of the scientific aspects of the work. However, I spent a lot of time interacting with other members of the Clarke group, who made my life in the second basement of Birge Hall very enjoyable. For this I would like to thank Marc-Oliver Andre, Yann Chemla, Josephine Chen, Oliver Froehlich, Helene Grossman, Teressa Ho, Darin Kinion, Cagliyan Kurdak, Jan Kycia, Tom Lee, Michael Mück, Alex Rimberg, Barbara Salisbury, Klaus Schlenga, Tim Shaw, Sabu Tanaka, Roy Therrien and Dinh Ton in addition to individuals mentioned above.

I would like to thank my thesis committee for their work, useful comments, and suggestions. I gratefully acknowledge the funding for my research provided by the the Director, Office of Energy Research, Office of Basic Energy Sciences, Materials Sciences Division of the U.S. Department of Energy under Contract No. DE-AC03-76SF00098.

Most of all I would like to thank my wife Audrey for her love, encouragement and support throughout my graduate studies.

Preface

My thesis consists of two parts that have the high-temperature superconductor (HTS) $YBa_2Cu_3O_{7-\delta}$ as a common denominator. This material was discovered more than a decade ago, and provided a broad basis for both fundamental and applied research in solid state physics.

The first part of the thesis concerns a fundamental study of the symmetry of the order parameter in $YBa_2Cu_3O_{7-\delta}$. A brief introduction to the fundamentals of superconductivity and the Josephson effect is given in Chapter 1, and an introduction to high-temperature superconductivity as well as a historical overview of previous experiments on HTS can be found in Chapter 2. The concept of our experiment is described in Chapter 3 and the experiment itself in Chapter 4. A detailed discussion of various experimental issues that support the main conclusion of the mixed symmetry of the order parameter in $YBa_2Cu_3O_{7-\delta}$ is given in Chapter 5.

I find it important for any novel material to be practically useful as opposed to being only the testing ground for fundamental research. The second part of the thesis describes one of the practical applications of $YBa_2Cu_3O_{7-\delta}$, a gradiometer for biomagnetic applications. High-T_c superconductors find themselves used in a variety of applications, which include Superconducting QUantum Interference Devices (SQUIDs). An introduction to SQUID principles and HTS SQUID gradiometers can be found in Chapters 6 and 7, respectively. Practical HTS SQUIDs developed in our group for unshielded applications are described in Chapter 8. Chapters 9 and 10 describe the principle and realization of long baseline HTS gradiometers that are particularly suitable for unshielded biomagnetic applications such as MagnetoCardioGraphy (MCG). The design and implementation of a multichannel system for MCG is described in Chapter 11. Measurements of magnetic signals from the human heart in an unshielded environment are presented in Chapter 12. Chapter 13 contains conclusions and describes future directions.

Part I

Direct Evidence for a Mixed Symmetry of the Order Parameter in $YBa_2Cu_3O_{7-\delta}$

Chapter 1

Background

In this chapter, I will provide background information necessary for understanding the content of the rest of the thesis. We will review the fundamentals of superconductivity followed by a discussion of quasiparticle and Josephson tunneling in superconductors. Tunneling effects form the basis for understanding of the experiments described in part I as well as the principles of Superconducting QUantum Interference Devices (SQUIDs), which we will consider in part II of this thesis. Introductory material of this chapter follows standard texts on these topics. For a detailed introduction to superconductivity, one can consult references [7, 8]. Superconducting tunneling phenomena are considered in detail in [2, 9, 10]. References [9, 10] also contain extensive literature on quasiparticle and Josephson tunneling in conventional superconductors.

1.1 Superconductivity

Superconductivity was discovered in 1911 by Kamerling Onnes. He observed a disappearance of electrical resistance in various metals when metals were cooled below a certain critical temperature T_c. In 1933, Meissner and Ochsenfeld discovered that a superconductor is also a perfect diamagnetic, i.e. a superconductor expels magnetic flux when cooled below T_c. However, it was not until 1957 that Bardeen, Cooper and Schrieffer formulated a microscopic theory of superconductivity, known as the BCS theory. They showed that a weak attractive interaction between electrons mediated by the electron-phonon interaction causes an instability with respect to the formation of bound pairs of electrons, so-called Cooper pairs. The process of electron pairing is illustrated in Fig. 1.1

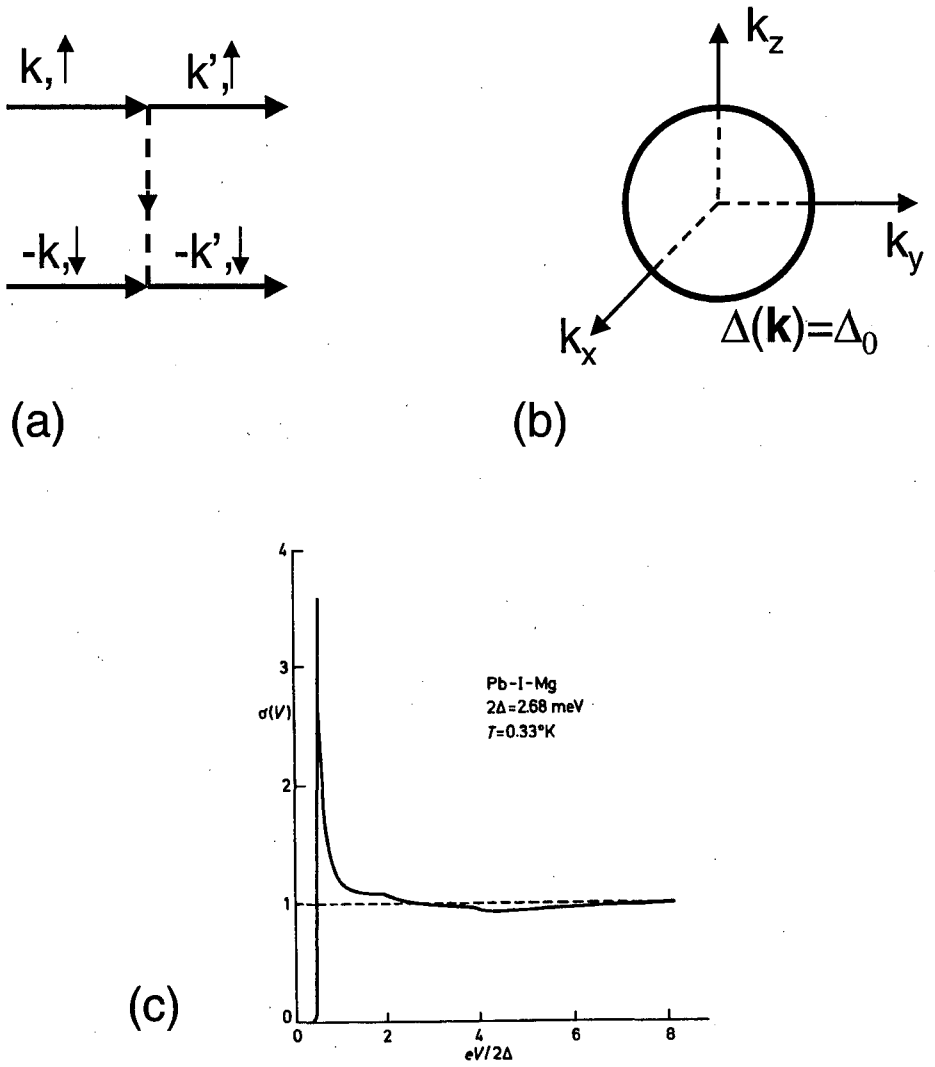

Figure 1.1: (a) Pairing of superconducting electrons via the exchange of a phonon. (b) In the superconducting ground state, the magnitude of the order parameter $\Delta(\mathbf{k})$ is constant along any direction on the Fermi surface. (c) The density of states of Pb determined from tunneling experiments showing the absence of states below the superconducting energy gap; from [1]

(a) where two electrons occupying states with equal and opposite momentum and spin (solid arrows) are attracted via the emission and absorption of a phonon (dashed line). In a superconductor, Cooper pairs reside at the Fermi level forming a macroscopic quantum condensate. The condensate can be described by a macroscopic wave function implying a long-range phase coherence of all superconducting electrons in the ground state. The local density of the superconducting electrons is given by

$$n_s = |\psi(\mathbf{r})|^2 , \tag{1.1}$$

where

$$\psi(\mathbf{r}) = |\psi(\mathbf{r})| e^{i\phi(\mathbf{r})} \tag{1.2}$$

is a macroscopic wave function describing the condensate, and $\phi(\mathbf{r})$ is a macroscopic phase.

As shown in the BCS theory, a minimum energy $E_g = 2\Delta(T)$ is required to break a Cooper pair to create two quasiparticle excitations from the ground state. The quantity Δ is the energy gap around the Fermi level in a quasiparticle density of states. In a BCS superconductor, Δ is constant and isotropic in k-space, as shown schematically in Fig. 1.1 (b). It was shown by Gorkov that Δ is the order parameter in a superconductor, which is a wave function that describes the paired electrons, and the phenomenological macroscopic wave function ψ in (1.1) is proportional to Δ. At low temperatures $T \ll T_c$, $\Delta(T)$ approaches its limiting value Δ_0 which is related to the critical temperature T_c by

$$2\Delta_0 = 3.528 k T_c. \tag{1.3}$$

The most direct way of probing the quasiparticle density of states is tunneling spectroscopy, which will be described in detail below. The quasiparticle density of states of Pb obtained from tunneling measurements is shown in Fig. 1.1 (c). It exhibits a lack of states below the energy gap Δ and a sharp peak at the gap energy $eV = \Delta$. Fine structure at energies above the gap seen in Fig. 1.1 (c) arises from strong electron-phonon interactions in Pb. These strong-coupling effects serve as direct evidence for the phonon mediated pairing mechanism underlying the BCS theory. All of the low-temperature superconductors, with a possible exception of heavy-fermion materials, exhibit the BCS pairing state,*i.e.* they are described by the order parameter $\Delta(\mathbf{k}) = \Delta_0$ that is very nearly isotropic in k-space.

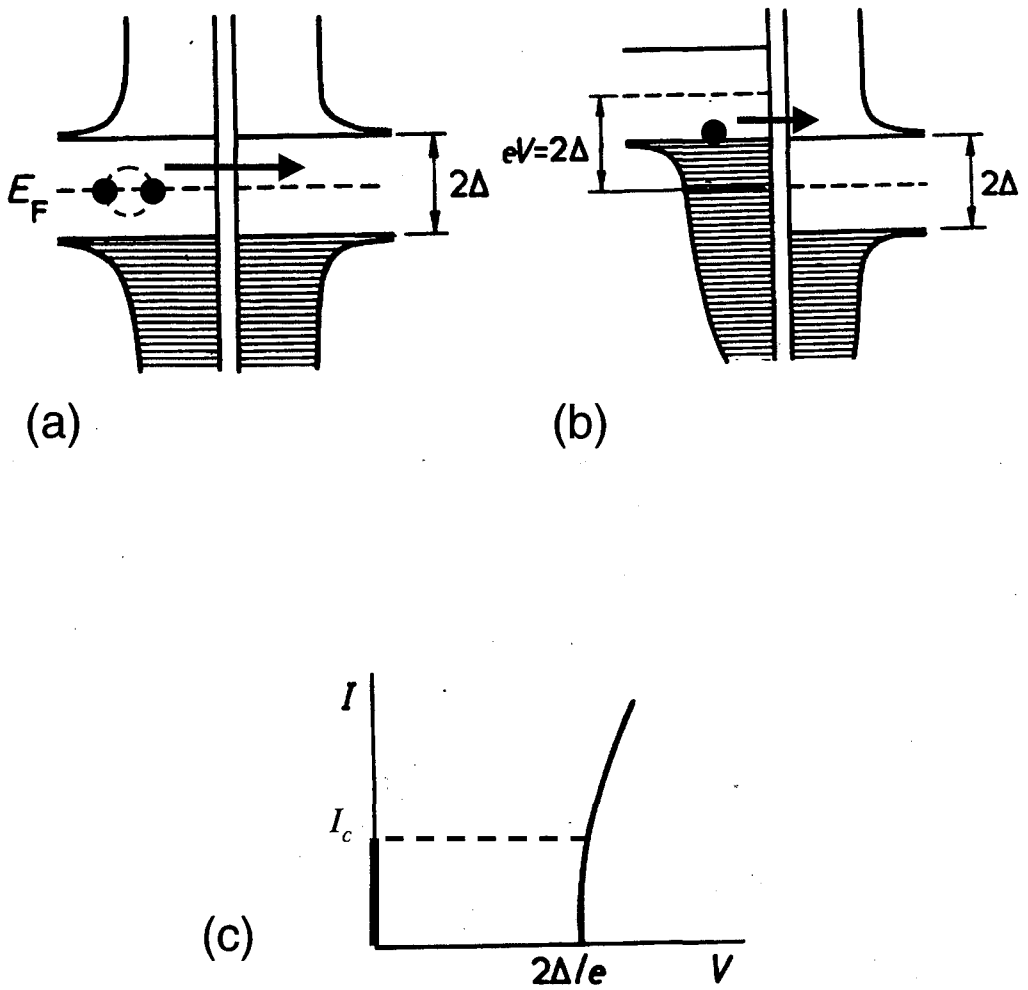

Figure 1.2: Schematic diagrams illustrating tunneling processes in a superconductor-insulator-superconductor ($S-I-S$) tunnel junction. (a) The bias voltage is zero, $V=0$, and only Cooper pairs can tunnel between the two superconductors. (b) For $V > 2\Delta/e$, quasiparticles can tunnel from filled states below $E_F - \Delta$ in one superconductor into empty states above $E_F + \Delta$ in the other. (c) Resulting $I-V$ characteristic for current-biased junction showing a supercurrent at zero voltage bias. For $I > I_c$, the junction switches to the quasiparticle branch; from [2]. $V > 2\Delta/e$.

1.2 Quasiparticle tunneling and Josephson effect

The superconductor-insulator-superconductor tunnel junction is formed when two superconductors are separated by a thin insulating barrier. The energy diagram for $T = 0K$ is shown in Fig. 1.2 (a). All energy levels are filled up to $E_F - \Delta$. At zero voltage, quasiparticles cannot tunnel across the barrier because all allowed quasiparticle states on the other side of the barrier are filled. For bias voltages $V < 2\Delta/e$, there is still no quasiparticle current flowing across the junction because filled states below the gap in one superconductor have no access to empty states in the other. At $V = 2\Delta/e$, Fig. 1.2 (b), there is an abrupt increase in current because electrons filling a large number of states just below the gap on the left can tunnel into empty states on the right. For higher bias voltages, the current increases and asymptotically approaches the normal state tunneling characteristic.

Electrons occupying states within Δ of the Fermi level in a normal state form Cooper pairs in the superconducting state; the Cooper pair energy is at the Fermi level. At $V = 0$, Cooper pairs can tunnel between two superconductors resulting in a nonzero current at zero voltage. The tunneling of Cooper pairs is called the Josephson effect after B. D. Josephson who predicted its existence in 1962. One can describe the Josephson tunneling via an overlap of the wave function of the condensate in one material with the wave function of the condensate in another, leading to a nonzero probability of Cooper pair tunneling. In this case, the Josephson current is given by

$$I = I_c sin(\Delta\phi), \tag{1.4}$$

where $\Delta\phi$ is the difference between the macroscopic phases of the two condensates, and I_c is the maximum supercurrent that can flow between the two superconductors. The value of I_c is a fundamental quantity determined by the pairing state. For two identical BCS superconductors separated by an insulating barrier, using microscopic theory Ambegaokar and Baratoff showed that

$$I_c = \frac{\pi\Delta(T)}{2eR_n} tanh\left(\frac{\Delta(T)}{2kT}\right), \tag{1.5}$$

where $\Delta(T)$ is the BCS energy gap, R_n is the normal state resistance of the junction, and e is the electron charge. In a current-biased junction, the current switches from a Josephson branch at $V = 0$ to a quasiparticle branch as soon as the applied current exceeds I_c; this results in the I-V characteristic schematically shown in Fig. 1.2 (c).

In discussing Josephson effects, one needs to consider the influence of electric and magnetic fields on the phase difference across the junction. If there is only an electric field applied to the junction, the phase difference $\Delta\phi$ becomes time dependent quantity. It evolves in time according to

$$d(\Delta\phi)/dt = 2eV/\hbar, \tag{1.6}$$

where V is a voltage difference maintained across the junction. This is called the *ac* Josephson effect as opposed to the *dc* Josephson effect described by Eq. (1.4). If a magnetic field is applied to a Josephson junction, the magnetic flux threading the junction area will spatially modulate the phase difference $\Delta\phi$. For an extended junction penetrated by a flux Φ the local value of the Josephson current oscillates with position along the junction length depending on the amount of magnetic flux in the junction. This leads to a magnetic field interference pattern of the form

$$I_c(\Phi) = I_0 \left| \frac{sin(\pi\Phi/\Phi_0)}{(\pi\Phi/\Phi_0)} \right|, \tag{1.7}$$

where $\Phi_0 = hc/2e = 2.07\times10^{-15}\,\mathrm{T\ m^2}$ is the single quantum of magnetic flux. In the general case of both electric and magnetic fields applied to a junction, the electrodynamics of a Josephson junction are governed by a time dependent Sine-Gordon equation. A discussion of the Sine-Gordon equations is beyond the scope of this introduction; introductory material and a detailed discussion can be found in [7] and [10], respectively.

Chapter 2

High Temperature Superconductors

The high-temperature superconductors were discovered by Bednorz and Mueller in 1986 [11] in a cuprate oxide LaBaCuO, and immediately attracted much attention not only from condensed matter physicists but also from researchers in other fields of physics and technology. Immediately after their original discovery, it became evident that these materials do not behave as conventional BCS superconductors. Discoveries of other cuprates with transition temperatures as high as 134 K ($HgBa_2Ca_2Cu_4O_{8+\delta}$) soon followed. The observed high transition temperatures in cuprates cannot be explained by the conventional electron-phonon pairing mechanism. Numerous transport, thermodynamic and optical measurements indicate the existence of low energy excitations inside an apparent gap structure. The existence of energy states inside the superconducting gap is contradictory to the conventional BCS model. Growing experimental evidence for an unconventional pairing instigated intense research efforts, both theoretical and experimental, to determine the nature of the pairing mechanism in high-T_c materials. A number of unconventional pairing scenarios have been proposed, each leading to different predictions for the symmetry of the order parameter; for reviews see [12, 13]. Finding the nature of the pairing symmetry in cuprates became a key problem in high temperature superconductivity. Much of the experimental and theoretical research efforts in high-T_c superconductivity in the early 1990's was focused on providing evidence for one pairing scenario or another.

The cuprate oxides are layered materials in which layers of CuO_2 oriented in the

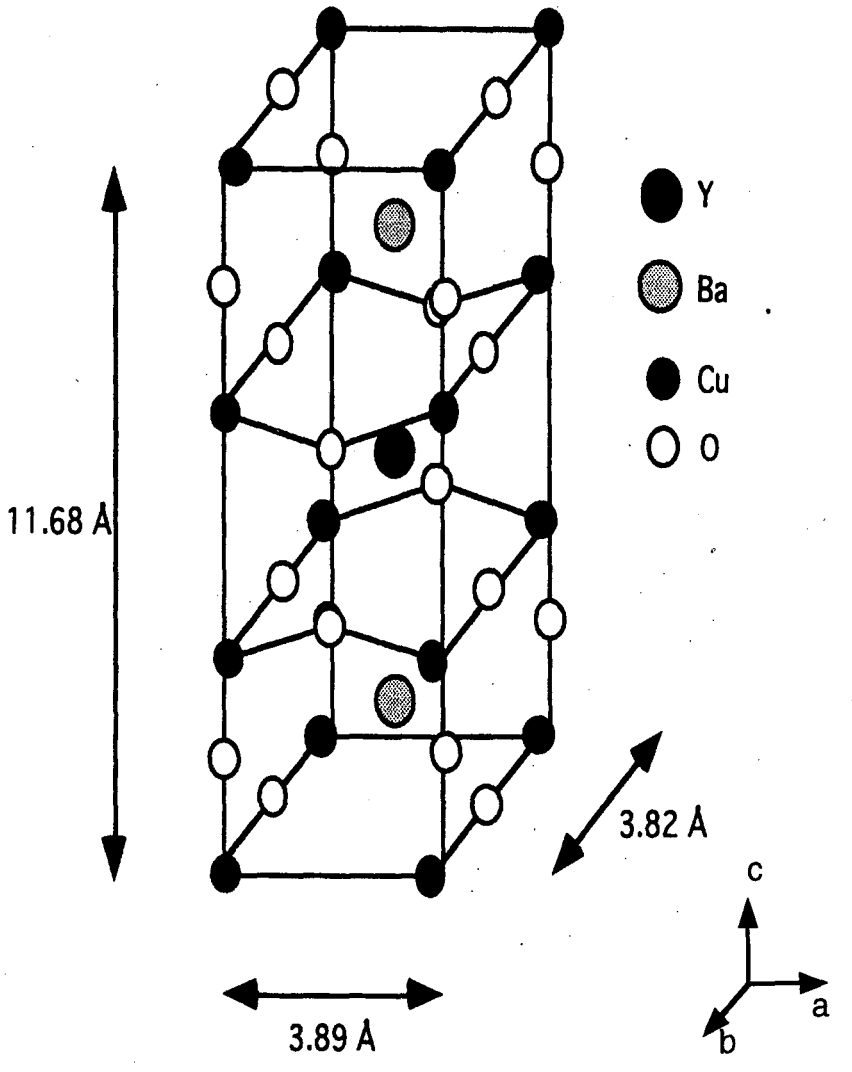

Figure 2.1: Unit cell of $YBa_2Cu_3O_{7-\delta}$.

a-b plane are weakly coupled along the c-direction via Josephson tunneling. A unit cell of $YBa_2Cu_3O_{7-\delta}$ is shown schematically in Fig. 2.1. In the undoped case, $\delta = 0$, the Cu^{+2} ions have a magnetic moment which results in antiferromagnetic ordering below the Neel temperature, and the system becomes an insulating antiferromagnet. As the CuO_2 layers become doped with holes the system becomes metallic and superconducting. In $YBa_2Cu_3O_{7-\delta}$, the highest transition temperature 92.5 K, occurs in the optimally doped case, $\delta \approx 0.05$.

In classifying the possible symmetry representations of the order parameter [3], one assumes that superconducting electrons form a singlet pairing state confined to a single CuO_2 plane with a square lattice structure. The two-dimensional square lattice has a symmetry group C_{4v} with four even parity irreducible representations that transform under symmetry operations as the identity, $xy(x^2 - y^2)$, $x^2 - y^2$ and xy. These four basis states are shown in Fig. 2.2 and are labeled as s_+, s_-, $d_{x^2-y^2}$ and d_{xy}, respectively. Two leading candidates for the pairing symmetry are a conventional s^+ state, in which the order parameter is constant for any lattice direction

$$\Delta(\mathbf{k}) = \Delta_0, \tag{2.1}$$

and a $d_{x^2-y^2}$ state described by

$$\Delta(\mathbf{k}) = \Delta_0(cosk_x a - cosk_y a). \tag{2.2}$$

Other possible s-wave symmetries include the extended s-wave, which also transforms as an s^+ state, and has the form

$$\Delta(\mathbf{k}) = \Delta_0(cosk_x a + cosk_y a), \tag{2.3}$$

and an anisotropic s-state [14] described by

$$\Delta(\mathbf{k}) = \Delta_1(cosk_x a - cosk_y a)^4 + \Delta_2. \tag{2.4}$$

Complex mixed states such as $s + id_{x^2-y^2}$ state [15] described by

$$\Delta(\mathbf{k}) = \Delta_0[\varepsilon + i(1-\varepsilon)(cosk_x a - cosk_y a)] \tag{2.5}$$

and an anyon state $d_{x^2-y^2} + id_{xy}$ [16, 17] described by

$$\Delta(\mathbf{k}) = \Delta_0[(1-\varepsilon)(cosk_x a - cosk_y a) + i\varepsilon(2sink_x asink_y a)] \tag{2.6}$$

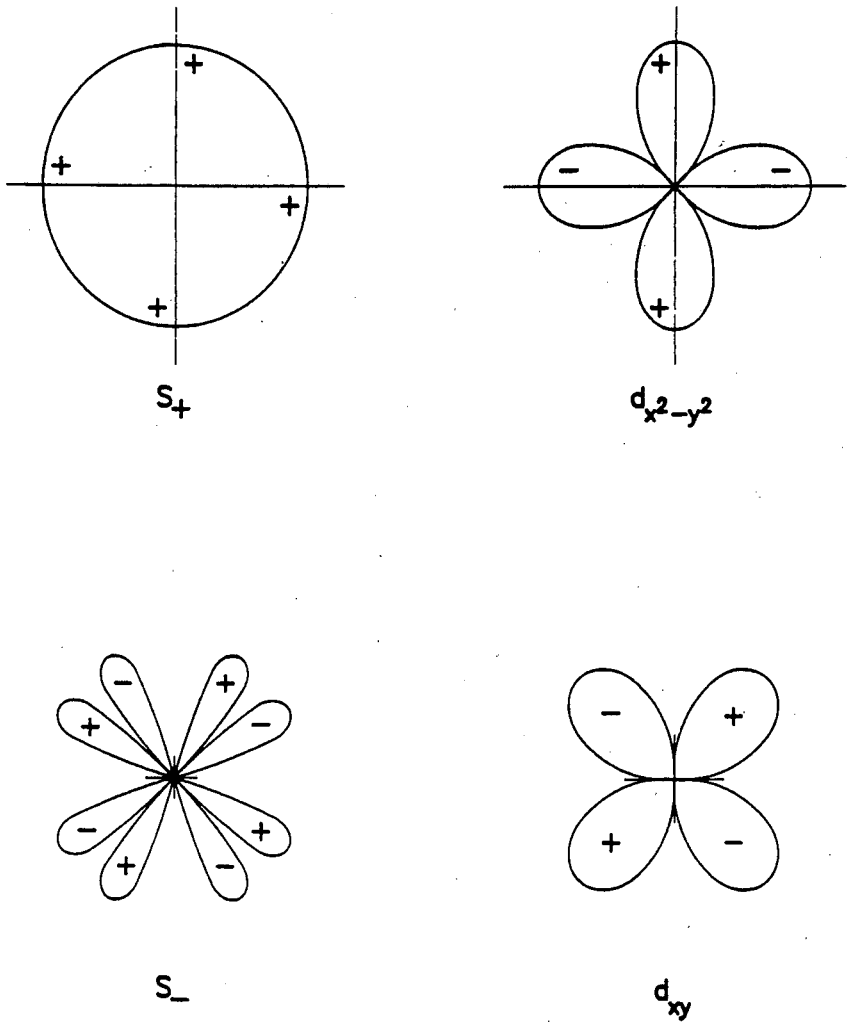

Figure 2.2: Four basis states of the order parameter in a two-dimensional tetragonal lattice; from [3].

have been proposed as well. Here, ε is the fraction of the s or d_{xy} component mixed in with a dominant $d_{x^2-y^2}$ state. States of mixed symmetry in the tetragonal lattice are possible in principle, but imply the existence of an additional second-order phase transition, which has not been observed experimentally. Furthermore, symmetry states with a complex order parameter such as $s + id_{x^2-y^2}$ and $d_{x^2-y^2} + id_{xy}$ break time-reversal symmetry. At present, the effects of time-reversal symmetry breaking in the bulk have not been observed experimentally in high-T_c materials.

In most cuprates, the CuO_2 planes are not tetragonal but have an orthorhombic structure. This is due to a slight difference in the a- and b-lattice directions. However, in the case of YBCO a substantial anisotropy results from the presence of chains in the b-direction. The significant anisotropy of the penetration depth [18], $\sim 50\%$, in the a-b plane shows that the orthorhombicity cannot be neglected. The point group of YBCO is C_{2v}; the a- and b- axes become inequivalent, but each remain a twofold axis and a mirror plane. As a result, states with a mirror symmetry along the a- and b- axes are allowed to mix, e.g. s_+ can mix with $d_{x^2-y^2}$ and s_- can mix with d_{xy}. These considerations are fundamental for understanding the concepts of phase sensitive experiments described in this thesis. We will develop these ideas further in chapter 3, when we discuss the concepts of our experiments.

Experiments probing the symmetry of the order parameter can be divided into two main categories: those measuring the anisotropy of the magnitude of the order parameter, and those sensitive to the relative phase of the order parameter for different directions in the crystal. Next, I will give a brief overview of the first class of experiments.

2.1 Probes of the magnitude of the order parameter

For all proposed states other than a conventional s-wave state the magnitude of the order parameter exhibits a modulation with a fourfold rotational symmetry. This results in a zero magnitude of the order parameter along nodal directions. The anisotropic energy gap leads to the existence of low lying excitations in the quasiparticle density of states $N(\omega)$. In a clean system with nodes, $N(\omega)$ varies linearly with ω at low energies and the low temperature quasiparticle properties vary as power laws. In a conventional BCS superconductor with a constant gap Δ, the low temperature density of quasiparticles and their contribution to optical, thermodynamic and transport properties decreases exponentially. For example, the temperature dependence of the penetration depth $\lambda(T)$ in a BCS superconductor is given

by

$$\frac{\lambda(T)-\lambda(0)}{\lambda(0)} \approx \sqrt{\frac{2\pi\Delta}{T}}e^{-\Delta/T} \tag{2.7}$$

where Δ is the energy gap and T is the absolute temperature. However, for a clean $d_{x^2-y^2}$ material with a density of states given by

$$\frac{N(\omega)}{N_0} \approx \frac{\omega}{\Delta_0}, \tag{2.8}$$

$\lambda(T)$ varies linearly with temperature as follows

$$\frac{\lambda(T)-\lambda(0)}{\lambda(0)} \approx \frac{T}{\Delta_0}. \tag{2.9}$$

The low-temperature linear variation of the penetration depth down to 2 K was observed by Hardy *et al.* [19] on high quality YBCO crystals. These experiments are considered to be the most sensitive probe of the magnitude of the gap in the low lying excitations in cuprates, indicating that line nodes are at most 2% of the full magnitude of the gap. Further investigations of the temperature dependence of $\lambda(T)$ in a variety of high-T_c materials, including crystals doped with impurities, demonstrated a power law behavior of $\lambda(T)$ at low temperatures as well.

Angle-resolved photoemission spectroscopy allowed *local* probes of the order parameter on different parts of the Fermi surface [20]. Measurements of the shift in the leading edge of the photoemission spectra clearly demonstrated the suppression of the magnitude of $\Delta(\mathbf{k})$ along nodal directions. Further evidence for gapless excitations have been found in NMR experiments [21], raman spectroscopy [22], tunneling spectroscopy [23] and specific heat [24] measurements.

2.2 Phase sensitive experiments in an a-b plane

Experiments probing the anisotropy of the magnitude of the order parameter cannot distinguish between s- or d-wave symmetries, because the density of states of an anisotropic or an extended s-wave superconductor is also gapless, displaying low energy excitations. In order to determine whether the symmetry of $\Delta(\mathbf{k})$ is predominantly d- or s-wave, one has to perform experiments that are sensitive to the relative phase of the order parameter in k-space. The phase of the order parameter does not vary in k-space for isotropic or anisotropic s-wave superconductors. However, in a d-wave superconductor, the

phase of the order parameter changes by π at the nodal lines along (110) directions. In an extended s-wave state, the phase changes by π along the eight nodal lines, but there is an overall invariance under rotation by 90°.

Phase sensitive experiments were first suggested by Geshkenbein, Larkin, and Barone [25] as a test for a p-wave symmetry in the heavy fermion superconductors. Sigrist and Rice [26] suggested concepts of phase sensitive experiments in the context of the d-wave pairing in cuprates.

The original phase sensitive experiments [27] involved two Josephson tunnel junctions on the two orthogonal faces of a single crystal of YBCO. The junctions are connected with a loop of a conventional s-wave superconductor forming a dc Superconducting QUantum Interference Device (SQUID). The critical current of the SQUID is periodically modulated by a magnetic flux threading the loop. The observed interference patterns differ dramatically depending on the relative phase of the order parameter of YBCO at the locations of the junctions. An improved version of this experiment [4] involved a single Josephson junction rather than a dc SQUID. The concept of the experiment is shown in Fig. 2.3 (a). The Josephson junction was fabricated on the corner of YBCO crystal, as shown in Fig. 2.3 (a). In this geometry, part of the tunneling current flows along the a-axis and part along the b-axis. For an s-wave superconductor the phase difference across a-c and b-c faces would be the same. For a magnetic field applied along the c-direction, the critical current would exibit the conventional, Fraunhofer interference pattern given by

$$I_c(\Phi) = I_0 \left| \frac{sin(\pi\Phi/\Phi_0)}{(\pi\Phi/\Phi_0)} \right| \tag{2.10}$$

where Φ is the total flux through the junction, and $\Phi_0 = h/2e$ is a single flux quantum. However, in a d-wave superconductor the order parameter has opposite signs along the a and b directions as shown in Fig. 2.3 (a). This results in a cancellation of the net supercurrent flowing in a symmetric junction in a zero magnetic field. When a magnetic field is applied parallel to the c axis, the total current would reach its maximum at a non-zero value of the field, tracing out an intereference pattern given by

$$I_c(\Phi) = I_0 \left| \frac{sin^2(\pi\Phi/2\Phi_0)}{(\pi\Phi/2\Phi_0)} \right|. \tag{2.11}$$

This interference pattern is plotted in Fig. 2.3 (b) where the current is in units of I_0 and the flux is in units of Φ_0. Interference patterns of the type shown in Fig. 2.3 (b) were actually observed in the corner junction modulation experiments [4] providing the most convincing

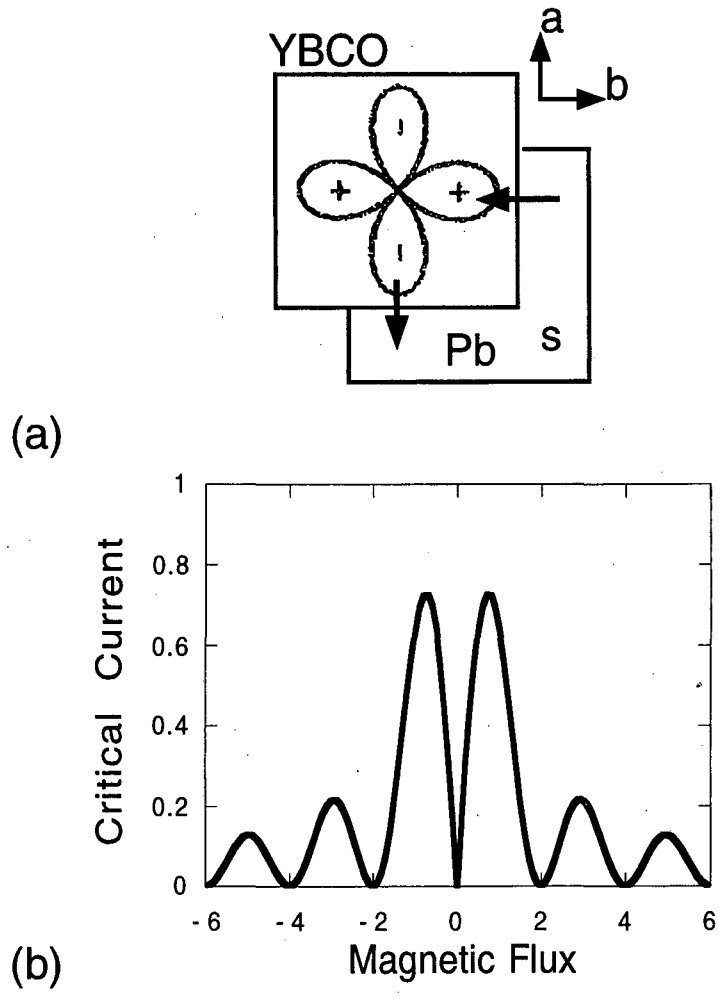

Figure 2.3: (a) Schematic diagram of the corner SQUID experiment (a), and (b) the magnetic interference pattern expected for a $d_{x^2-y^2}$ superconductor, from Ref. [4], where the critical current and flux are in units of I_0 and Φ_0, respectively.

evidence for a sign change of the order parameter in YBCO. Similar results were found in experiments by Brawner and Ott [28] on a Nb-YBCO dc SQUID with point contact junctions. Spontaneous currents in a thin film Nb-YBCO SQUID were investigated by Mathai *et al.* [29] with a scanning SQUID microscope. The last results not only reinforced the case for a d-wave symmetry but also provided an upper bound on the amount of breaking of the time-reversal symmetry in the unconventional pairing state of YBCO.

Very elegant experiments demonstrating the sign change of the order parameter were performed at IBM in a tricrystal ring geometry [30, 31]. In this experiment a ring of YBCO was deposited on a $SrTiO_3$ substrate that contained three regions in which the a and b axes were successively rotated by 30°. In this geometry, Josephson junctions are formed at each grain boundary in such a way that in a d-wave superconductor there will be a net phase shift of π around the closed ring. For a ring with a sufficiently large inductance, the circulating supercurrent will result in a half-integer flux quantum in the ring. The predicted half odd-integer flux quanta were experimentally detected at IBM using a scanning SQUID microscope, providing further evidence for $d_{x^2-y^2}$ pairing.

2.3 Phase sensitive experiments along c-axis

In contrast, the observation of Josephson tunneling perpendicular to the CuO_2 planes between heavily twinned YBCO and a conventional *s*-wave superconductor [5, 32, 33, 34, 35] provided very strong evidence for an s-wave pairing in YBCO. The results of c-axis tunneling experiments clearly contradicted the results of phase-sensitive experiments in the a-b plane, thus creating a heated controversy around a fundamental question regarding the symmetry of the order parameter in high-T_c materials.

The concept of c-axis tunneling experiments is shown in Fig. 2.4. The c-axis Josephson junction consists of a film of a conventional superconductor, Pb, deposited on an a-b face of the YBCO single crystal. In this geometry, the tunneling current along the c direction is expected to vanish for a tetragonal YBCO crystal with a pure $d_{x^2-y^2}$ symmetry. In an orthorhombic crystal with mixed s- and d-wave symmetries, the s component is expected to contribute a nonzero supercurrent along the c-axis. The situation is different yet again in a heavily twinned sample or a thin film, where the non-dominant s component, induced by the orthorhombicity, is expected to average to zero over many twin domains, leading to a pure $d_{x^2-y^2}$ order parameter.

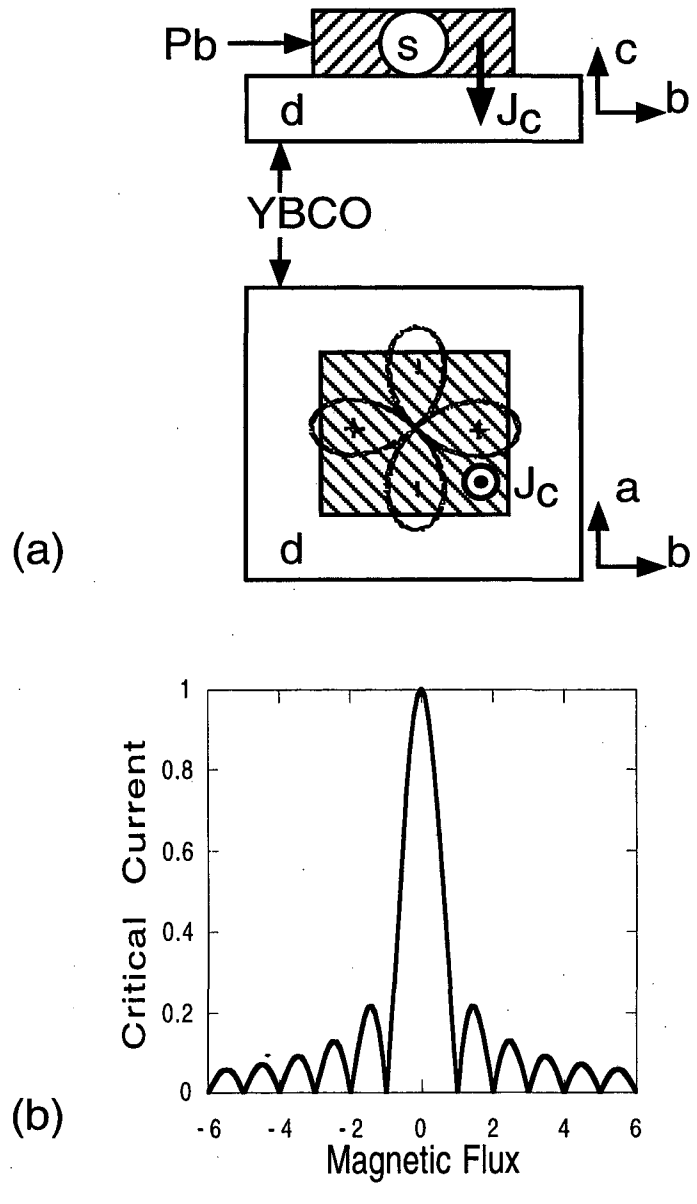

Figure 2.4: (a) Schematic diagram of the c-axis tunneling experiment, and (b) the magnetic field interference pattern expected in a presence of a substantial s-wave component, where the critical current and flux are in units of I_0 and Φ_0, respectively, Ref. [5].

Sun *et al.* [5] performed extensive measurements of tunneling along the c direction between $Y_{1-x}Pr_xBa_2Cu_3O_{7-\delta}$ and Pb. At temperatures near 1 K, the junction current-voltage characteristics exhibited a Josephson supercurrent at zero voltage and a very small quasiparticle tunneling current for voltages below the Pb gap. When a magnetic field was applied in the plane of the junction, the supercurrent was modulated according to the conventional Fraunhofer interference pattern, Fig. 2.4 (b). These results, obtained on heavily twinned samples of YBCO, provided strong evidence for the dominant s-wave component. The temperature dependence of the penetration depth $\lambda_{ab}(T)$ inferred from these measurements was consistent with results of earlier microwave experiments [19].

A possible explanation for a nonzero Josephson current between YBCO and Pb came from considerations of higher-order tunneling processes. It was suggested by Tanaka [36] that for tunneling between pure s- and d-wave superconductors the nonzero Josephson current may arise from second-order tunneling, *i.e.* the coherent transport of pairs of Cooper pairs across the tunneling barrier. The current-phase relation of this current is given by $I = I_0 sin2\delta$, where I_0 is the magnitude of the critical current, and δ is the difference between the phase of the s-wave order parameter and the phase of the d-wave order parameter averaged over the azimuthal angle. This current phase relation implies that applied microwaves of frequency f will induce steps in the junction $I-V$ characteristics at voltages $(n/2)f\Phi_0$, where n is an integer and $\Phi_0 = h/2e$ is a single flux quantum; in BCS superconductors, the current-phase relation is given by Eq. (1.4) and microwave induced steps appear at $nf\Phi_0$. Kleiner *et al.* investigated the microwave response of the c-axis junctions extensively, and found *no* evidence for half-integer steps to the limit of their experimental resolution. Results of these measurements reinforced previous findings of a substantial s-wave component in YBCO samples.

Chapter 3

Concept of the experiment

Heavily twinned samples of YBCO were used in most of the phase sensitive experiments described in the previous section. A very important question that arises in the discussion of the observed results is the following: what happens to the order parameter upon crossing the twin boundary? If we believe that the order parameter in a single twin is of mixed s- and d-wave symmetry, then one of these symmetries must be dominant. The dominant component is the one whose phase does not change across the twin boundary, where the a and b axes rotate by 90°. That component is preserved throughout the sample in the heavily twinned limit in which the number of twinned domains tends to infinity and there is no systematic bias in favor of one orientation.

For the dominant $d_{x^2-y^2}$ component, conservation of the sign of the order parameter implies that the "+" lobe of the $d_{x^2-y^2}$ order parameter is always oriented along the same direction in the crystal regardless of the orientations of the a- and b- axes, as is the "-" lobe. The a-b plane phase sensitive experiments described in the previous section support this picture. First of all, the critical current of twinned samples differs only by a small amount from the critical current of the untwinned samples [4, 27]. If the order parameter were rotating by 90° at twin boundaries, we would expect the critical current to be reduced by averaging over the twin regions of opposite polarity. The strongest argument for sign preservation yet comes from the observation of the reproducible π-phase shift for tunneling along two orthogonal directions [4, 27, 28, 29, 30, 31]. Without the sign preservation assumption, it would very difficult to devise with another physical mechanism underlying the observed behavior. However, these experimental observations serve only as an *indirect* evidence in support of the hypothesis of the constant orientation of the $d_{x^2-y^2}$ order param-

eter across twin boundaries. By the same token, the results of c-axis tunneling experiments on heavily twinned samples seemed to rule out the $d_{x^2-y^2}$ scenario and to support a pure s-wave picture.

In order to probe the behavior of the order parameter at the twin boundary directly, we devised an experiment, whose concept is shown schematically in Fig. 3.1. We assume that the order parameter in a single twin is of mixed $d_{x^2-y^2}$+s symmetry with the d-wave component dominant. This is represented pictorially as a larger "+" lobe of the d-wave order parameter oriented along the b-axis in the twin domain on the left. Across the twin boundary the crystal axes rotate by 90°, but the d-wave component preserves its orientation relative to the crystal. The nondominant, s component changes sign across the twin boundary which can be represented as an enlarged "-" lobe of the order parameter on the right. Note that the "+" and "-" lobes point in the same direction in both domains, illustrating the preservation of the sign of the d-wave component.

In the experiment, we form a *c*-axis Josephson tunnel junction by depositing a thin film of a conventional superconductor, Pb, over the twin boundary as shown by the hatched area in Fig. 3.1. Because Pb is an *s*-wave superconductor, the Pb counterelectrode couples only to the *s*-wave component of the YBCO order parameter: the net phase difference with any *d*-wave component integrates to zero. If our assumption of the sign change of an s-wave component is correct, than the s-wave order parameter of Pb couples to a +s component of the YBCO in one domain and to a -s component in the other. This results in a π-shift in the relative phase between the s-wave components of Pb and YBCO at the twin boundary, which, in the absence of a magnetic field, leads to supercurrents flowing in opposite directions on either side of the boundary. If the junction areas deposited on either side of the twin boundary are the same, i.e. the junction is symmetric, than the net current in the c directions will be zero. If we apply a magnetic field *parallel* to the twin boundary, contributions from the two domains will no longer cancel each other, resulting in a nonzero Josephson supercurrent reaching its maximum value at a nonzero applied field $B \neq 0$. For a symmetric junction with an abrupt π-phase shift at the twin boundary, the magnetic field interference pattern will be given by

$$I_c(\Phi) = I_0 \left| \frac{sin^2(\pi\Phi/2\Phi_0)}{(\pi\Phi/2\Phi_0)} \right|. \tag{3.1}$$

This interference pattern is shown schematically in Fig. 3.2 (a).

A c-axis Josephson junction can be made asymmetric either by deliberately choos-

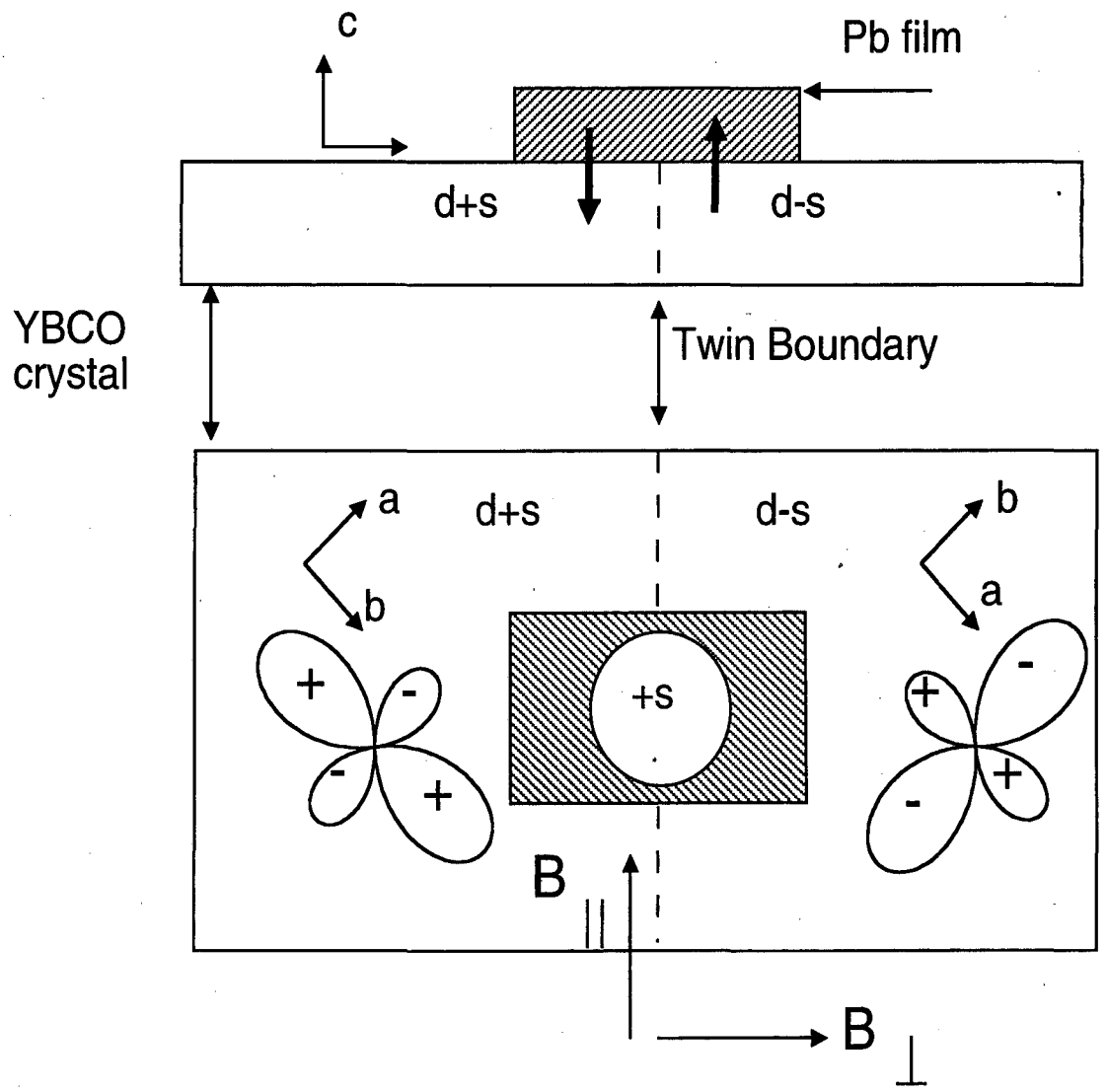

Figure 3.1: Schematic diagram of a c-axis tunneling experiment on a Josephson junction (hatched) grown across a twin boundary (dashed line). For the YBCO order parameter shown the s-wave component changes sign across the boundary

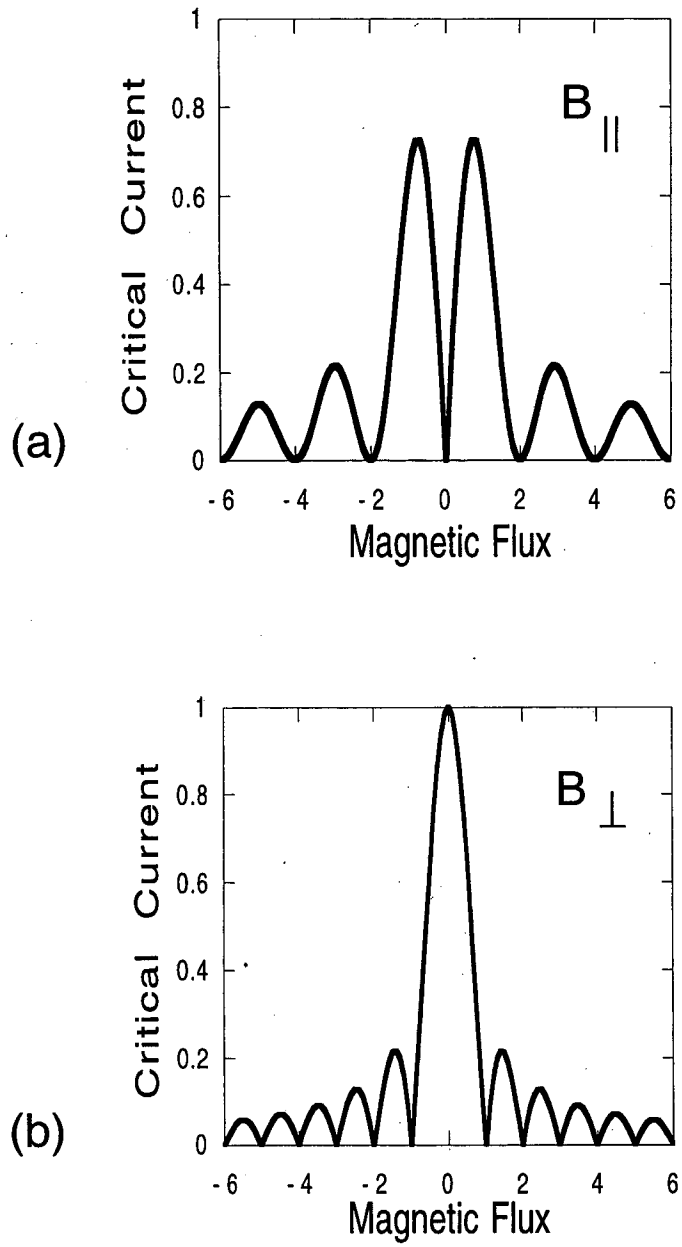

Figure 3.2: (a) Magnetic field interference pattern expected for a symmetric junction for a magnetic field applied along the twin boundary. (b) Fraunhofer pattern expected for an asymmetric junction for a field applied perpendicularly to the twin boundary. Here, the critical current and flux are in units of I_0 and Φ_0, respectively.

ing different junction areas over two twin domains or by an unintentional difference in the thickness of the tunneling barrier on either side of the twin boundary. The junction asymmetry results in a nonzero supercurrent for zero applied field. If we apply a field *parallel* to the twin boundary, the net supercurrent will increase compared to the zero field value, displaying a local minimum at $B = 0$ and two global maxima on either side of the $B = 0$ axis. However, a magnetic field applied *perpendicular* to the twin boundary will not influence the π-phase shift at the twin boundary and the conventional Fraunhofer-like interference pattern will result.

Let us consider what happens if our assumptions regarding the symmetry of the order parameter and its behavior at the twin boundary are false. An alternative scenario would be a dominant s-wave component which remains unchanged upon crossing the twin boundary. In either the pure s-wave or mixed dominant-s-plus-d cases this will lead to a maximum net supercurrent at $B = 0$. The magnetic field interference pattern would exhibit the conventional Fraunhofer-like behavior regardless of the direction of the magnetic field in the plane of the junction. The Fraunhofer pattern would be given by

$$I_c(\Phi) = I_0 \left| \frac{sin(\pi\Phi/\Phi_0)}{(\pi\Phi/\Phi_0)} \right| \tag{3.2}$$

which is shown schematically in Fig. 3.2 (b). A Fraunhofer-like pattern with a global maximum at zero field is also expected for any test junction deposited on a single twin of the YBCO.

Note that the magnetic field interference patterns shown in Fig. 3.2 are similar to those observed in phase sensitive measurements in the a-b plane; patterns with the local minimum at $B = 0$ occur only in the case of a dominant $d_{x^2-y^2}$ symmetry. However, the mechanisms leading to this behavior are different from those in our experiments. In the a-b plane experiments, a local minimum at $B = 0$ arises from the global $d_{x^2-y^2}$ order parameter in the crystal and the directional tunneling into two orthogonal lobes of the order parameter. In our own c-axis experiments, the local minimum is due to the existence of a nondominant s-wave component that changes sign across the twin boundary in the presence of a dominant d-wave contribution. In subsequent chapters, I will describe how we carried out the proposed experiments, and discuss our results.

Chapter 4

Experiment

The experiments described in chapter 3 were carried out at UC, Berkeley (UCB) by Beth Chen and myself and at UC, San Diego (UCSD) by Guoping Sun and Andy Katz [37]. Both groups independently obtained similar experimental results using $YBa_2Cu_3O_{7-\delta}$ crystals grown at UCSD and the University of Illinois, respectively. Prior to this work, the UCB and UCSD groups collaborated on a set of microwave experiments whose purpose was to investigate the existence of the second-order Josephson tunneling along c-direction in $YBa_2Cu_3O_{7-\delta}$-Pb junctions.

4.1 $YBa_2Cu_3O_{7-\delta}$ Crystals

Intensive investigations of various techniques for growing single crystals as well as thin films began immediately after the discovery of high-temperature superconductivity. Experiments focused on the investigation of fundamental physical properties of cuprates demanded high quality single crystals. The most popular technique for preparing single crystals of $YBa_2Cu_3O_{7-\delta}$ is growth in a flux consisting of an excess of CuO and $BaCO_3$ or BaO [38].

Here, we outline the procedure used at the University of Illinois [39] for growth of $YBa_2Cu_3O_{7-\delta}$ crystals. Their method of crystal growth is similar to that of Schneemeyer et al. [38]. It involves mixing of CuO, $BaCO_3$ and Y_2O_3 with a Y:Ba:Cu molar ratio of 1:4:10. The mixture is then poured into a crucible of 10.5% yttria-stabilized zirconia. The crucible is heated in air in a box furnace to 780°C in 4 hours, then to 980°C in another 4 hours, held at 980°C for 4 hours, and slowly cooled to 830°C over 37.5 hours. The crystal growth

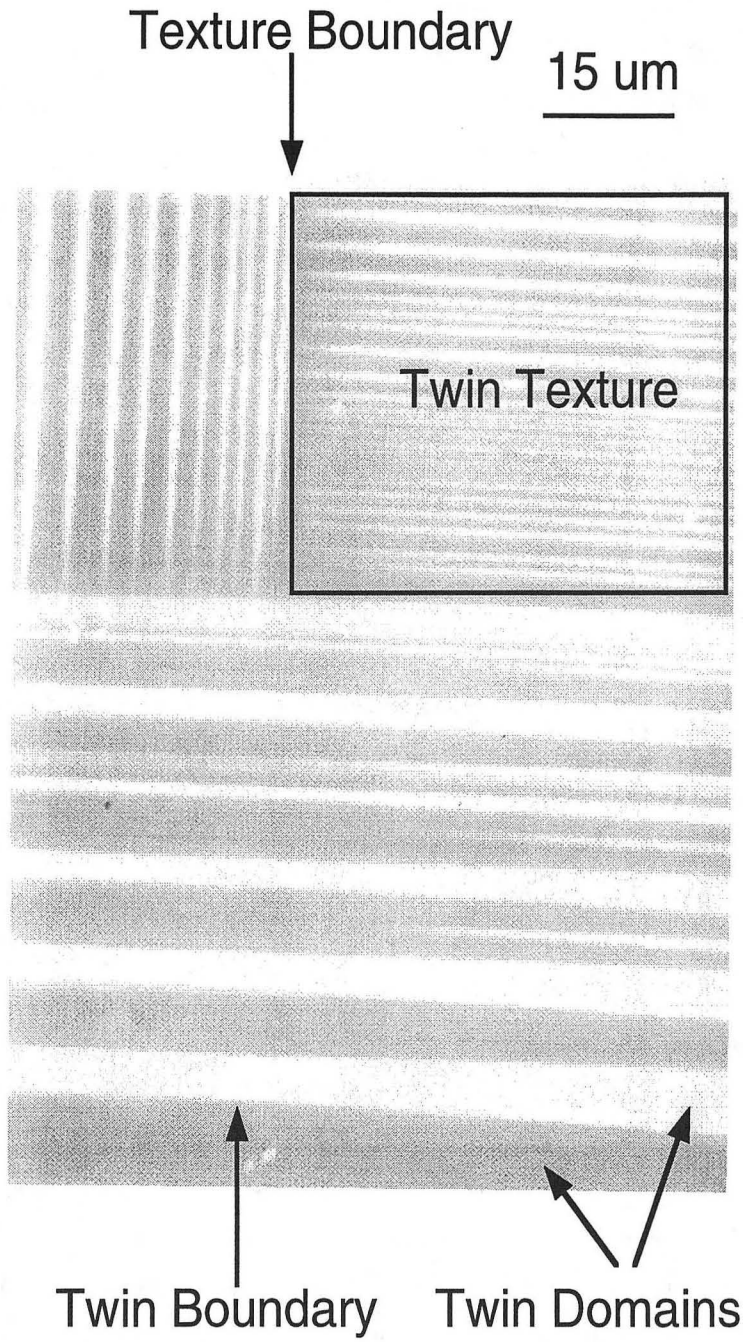

Figure 4.1: Nemarsky photograph of a heavily twinned $YBa_2Cu_3O_{7-\delta}$ crystal. Twin domains of opposite orientation are seen as areas of different contrast (white and gray).

occurs during this cooling segment. The temperature is reduced to 780°C in 5 hours, to 470°C in another 5 hours, and to room temperature. This procedure yields single crystals as large as 2 x 2 x 0.05 mm^2 with a c axis oriented perpendicularly to the largest face, and the characteristic orthorhombic structure with a (110) twinning. The temperature of the superconducting transition is increased by the annealing procedure in the presence of a continuous flow of oxygen. Typical transition temperatures are near 90 K, exhibiting sharp superconducting transitions about 1 K wide. Similar techniques [40] were used at UCSD to grow crystals that were subsequently used in experiments carried out by the UCSD group.

A photograph of a typical twinned $YBa_2Cu_3O_{7-\delta}$ crystal taken under polarized light (Nemarsky) microscope is shown in Fig. 4.1. Areas of different contrast correspond to different twin domains in the crystal. Twin boundaries are located in (110) planes which are the borders between white and gray areas in the crystal. Individual twin domains could be as wide as 40 μm in a heavily twinned crystal. Very often we observed wide twin domains of one orientation separated by thin twin domains of an orthogonal orientation. The existence of two large size neighboring twins was quite rare. In Fig. 4.1, one can see distinctly that the twin boundaries are parallel to each other within one twin texture. In the neighboring twin textures, the direction of twinning rotates by 90°, i.e. twin boundaries in two neighboring twin textures are perpendicular to each other. We define the boundary between two textures as a texture boundary as opposed to a twin boundary. In-plane dimensions of a single texture could be as large as 500×500 μm^2 in a heavily twinned crystal.

Single crystals of $YBa_2Cu_3O_{7-\delta}$ used in most of the transport, thermodynamic and optical experiments have almost invariably been twinned. Our experiments demanded large area crystals consisting of only two twin domains separated by a single twin boundary. The method of obtaining crystals that contain only few domains or even a single domain are based on detwinning of heavily twinned crystals. The detwinning procedure used at the University of Illinois [41] is based on applying a pressure of 25MPa to a heavily twinned crystal along the (100) direction while the crystal is kept at 450°C. The temperature of 450°C is chosen to increase the mobility of oxygen atoms, which causes the reorientation of the domains. However, temperatures in excess of 450°C lead to a rapid loss of oxygen from the crystal. Figure 4.2 shows a Nemarsky photograph of the single crystal that consists of two twin domains separated by a single twin boundary. This particular crystal was used in our experiments described below. The area of the smaller twin domain is about

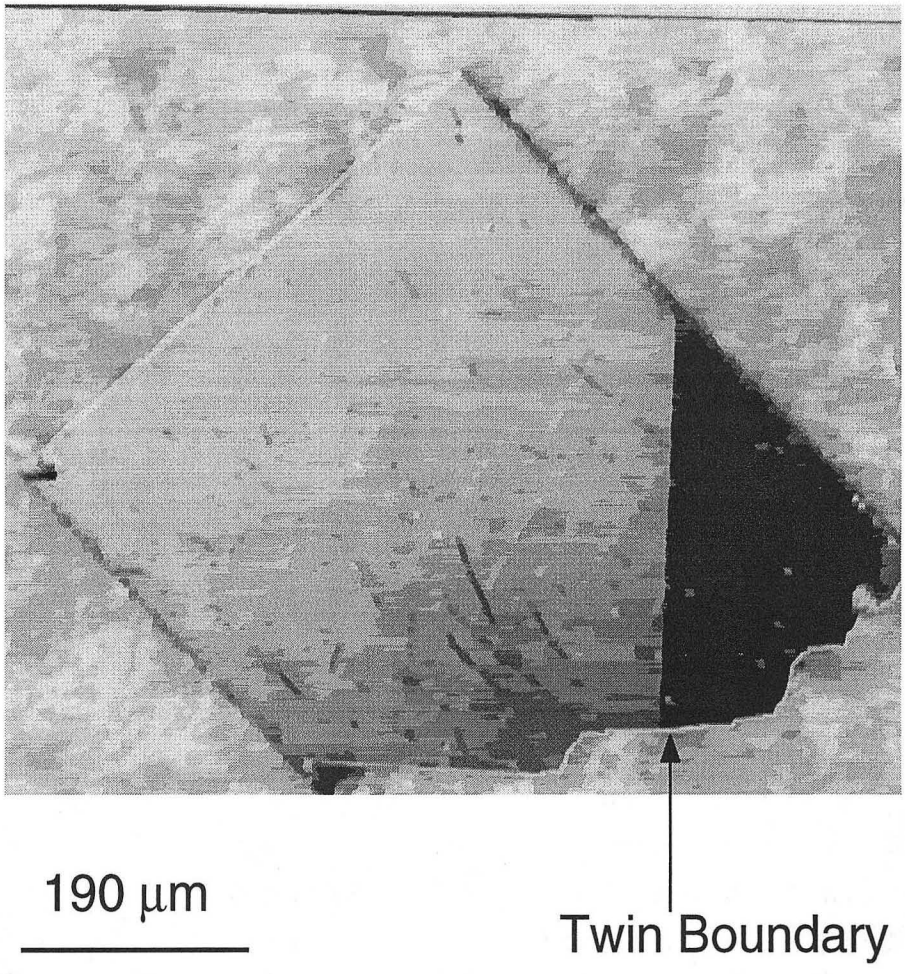

Figure 4.2: Nemarsky photograph of a single crystal of $YBa_2Cu_3O_{7-\delta}$ used in the experiment. Note two large area twin domains separated by a single twin boundary.

$200 \times 200 \mu m^2$. Such large dimensions of the domains allowed us to fabricate two Josephson junctions on the same crystal. One of these junctions was positioned across two twin domains separated by a single twin boundary, whereas the other one was positioned on a single (larger) domain and served as a control junction for the experiment.

4.2 Fabrication of Josephson Junctions

Our procedure of junction fabrication is derived from the method used by Valles *et al.* [42] for the fabrication of c axis oriented quasiparticle tunnel junctions. Similar techniques were used by Sun *et al.* [5] for fabrication of c-axis Josephson junctions between heavily twinned crystals of $Y_{1-x}Pr_xBa_2Cu_3O_{7-\delta}$ and Pb.

Figure 4.3 illustrates the steps involved in the fabrication procedure. In the first step, Fig. 4.3 (a), a crystal is glued to a non-conductive substrate using 5 min epoxy. We etched the surface of the crystal in a 1% solution of Br_2 and methanol for 1 minute. The effect of the etching is to remove the degraded layer of YBCO from the surface of the crystal. The surface flatness of YBCO crystals was investigated by Sun *et al.* [34], before and after etching in Br_2 solution, using a scanning tunneling microscope. It was shown in [34] that the etching of high quality YBCO crystals in Br_2 solution is uniform and does not introduce etch pits on the surface. Therefore, the flatness of the surface is preserved during the etching process. However, in certain cases, for crystals with degraded surfaces, we observed the formation of etch pits on the surface, which was evident from an inspection of the crystal surface under an optical microscope. Crystals with degraded surfaces were discarded from the experiment. Next, , we evaporated a 500 μm thick layer of SiO through the shadow mask as shown in Fig. 4.3 (b) in order to define two opposite edges of the rectangular junction. The mask width of 240 μm determined the longer dimension of the junction. Another purpose of the SiO layer is to isolate areas of the crystal containing multiple residual twins that remained after detwinning.

We formed the counterelectrode by evaporating a 2.5 nm thick layer of Ag through the shadow mask, and then, without breaking vacuum, by evaporating a 1μm thick film of $Pb_{0.95}In_{0.05}$. We used a $Pb_{0.95}In_{0.05}$ rather than a Pb source to extend the longevity of Josephson junctons. If a Pb/YBCO junction is kept in air for about 1 hour, oxygenation and diffusion of the Pb layer leads to a degradation of the junction. The 5% of In introduced into the source leads to a formation of a thin In layer film covering the Pb film, protecting

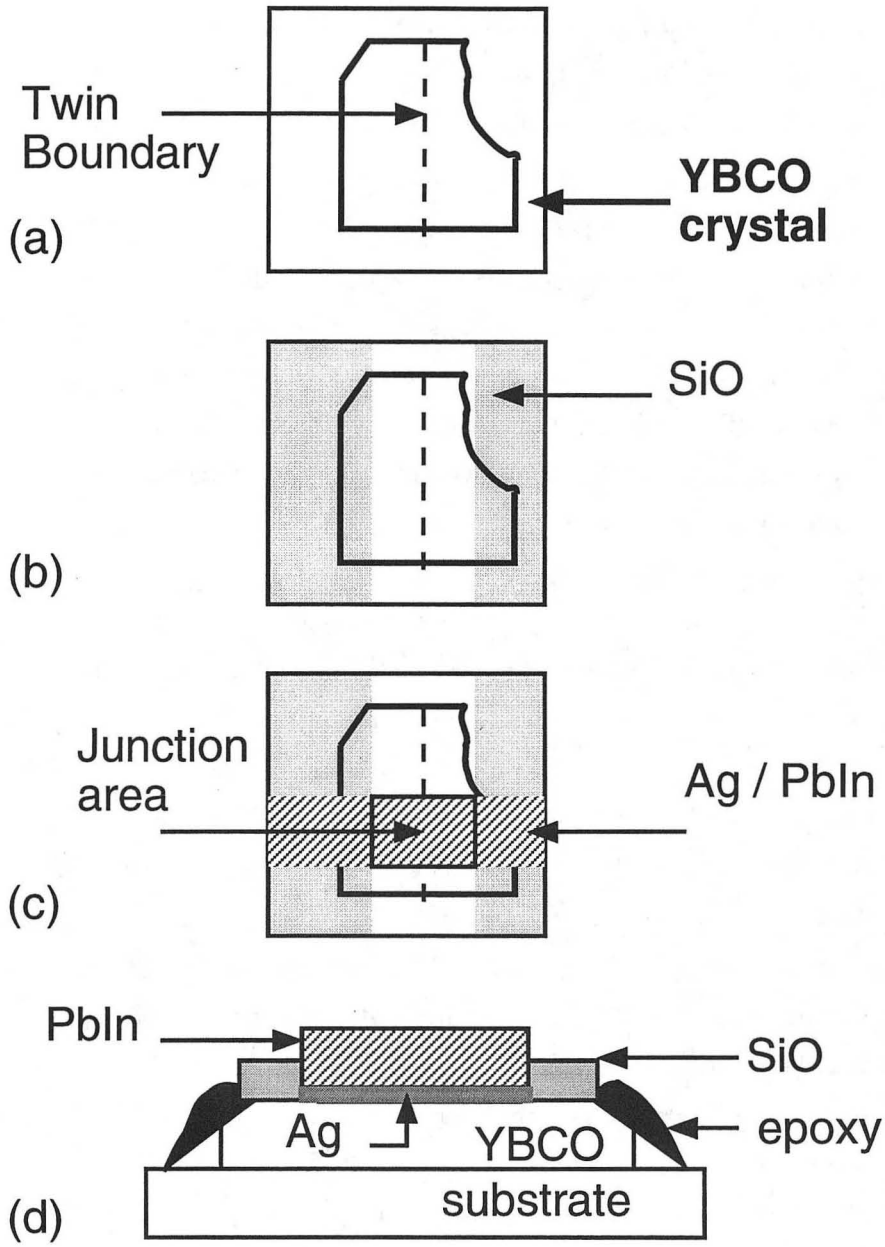

Figure 4.3: Steps in the fabrication procedure. (a) mounting of the crystal, (b) SiO evaporation, (c) evaporation of the Ag/PbIn counterelectrode. (d) shows a crossection of the junction.

the Pb film from rapid degradation in air. The thin Ag layer deposited immediately before the PbIn serves as a diffusion barrier to prevent the diffusion of the Pb counterelectrode into the $YBa_2Cu_3O_{7-\delta}$. The effectiveness of the Ag layer in preventing the diffusion of Pb indicates that the Ag layer is uniform despite the fact that it is only 2.5 nm thick. The junction resistance is typically reduced by one or two orders of magnitude by the Ag layer. The nature of the high quality tunnel junctions is not influenced by the presence of Ag layer, as demonstrated by the unchanged value of the Pb gap, the hysteretic I-V characteristics and the sharp Fiske modes. The Ag layer is too thin to introduce a proximity effect in the Pb counterelectrode, which is evident from the unchanged value of the Pb gap. The quasiparticle tunneling characteristics displaying low leakage current below the Pb gap indicate the existence of an intrinsic tunneling barrier formed at the surface of $YBa_2Cu_3O_{7-\delta}$. As shown in Fig. 4.3 (c), the shorter dimension of the junction is defined by the evaporated Ag/PbIn layer. All junctions fabricated at UCB had a 180 x 240 μm^2 rectangular geometry which was reproducible to within $\approx \pm 10$ μm from junction to junction.

Figure 4.4 (a) is a photograph of junction B1 taken under a Nemarsky optical microscope. A single YBCO twin boundary runs from top to bottom and is clearly visible in the photograph. Areas of light and dark contrast on either side of the boundary are two neighboring twin domains. Each domain is bound on one side by the twin boundary and on the other side by the SiO layer deposited on the surface. The boundary between the light twin domain and the SiO layer is clearly visible on the left side of the picture, whereas the SiO boundary over the darker domain is harder to see because of the similar contrast of the domain and the SiO layer. The dimension of the junction perpendicular to the twin boundary is defined by the opening in the SiO layer (L=240 μm). A white strip running from left to right is the Ag/PbIn counterelectrode evaporated perpendicularly to the opening in the SiO layer. The dimension of the junction parallel to the twin boundary is determined by the width of the Ag/PbIn counterelectrode (W=180 μm). The junction area is outlined by the black square in the middle; one cannot see twin domains in the junction area because they are covered by the Ag/PbIn layer. Notice that in this particular junction the twin boundary does not run through the center of the junction, i.e. this junction is deliberately made asymmetric.

Figure 4.5 is a photograph of junctions B2a and B2b fabricated on the crystal whose photograph is shown in Fig. 4.2. The SiO layer defines top and bottom dimensions

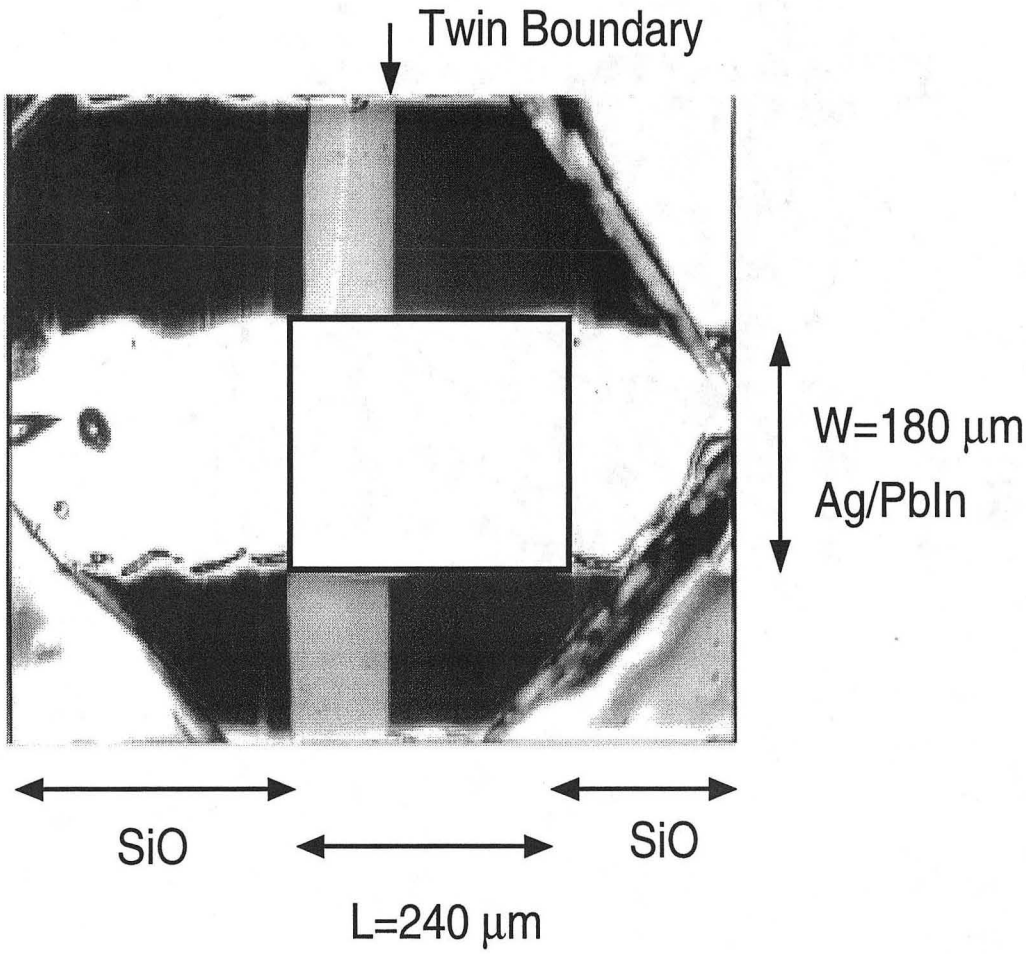

Figure 4.4: Nemarsky photograph of junction B1. The twin boundary runs vertically through the center of the photograph. The Ag/PbIn strip is the horizontal white region.

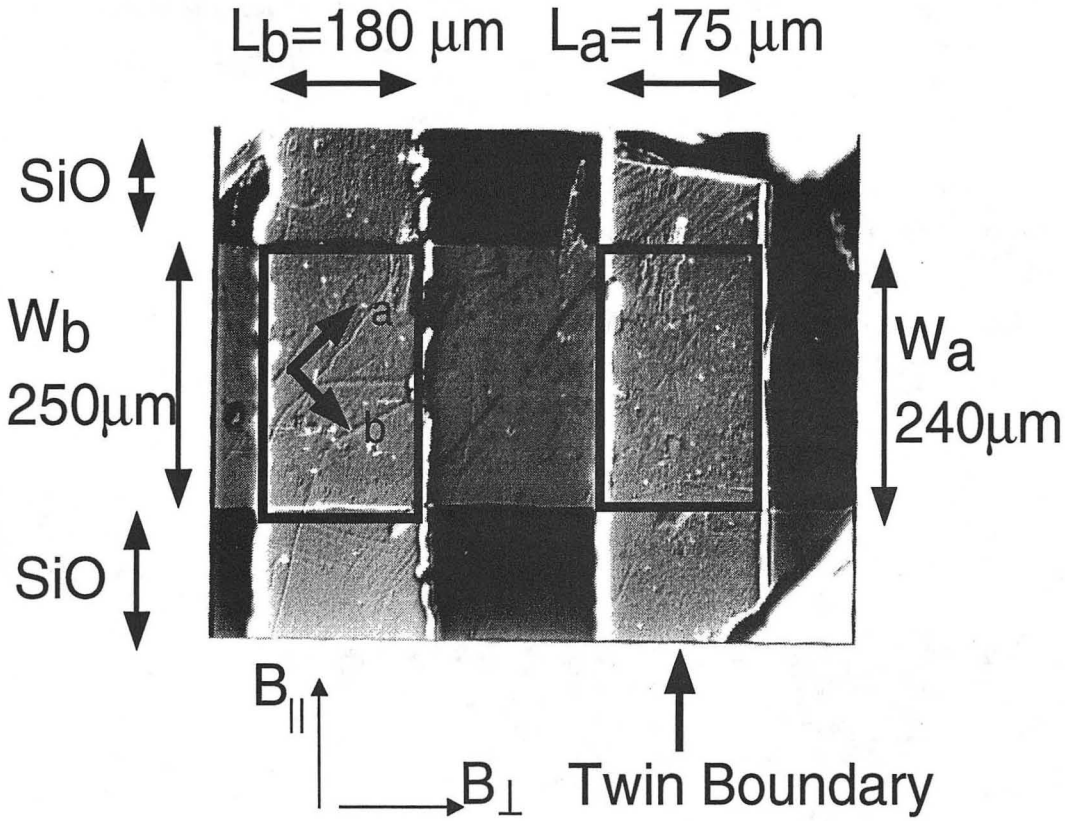

Figure 4.5: Nemarsky photograph of junctions B2a (right) and B2b (left), fabricated on the same crystal, whose photograph is shown in Fig. 4.2. The counterelectrodes are the two vertical white strips. The twin boundary in junction B2a is covered by the Ag/PbIn film on the right.

of the junctions in this figure. The two white strips running from top to bottom are the two Ag/PbIn counterelectrodes. They define the left and right dimensions of the junctions. Junction B2a, located on the right, was fabricated symmetrically over a twin boundary. In this figure, as well as in Fig. 4.2, the boundary runs from top to bottom of the figure. This boundary cannot be seen in Fig. 4.4 (b) because it is covered by the Ag/PbIn layer on the right. However, the areas of different contrast on the two sides of junction B2a indicate two twin domains with orthogonal orientations of crystal axes; the boundary between these domains lies exactly in the middle of the junction. Junction B2b located on the left side is a control junction fabricated on a single twin domain on the same crystal as junction B2a. The geometric dimensions of junction B2b are the same as those of junction B2a. Notice that areas of the crystal seen on either side of junction B2b are of the same contrast, illustrating that this is a single domain junction. The geometric areas of the two junctions are outlined by two black rectangles. The a- and b-crystal axes are shown schematically in Fig. 4.5. They are oriented at a 45° angle with respect to the twin boundary and rectangular dimensions of both junctions.

4.3 Measurements

A schematic diagram of the experimental apparatus is shown in Fig. 4.6. Tunneling measurements were done at liquid He temperatures. To mitigate the problems of trapped magnetic flux and external interference, the dewar was surrounded by two μ-metal shields. The Josephson junctions were mounted at the end of a cryogenic probe, and cooled slowly from about 125 K to 4.2 K to minimize trapped flux. We measured current-voltage (I-V) characteristics by current biasing the junction and reading the voltage drop across it with a room temperature voltage amplifier. The current bias was continuously swept from positive to negative and back to positive direction at a frequency of about 10 Hz, which allowed us to monitor I-V curves continuously on the oscilloscope. All junctions displayed low leakage, superconductor-insulator-superconductor tunneling characteristics similar to those seen in previous work [5, 32, 34, 33, 35] (see inset to Fig. 4.7), including a well-defined Pb energy gap (≈ 1.4 meV) and sharp Fiske modes, indicating a high quality tunneling barrier. To record magnetic field interference patterns, we applied a uniform field in the plane of the junction by means of two orthogonally mounted Helmholtz pairs. By varying the ratio of currents passing through the Helmholtz pairs, we could vary the angle of the magnetic

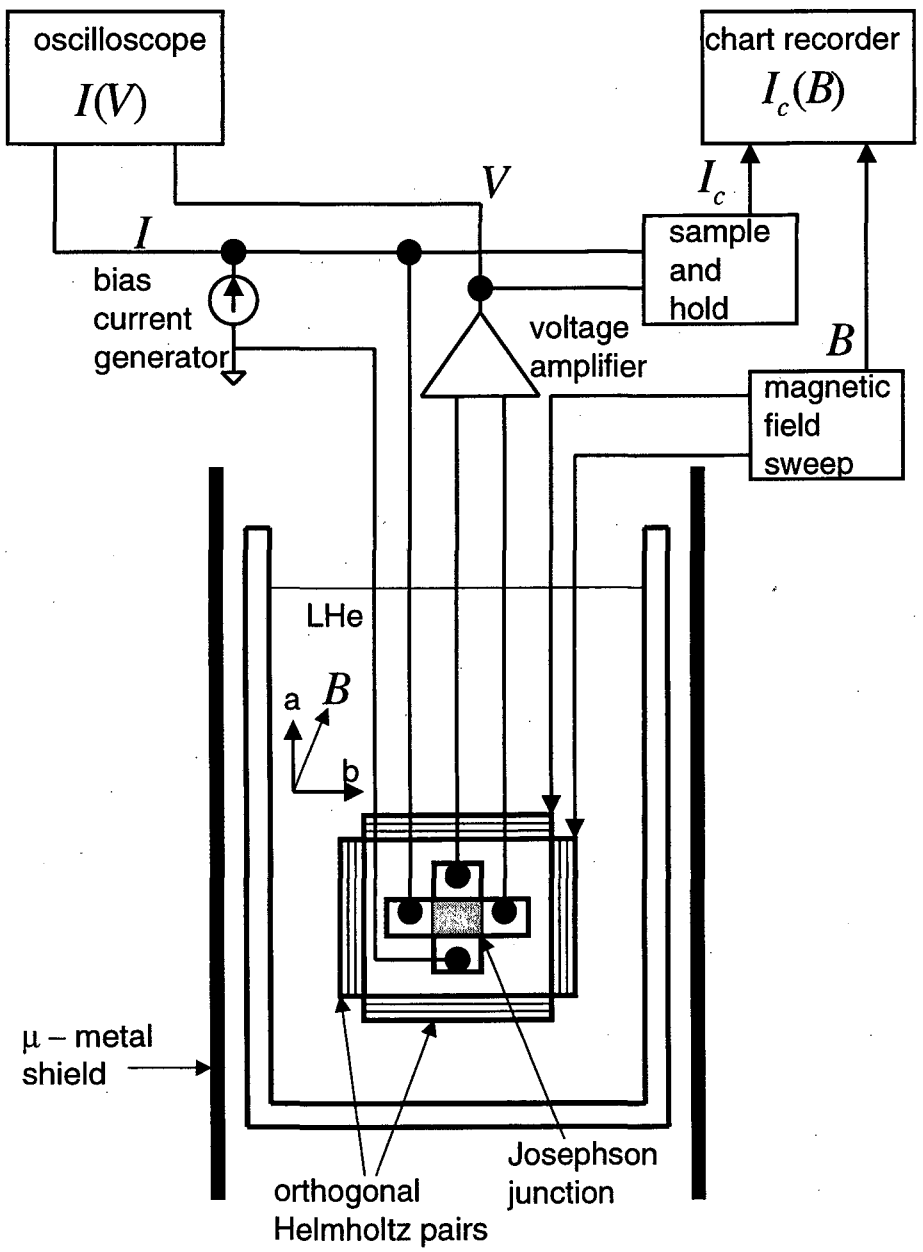

Figure 4.6: Schematic diagram of the experiment.

field relative to the sample. The angular control of the field direction was accurate to $\pm 1°$. The magnitude of the critical current was measured as a function of the applied field using a sample-and-hold stage to store the value of the maximum critical current for a given field. The trigger pulse for the sampling process was derived from the voltage appearing across the junction when it switched from the Josephson to the quasiparticle tunneling branches. The current resolution of the sample and hold stage was limited to a few microamps by the noise at the output of the voltage amplifier.

Results from four samples fabricated at UCB are listed in Table 4.1. We define the geometric asymmetry of the position of the twin boundary within the junction as $\gamma \equiv A_1/A$, where A_1 is the area of the smaller twin domain and $A = A_1 + A_2$ is the total area of the junction. Other junction parameters are as follows: L and W are the dimensions of the junction perpendicular and parallel to the twin boundary, respectively; I_c^0 is the zero-field critical current; I_c^{max} is the maximum critical current for a field applied parallel to the twin boundary; $\eta_{th} \equiv I_c^0/I_c^{\max}$ is the ratio expected theoretically for a given asymmetry parameter [see Eq. (4.5) below]; η is the ratio $I_c^0/I_c^{\max}$ observed in the experiment; and $I_c^{\max}R_N$ is the product of I_c^{max} and R_N, where R_N is the resistance of the junction for voltages above the Pb gap. For comparison, the same parameters for four junctions fabricated at UCSD are listed in Table 4.2 as they were presented in [37].

All of the junctions listed in Tables 4.1 and 4.2 were in the small junction limit, $L/\lambda_J < 1$, except for junctions SD3 and B1 where $L/\lambda_J \approx 1.2$ and 1.5, respectively. Here, λ_J is the Josephson penetration depth defined by

$$\lambda_J^2 = \frac{\Phi_0}{2\pi\mu_0(\lambda_{ab} + \lambda_{Pb} + t)J_c}, \tag{4.1}$$

where λ_{ab} and λ_{Pb} are the values of the London penetration depth in YBCO and Pb, respectively, and J_c is the critical current density in the junction. As shown in Tables 4.1

Table 4.1: Parameters of junctions fabricated at UCB.

	L (μm)	W (μm)	γ	I_c^0 (μA)	$I_c^{\max}$ (μA)	η_{th}	η	$I_c^{\max}R_N$ (mV)
B1	240	180	0.33	780	1550	0.49	0.50	0.68
B2a	175	240	0.40	82	158	0.28	0.52	0.51
B2b	180	250	0.0	300	300	1.00	1.00	0.75
B3	160	250	0.50	10	37.6	0.0	0.27	1.00

Table 4.2: Parameters of junctions fabricated at UCSD.

	L (μm)	W (μm)	γ	I_c^0 (μA)	$I_c^{\max}$ (μA)	η_{th}	η	$I_c^{\max}R_N$ (mV)
SD1	250	445	0.45	226	396	0.14	0.57	1.03
SD2	150	330	0.47	193	815	0.08	0.24	0.90
SD3	250	280	0.48	300	2010	0.06	0.15	1.03
SD4	250	350	0.42	0	28	0.22	0	0.90

and 4.2, the $I_c^{\max}R_N$ products lie between 0.5mV and 1mV, even though the values of $I_c^{\max}$ and R_N vary by more than an order of magnitude. This result suggests that variations in $I_c^{\max}$ and R_N arise from variations in the properties of the tunneling interface and that the properties of the YBCO crystals do not change substantially from sample to sample.

4.4 Experimental Results

The main result of the experiment is an observation of the local minimum at $B = 0$ in the magnetic field interference patterns of all seven twin boundary junctions fabricated at UCB and UCSD. Figure 4.7 shows $I_c(\mathbf{B})$ for junction SD2 with the field parallel to the twin boundary. In addition to a deep local minimum in I_c at $B = 0$, we observe a high degree of symmetry under reversal of both field and current, indicating that the junction is free of significant trapped flux and that self-field effects are negligible. Self-fields are expected to become important for long junctions in which $L/\lambda_J > 1$, whereas for this junction $L/\lambda_J = 0.55$. The inset in Fig. 4.7 shows the tunneling I-V characteristic of this junction with a very low leakage current below the Pb gap. This I-V characteristic indicates that the insulating barrier is uniform and the tunneling transport occurs predominantly along the c direction.

Figure 4.8 (a) shows $I_c(\mathbf{B})$ patterns obtained for junction B2a. When a magnetic field is applied *parallel* to the twin boundary, we observe a local minimum at $B = 0$ and two global maxima located on either side of the $B = 0$ axis. For a field applied *perpendicular* to the twin boundary, the resulting $I_c(\mathbf{B})$ displays a conventional Fraunhofer-like behavior. The global maximum of $I_c(\mathbf{B})$ pattern in a perpendicular field occurs at $B = 0$, and it coincides exactly with the value of the local minimum in $I_c(\mathbf{B})$ in a parallel field. Both patterns in Fig. 4.8 (a) are symmetric with respect to the direction of the applied field.

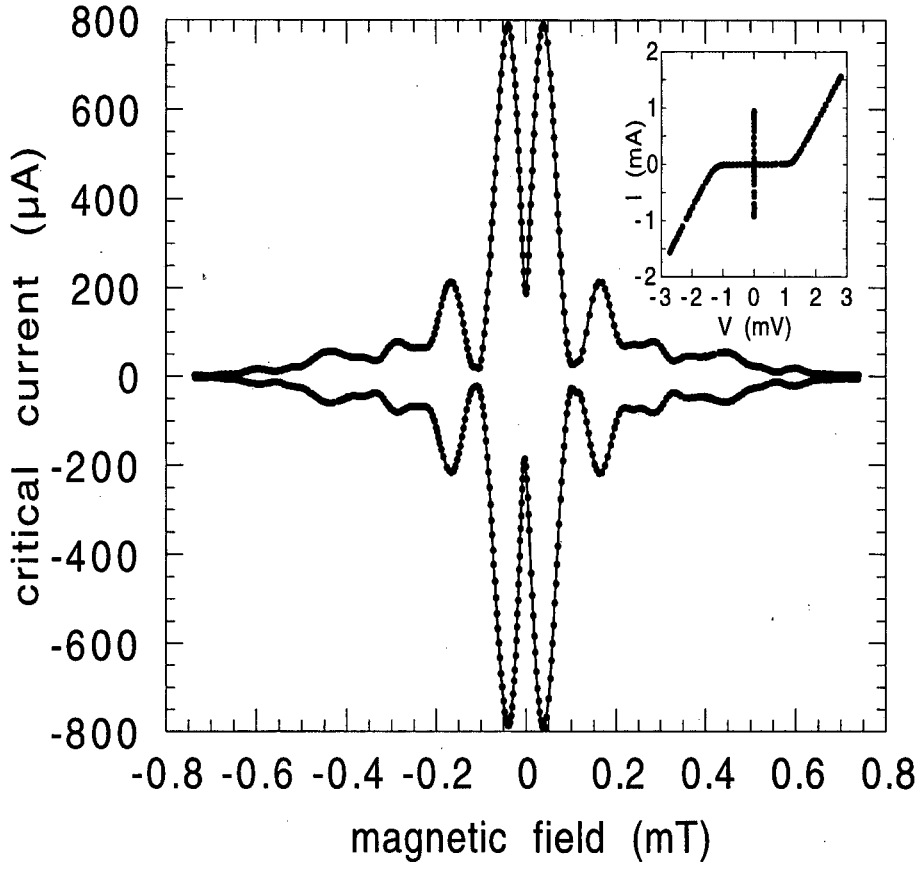

Figure 4.7: $I_c(\mathbf{B})$ for junction SD2 (γ=0.47). The magnetic field is applied parallel to the twin boundary. Inset: I-V characteristic at 1.3 K and 0.0413 mT.

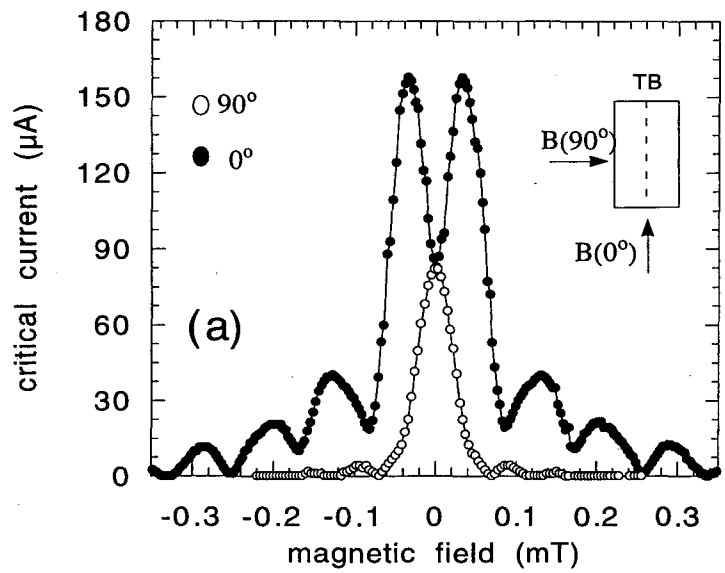

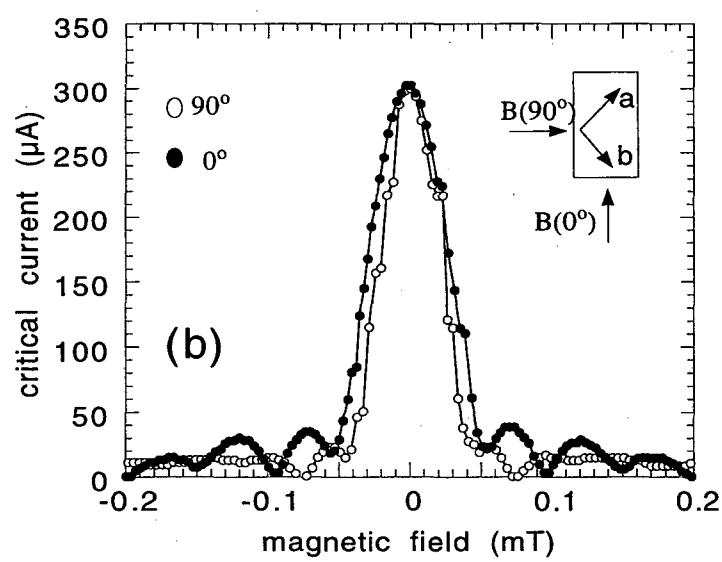

Figure 4.8: (a) $I_c(\mathbf{B})$ for junction B2a (γ=0.4) for fields applied perpendicularly $B(90°)$ and parallel $B(0°)$ to the twin boundary. (b) $I_c(\mathbf{B})$ for junction B2b grown on a a single twin domain, showing conventional, Fraunhofer-like behavior for two orthogonal field directions $B(90°)$ and $B(0°)$.

Figure 4.8 (b) shows $I_c(\mathbf{B})$ for a control junction B2b grown over a *single* domain on the same crystal as junction B2a (see Fig. 4.5). We observed conventional, Fraunhofer-like behavior, with a global maximum at $B = 0$, for fields applied parallel, $B(0°)$, and perpendicular, $B(90°)$, to the junction width; the field directions are illustrated schematically in Fig. 4.8 (b). The ratio of the periodicities for fields $B(0°)$ and $B(90°)$ for junction B2b should be $W/L \approx 1.4$. The measured ratio of the difference between the first two local minima at $B < 0$ for two patterns is approximately 1.5, which is in good agreement with what we expected from the junction geometry. We applied a magnetic field at different angles ϕ with respect to the junction width, which is the direction of $\phi = 0$; this direction corresponds to the field applied parallel to the twin boundary in junction B2a. We observed conventional, Fraunhofer-like behavior, with a global maximum at $B = 0$, in junction B2b for all values of ϕ.

As we discussed in chapter 3, YBCO is orthorhombic, and therefore the order parameter is expected to be of the form $d + \varepsilon s$ within a single domain. The Pb c-axis junction couples only to the s-wave component, so that a Fraunhofer-like $I_c(\mathbf{B})$ for all angles ϕ, as seen in Fig. 4.8 (b), is expected. The contrast between the data shown in Fig. 4.8 (b) and the behavior observed in the other seven junctions makes it clear that the minima at $B = 0$ in those junctions are due to the presence of the twin boundary. The results presented in Fig. 4.8 (a) and (b) agree precisely with predicted outcome of this experiment (see discussion in chapter 3), which was based on the assumption that the order parameter of YBCO is of mixed d+s symmetry with a d-wave component dominant and the s-wave component changing sign across the twin boundary.

The $I_c(\mathbf{B})$ pattern of the twin boundary junction is expected to be periodic with a period of $2\Phi_0$ as opposed to the Φ_0 periodicity of a conventional Fraunhofer pattern, as illustrated in Fig. 3.2. We compare the periodicities of the $I_c(\mathbf{B})$ patterns for junctions B2a and B2b for fields perpendicular to the junction lengths, i.e. $B(0°)$. The geometric lengths of junctions B2a and B2b are 175 μm and 180 μm, respectively; thus, for $B(0°)$, we expect the periodicity of $I_c(\mathbf{B})$ for junction B2a to be larger by a factor of two than that for junction B2b. Here, we have assumed the same values for the penetration depth in both junctions, which is a reasonable assumption for junctions fabricated on the same crystal. The experimentally determined ratio of distances between two adjacent minima for $B < 0$ for junctions B2a and B2b is approximately 2.05. This factor is in excellent agreement with the anticipated factor of 2. It shows that not only the existence of the local minimum

at $B = 0$ but also the doubling of the periodicity in $I_c(\mathbf{B})$ occurs in the twin boundary junctions.

Figure 4.9 shows $I_c(\mathbf{B})$ for junction B2a as a function of the angle ϕ between the twin boundary and $\mathbf{B}$. For $\phi = -90^o$, we observe a conventional, Fraunhofer-like pattern. As we increase ϕ, two local maxima in critical current develop on either side of the $B = 0$ axis, while the value of $I_c(B = 0)$ remains constant. These two peaks have a maximum height at $\phi = 0^o$, and decrease again as we increase ϕ to $+90^o$. The behavior shown in Figs. 4.7, 4.8 (a), and 4.9 was observed in all junctions grown across a twin boundary.

The observed, reproducible dependence of the critical current on the angle ϕ strongly suggests an interpretation in terms of a sign reversal of the s-wave component of the YBCO order parameter across the twin boundary. For an s-wave component which changes sign across the twin boundary, and for $\mathbf{B}$ making an angle ϕ with respect to the boundary, we can write the critical current of a small ($L \ll \lambda_J$), uniform junction with an asymmetry parameter γ as

$$\begin{aligned} I_c^2(\Phi,\gamma) &= I_0^2 \left| \frac{sin(\pi\Phi_x/\Phi_0)}{(\pi\Phi_x/\Phi_0)} \right|^2 \times \\ &\left| \frac{1+\cos^2(\pi\Phi_y/\Phi_0) - \cos(2\gamma\pi\Phi_y/\Phi_0) - \cos[2(\gamma-1)\pi\Phi_y/\Phi_0]}{(\pi\Phi_y/\Phi_0)^2} \right|, \end{aligned} \tag{4.2}$$

where fluxes Φ_x and Φ_y are applied parallel and perpendicular to the twin boundary, respectively. They are given by

$$\Phi_x = B(\lambda_{ab} + \lambda_{Pb} + t)Lcos\phi \tag{4.3}$$

and

$$\Phi_y = B(\lambda_{ab} + \lambda_{Pb} + t)Wsin\phi. \tag{4.4}$$

Here, I_0 is the maximum critical current of the junction with no sign reversal, B is the magnitude of the applied field, λ_{ab} and λ_{Pb} are the values of the penetration depth in YBCO and Pb, respectively, and t is the thickness of the tunneling barrier. For a field applied parallel to the twin boundary of an asymmetric junction, Eq. (4.2) simplifies to

$$\begin{aligned} I_c^2(\Phi,\gamma) &= (I_0\,\Phi_0/\pi\Phi)^2 \times \\ &\Big[1+\cos^2(\pi\Phi/\Phi_0) - \cos(2\gamma\pi\Phi/\Phi_0) - \cos[2(\gamma-1)\pi\Phi/\Phi_0]\Big], \end{aligned} \tag{4.5}$$

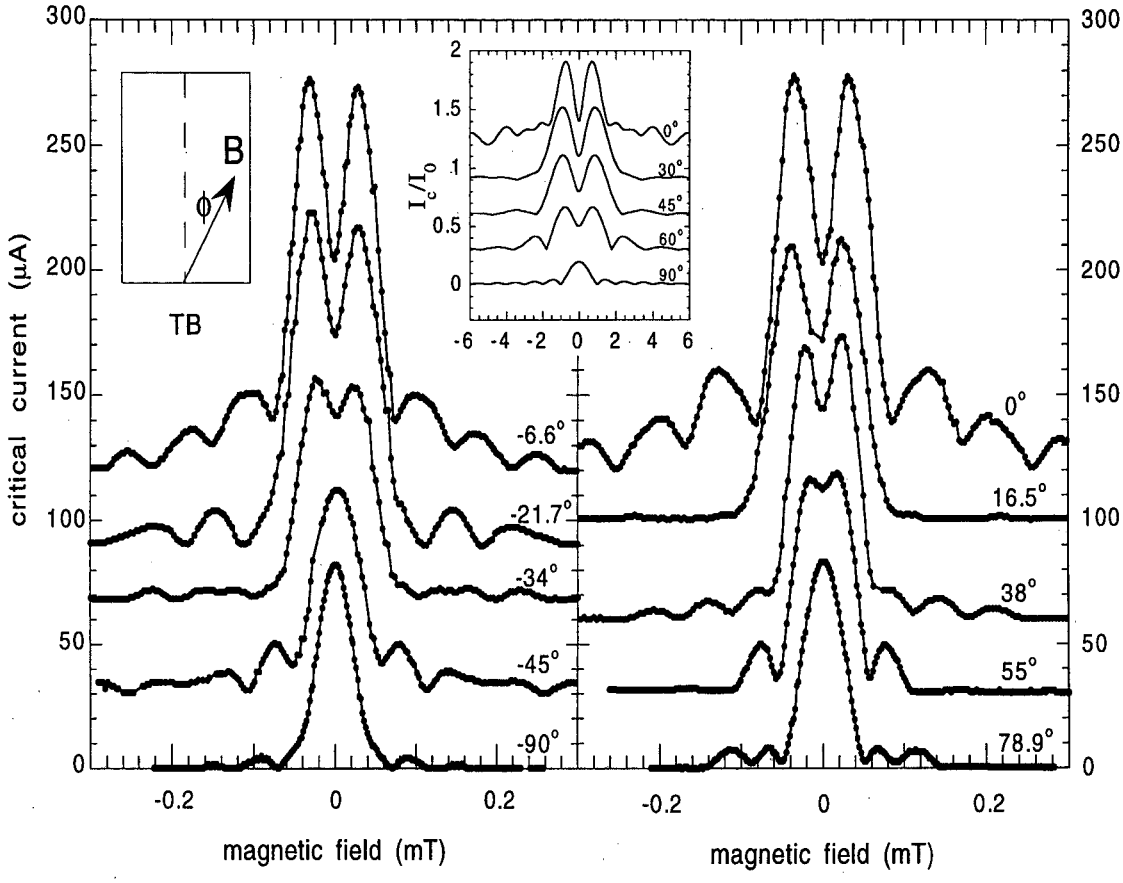

Figure 4.9: $I_c(\mathbf{B})$ for junction B2a (γ=0.4) for ten values of angle ϕ relative to the twin boundary (TB). Successive plots are offset vertically by 30 μA. Center inset: Computed values of I_c/I_0 vs Φ/Φ_0 for a junction with a sign reversal of the s-wave component and γ=0.4. Successive plots are offset vertically by 0.3.

where $\Phi = B(\lambda_{ab} + \lambda_{Pb} + t)L$ is the magnetic flux penetrating the junction. For $\gamma = 0$, Eq. (4.5) yields the Fraunhofer pattern of a purely s-wave junction

$$I_c = I_0 \left| \frac{\sin(\pi\Phi/\Phi_0)}{(\pi\Phi/\Phi_0)} \right|. \tag{4.6}$$

For $\gamma = 0.5$, we find

$$I_c = I_0 \left| \frac{\sin^2(\pi\Phi/2\Phi_0)}{\pi\Phi/2\Phi_0} \right|. \tag{4.7}$$

Equations (4.6) and (4.7) are identical to results for the d-wave corner junction [4] as we have already discussed in chapters 2 and 3.

In the inset in Fig. 4.9 we plot $I_c(\mathbf{B})$ calculated using Eq. (4.2) for $\gamma = 0.4$ as a function of the angle ϕ. The predicted behavior is similar to our experimental observations: a continuous variation as a function of ϕ from a local minimum at $B = 0$ for fields parallel to the twin boundary to a global maximum at $B = 0$ for fields perpendicular to the twin boundary.

In Tables 4.1 and 4.2, we summarize $I_c(\mathbf{B})$ for all eight junctions in terms of the ratio $\eta \equiv I_c^0/I_c^{\max}$, where I_c^0 is the critical current at zero field and $I_c^{\max}$ is the largest critical current in a field applied parallel to the twin boundary. We also list η_{th}, the value of η computed from Eq. (4.5) for measured values of γ. For a conventional s-wave junction, or a twin boundary junction in perpendicular applied fields, we expect the maximum I_c to be at $B = 0$, hence $\eta_{th} = 1$. For an ideal, symmetric twin boundary junction ($\gamma = 0.5$) in parallel applied fields, we expect $I_c(B = 0) = 0$, hence $\eta_{th} = 0$. For the junction B1, with $\gamma = 0.33$, the predicted and measured values of η are in good agreement. On the other hand, for the one junction (SD4) for which η was measured to be zero, γ was 0.42 and $\eta_{th} = 0.22$. For the remaining five junctions with $0.40 \leq \gamma \leq 0.50$, the measured values of η are consistently higher than the predicted values. The difference might be due to self-field effects, *i.e.* the junctions might not be small enough compared to λ_J so that screening can be neglected. The other possible explanation for this discrepancy is a nonuniform current density in the junction. We will discuss these and other issues in the next chapter.

Chapter 5

Discussion and Conclusions

In discussing the results, one must address a number of issues that can impact the experimental results and their interpretation. Issues of trapped magnetic flux, long junction effects, states with a broken time reversal symmetry and nonuniform current density in the junction must be considered in order to determine unambiguously the pairing symmetry of YBCO. A discussion that follows will reinforce the most natural interpretation of our experiments, which is in terms of the dominant d-wave symmetry of YBCO with a sign reversal of the orthorombically induced s-wave component of the order parameter. In conclusion, we will discuss what we currently know and what we don't know about the pairing symmetry and the mechanism of superconductivity in cuprates.

5.1 Effects of trapped magnetic flux

Could the large observed minima in I_c at $B = 0$ arise from trapped vortices in a purely s-wave superconductor? A vortex containing flux Φ_0 trapped within the plane of the twin boundary, at an angle $0^o < \theta < 90^o$ relative to the c-axis, would have the same effect as a phase shift of $2\pi \sin\theta$ at the boundary. For a field applied in the plane of the junction, the phase shift of $2\pi \sin\theta$ will distort the magnetic field interference pattern. The largest distortion of the $I_c(\mathbf{B})$ pattern occurs if a vortex couples a total integrated flux of $\Phi_0/2$ in the plane of the junction. We have simulated the effect of such a vortex located at different places along the junction. The expected $I_c(\mathbf{B})$ patterns are asymmetric in $\mathbf{B} \rightarrow -\mathbf{B}$. Similar simulations have been performed by Wollman *et al.* for corner SQUID experiments in the a-b plane; see Fig. 13 in [43]. Our simulations indicate that a symmetric $I_c(\mathbf{B})$ with a local

minimum at $B = 0$ occurs only for a point vortex trapped in the twin boundary plane in such a way that the component of the flux perpendicular to the plane of the junction is exactly $\Phi_0/2$. In this case, the angle between the vortex and the c axis is $\theta = 30^o$. A trapped vortex out of the plane of the twin boundary exhibits the same behavior, except that the minima in $I_c(\mathbf{B})$ occur at magnetic field angles parallel to the direction of the vortex. The highly reproducible symmetry of the data for any field direction, from sample-to-sample and from run-to-run on a given sample, indicate that trapped magnetic flux is an extremely unlikely explanation of the data.

5.2 Self-field effects

Self-field effects occur in junctions that are not small enough compared to λ_J so that screening can be neglected. In particular, the measured values of η in Tables 4.1 and 4.2 are consistently higher than the predicted values η_{th}. Self-field effects can potentially cause this disprepancy, and in the case of a junction with $L \gg \lambda_J$ lead to a conventional Fraunhofer-like pattern due to the formation of a π-vortex in the junction [44]. Kirtley *et al.* [45] have carried out a thorough theoretical analysis of this scenario. They showed that, contrary to the result of [44], the critical current $I_c(\mathbf{B})$ of twin boundary junctions will exibit a local mimimum at $B = 0$ for a field applied parallel to the boundary even in the long junction limit, *i.e.* $L \gg \lambda_J$. However, the depth of the minimum is expected to be lower in the presence of self-fields, *i.e.* η is expected to be higher than η_{th}. For $L/\lambda_J = 1$ the expected η_{th} for a symmetric junction ($\gamma = 0.5$) is no more than 0.12. Most of our junctions are in the regime $L/\lambda_J < 1$; at the same time measured values of η are higher than η_{th} by a factor of two to three. Therefore, self-field effects appear to be too small to explain the discrepancies in η. As shown in [45], a symmetric twin boundary junction, $\gamma = 0.5$, is expected to contain a spontaneously generated magnetic flux even for $L < \lambda_J$. This self-generated flux can be probed using a scanning SQUID microscope in a manner similar to the tricrystal ring experiments [30, 31].

Self-field effects in time reversal invariant junctions were investigated by Agterberg and Sigrist [46] to account for effects of parity symmetry breaking. The parity breaking can occur if either the junction is not invariant under a parity transformation about its center or the current from the leads does not enter and leave a rectangular junction through opposite edges. The former case is refered to as an intrinsic parity breaking, which occurs,

for example, in an asymmetric junction; whereas the latter is an extrinsic parity breaking due to the geometry of the experiment. In our experiments, the current does not enter and leave the junction area through opposite *parallel* edges, but rather through *orthognal* edges. This geometry leads to an extrinsic parity breaking and in this case there are no symmetry relations enforcing $I_c(\mathbf{B}) = I_c(-\mathbf{B})$ even for a symmetric twin boundary junction. In the general case of the asymmetric twin boundary junction with an externally broken parity symmetry, the interplay between a π-shift at the boundary and the geometry of the junction makes quantitative discussion difficult. Agterberg and Sigrist [46] analyzed the configuration relevant to our experiments numerically. They solved the Sine-Gordon equation numerically in the presense of a π-phase shift and the boundary conditions imposed by the geometry that breaks the parity symmetry. They found that for fields applied parallel and perpendicular to the twin boundary, $I_c(\mathbf{B})$ is symmetric with respect to the $B = 0$ axis. However, for intermediate angles the $I_c(\mathbf{B})$ patterns are asymmetric, $I_c(\mathbf{B}) \neq I_c(-\mathbf{B})$, which is a feature seen distinctly in the data in Fig. 4.9. We notice that this asymmetry occurs for low field strengths, *i.e.* B lies within the first maxima, and maximum is close to the $\pi/4$ direction. The asymmetic features of data in Fig. 4.9 were reproduced in model calculations in [46] that provided an explantion for an observed behavior and supported the scenario of sign reversal of s-wave component.

5.3 Nonuniform current density distribution

Another possible source of the discrepancy in η, which would also explain the observation of non-zero supercurrents in heavily twinned samples [5, 32, 33, 34, 35] is the nonuniform current density distribution in the junction. The nonuniform current density can arise from differences in the effective heights of the tunneling barriers between the Pb film and twin domains that are orthogonally orientated. At this point, we do not have a physical picture of why this would be the case in our experiment. A spatially varying barrier height would mean that the value of γ inferred from the relative areas of the domains might not reflect the actual asymmetry in critical current magnitudes. In order to look into the possibility of a nonuniform current density, we calculated $I_c(\mathbf{B})$ patterns assuming different tunneling matrix elements on two sides of the twin boundary. We compare the $I_c(\mathbf{B})$ pattern of junction B2a with the expected pattern for a given geometric asymmetry parameter $\gamma = 0.4$ and a uniform current density (identical tunneling matrix elements for

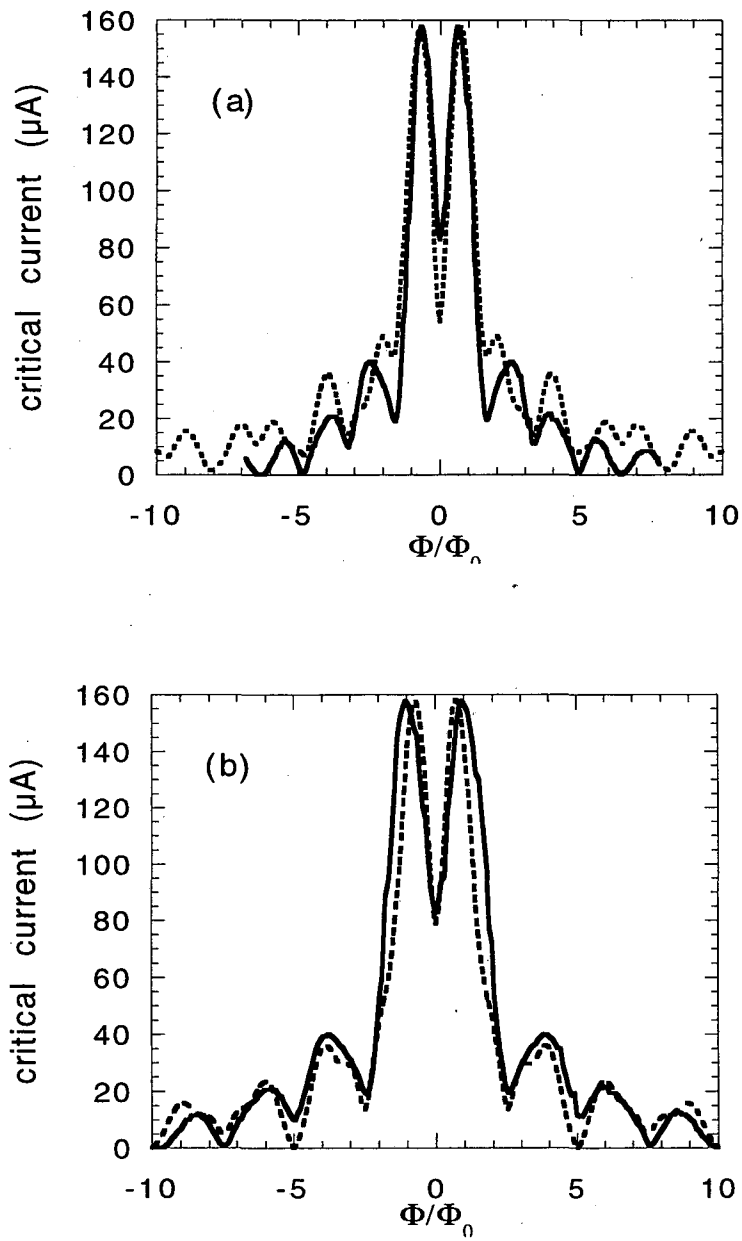

Figure 5.1: $I_c(\mathbf{B})$ for junction B2a, solid line in (a) and (b), for a field parallel to the twin boundary. Simulated $I_c(\mathbf{B})$ for a uniform junction with γ=0.4, dashed line in (a). Simulated $I_c(\mathbf{B})$ assuming a current density in one domain is three times higher than in the other, dashed line in (b).

two twins) in Fig. 5.1 (a). Here, we plot the critical current vs the total flux in the junction. The best fit is shown in Fig. 5.1 (a) assuming an effective junction thickness d_{eff}=220 nm in converting the field to flux values in the experimental curve. We notice that the experimentally observed value of I_c at $B = 0$ is substantially higher than the predicted one, and the periodicity of the experimental curve does not follow the expected behavior.

If we assume a difference in the tunneling matrix elements on the two sides of the boundary, we obtain a good fit to the experimental data as shown in Fig. 5.1 (b). Here, the tunneling matrix element on one side is assumed to be three times higher than on the other. The periodicities of the two curves agree well for d_{eff}=340 nm. We note that the inverse operation of obtaining the current density distribution from the magnetic field interference pattern is not unique [47], *i.e.* many different current distributions can lead to the same $I_c(\mathbf{B})$. Postulating a slightly more complicated current density, one can achieve an almost perfect fit of $I_c(\mathbf{B})$ patterns, although those postulates have no physical basis. The above discussion is intended to make an observation and raise a possible issue in the experiment, since we find that a very simple picture of tunneling probabilities differing by a factor of three leads to a very adequate fit to the experimental data in Fig. 5.1 (b), and can potentially explain the non-zero current in heavily twinned samples.

5.4 Time reversal symmetry breaking at the twin boundary

Two physical mechanisms that were proposed as an explanation for the observation of non-zero supercurrents in heavily twinned samples are: (1) an additional s-wave component to the order parameter induced by the presence of the surface [48], and (2) a localized time-reversal breaking $(d + is)$ state at the twin boundary, due to a continuous rotation of the relative phase between d and s [26].

Scenario (1) is consistent with our results for a single twin or twin boundary junction. The s-wave component induced at the surface adds to the orthorombically induced s-wave contribution. If an orthorombically induced s-wave component has the dominant effect, which is highly likely because orthorombicity is a bulk phenomenon, then the outcome of the experiment will be the same whether the s-wave order parameter at the surface changes its sign or not. The situation becomes different in the heavily twinned limit where the orthorombic s-wave contribution averages to zero. In this case, tunneling into a surface

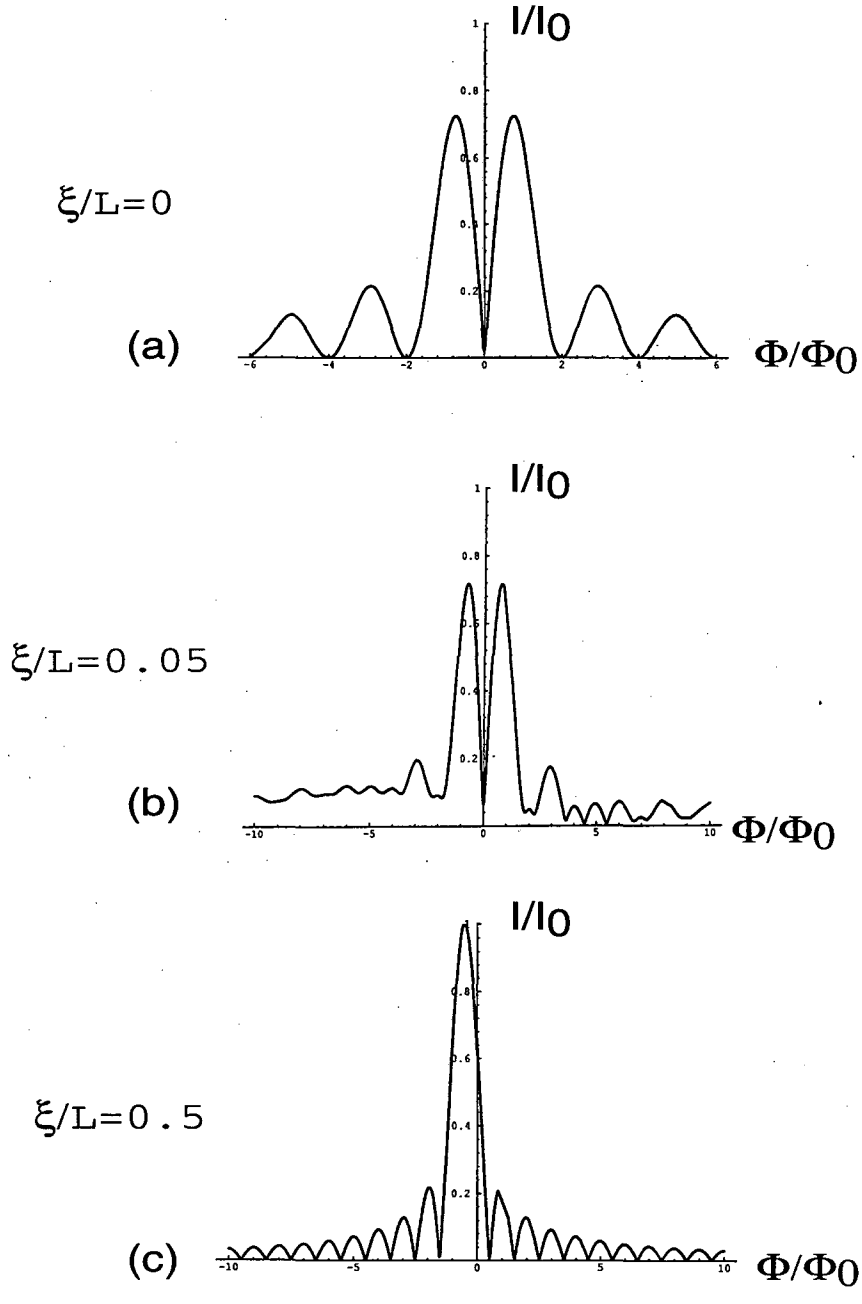

Figure 5.2: Simulated $I_c(\mathbf{B})$ patterns for a symmetric junction in which the relative phase of the s- and d-wave components rotates from 0 to π over the length ξ on either side of the boundary. (a), (b) and (c) correspond to ξ/L=0, 0.05 and 0.5, respectively. Here, L is the total junction length.

induced s-wave component may account for the observed supercurrent.

We note that the $I_c(\mathbf{B})$ data in Fig. 4.7, 4.8 and 4.9 are highly symmetric with respect to the reversal of both field and current. A small asymmetry in $\mathbf{B} \rightarrow -\mathbf{B}$ at intermediate angles in Fig. 4.9 was explained by the parity breaking in an otherwise time invariant junction. Does the symmetry of $I_c(\mathbf{B})$ mean that our results rule out the time reversal symmetry breaking state ? The bulk $(d + is)$ and $(s + id)$ states that evolve into $(d - is)$ and $(-s + id)$, respectively, in the neighboring twin would be consistent with our results. However, the existence of these states has been ruled out by phase sensitive experiments in the a-b plane [4, 43] on detwinned crystals. In these experiments $(d + is)$ and $(s + id)$ states would lead to a phase shift other than π in $I_c(\mathbf{B})$.

The more interesting issue is the local time reversal symmetry breaking at the twin boundary proposed by Sigrist *et al.* [49]. The sign reversal of the s-wave component at a twin boundary can occur via two alternative mechanisms: (1) the magnitude of the s-wave component decreases to zero at the twin boundary and reappears with an opposite sign in an adjacent twin domain, or (2) the magnitude of the s-wave component is constant, but the relative phase gradually aquires a phase shift of π across the twin boundary. In the latter case, the relative phase of s- and d-wave contributions is equal to $\pi/2$ at the twin boundary leading to a $(d + is)$ state, which is a state of broken time reversal symmetry. As suggested in [49], a coherent superposition of supercurrents from $(d + is)$ states at twin boundaries may lead to a nonzero c-axis supercurrent between Pb and a heavily twinned crystal of YBCO.

Local time reversal symmetry breaking at the twin boundary will result in an asymmetric $I_c(\mathbf{B})$ in a junction containing only a single twin boundary, and, hence, could be in principle observed in our experiments. In order to account for these effects quantitatively, we assume that at the boundary the relative phase of s and d-wave components varies linearly from 0 to π over the length 2ξ as

$$\theta(x) = \frac{\pi}{2} + \frac{\pi x}{2\xi} \tag{5.1}$$

for $|x| \leq \xi$ and $\theta(x) = 0$ for $\xi < |x| \leq L/2$, where x is the coordinate along the junction length such that the boundary is located at $x = 0$, and L is the total length of the junction.

Using these expressions for the phase behavior, we derive the resulting $I_c(\Phi)$ as

$$I_c(\Phi) = \left[\frac{sin^2(\frac{\pi}{2} + \frac{\pi\Phi}{\Phi_0}\frac{2\xi}{L})}{(\frac{\pi\Phi}{\Phi_0} + \frac{\pi}{2}\frac{L}{2\xi})} + \left(\frac{cos(\frac{\pi\Phi}{\Phi_0}\frac{2\xi}{L}) - cos(\frac{\pi\Phi}{\Phi_0})}{\frac{\pi\Phi}{\Phi_0}} \right)^2 \right]^{1/2} \tag{5.2}$$

where Φ is the total flux in the junction. Here, we assumed a symmetric junction, and a magnetic field applied parallel to the twin boundary. We confine our attention to this particular geometry, because the asymmetry in $I_c(\mathbf{B})$ is expected to be a maximum at $\phi = 0^o$ for a symmetric junction in a field parallel to the boundary.

Using Eq. (5.2) we generated a series of $I_c(\mathbf{B})$ patterns for different values of ξ/L. The time reversal invariant case ($\xi/L = 0$) is shown in Fig. 5.2 (a) where $I_c(\mathbf{B})$ is perfectly symmetric with respect to the revesal of the field. For the case $\xi/L = 0.05$ shown in Fig. 5.2 (b), we observe noticable asymmetry for positive and negative fields. In the extreme case of $\xi/L = 0.5$, Fig. 5.2 (c), the phase rotates continuously from 0 to π throught the total length of the junction resulting in a conventional Fraunhofer pattern shifted by $\Phi_0/2$. We can use the symmetry of the data to place a limit on the degree of time-reversal breaking at a single boundary. To the limit of our resolution for the data in Fig. 4.7, the maximum peak height asymmetry ratio is smaller than 1.02. This leads to an upper limit for the length of the phase rotation of $\xi/L = 0.017$. Therefore, we find that the length over which the phase angle rotates must be less than $4\,\mu$m. This upper limit is fairly high since one expects ξ to be of the order of the coherence length in the a-b plane of YBCO, which is $\sim$ 1.6 nm. To explore the time-reversal symmetry breaking on a shorter lengthscale, one can potentially use a scanning tunneling microscope.

5.5 Experiments on twinned textures

Having answered the question about what happens at a single twin boundary, we return to the question of why there is a significant supercurrent in heavily twinned samples. Two viable possibilities, namely a surface induced s-wave component and a coherent superposition of $(d + is)$ states at twin boundaries, have been discussed in the previous section. Here, we resort to less exotic scenarios by considering what happens in a twin texture. As we discussed in section 4.1 of chapter 4, multiple twins form twin textures in a heavily twinned crystal. Within a given twin texture, there is a preferred direction because all twin boundaries are parallel to each other. Therefore, a twin texture has an orthorhombic

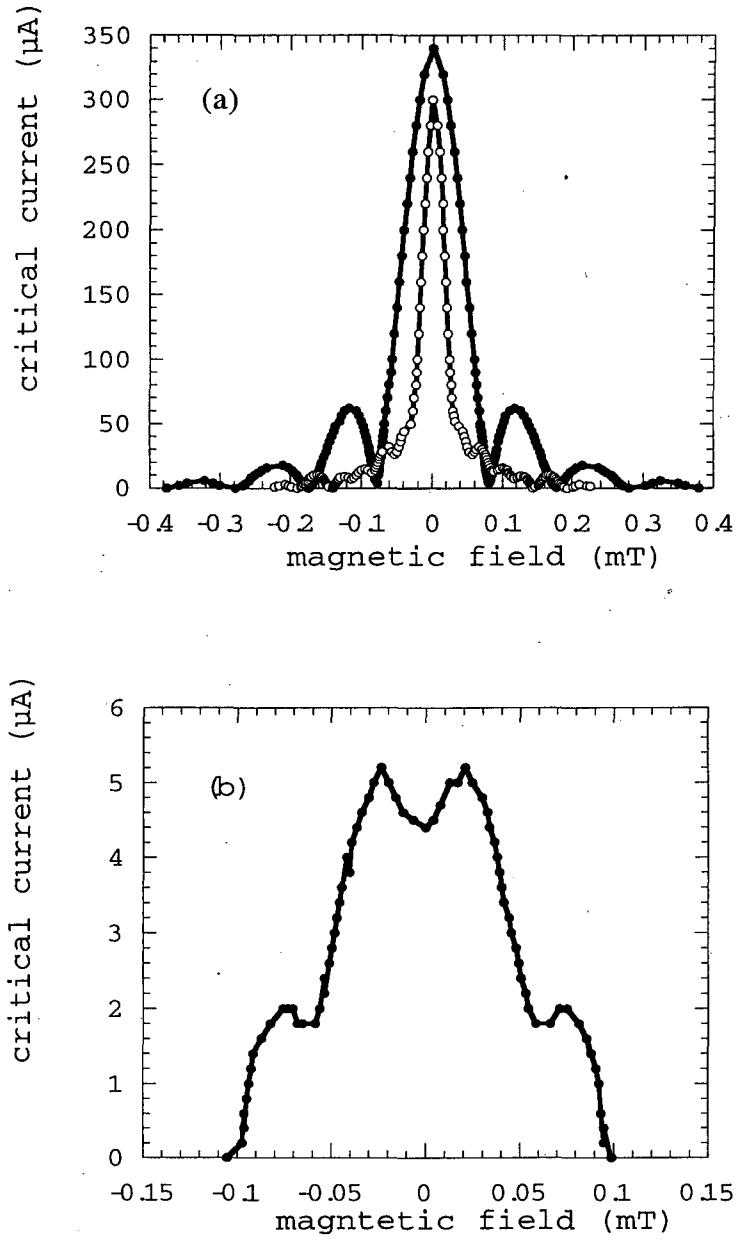

Figure 5.3: (a) $I_c(\mathbf{B})$ for a junction fabricated across two twin textures indicating Frauuhofer-like patterns for both parallel (solid circles) and perpendicular (open circles) fields. (b) another example of $I_c(\mathbf{B})$ in a texture bounadry junction; this pattern displays a local minimum at $B = 0$.

symmetry and a global $(s + d)$ rather than a pure d order parameter is possible; texture dimensions can be as large as $500 \times 500\ \mu m^2$. Therefore, on general symmetry grounds, it is entirely possible to expect a substantial supercurrent from samples containing several textures despite the heavy twinning within individual textures. We considered the possibility of sign reversal of a macroscopic s-wave order parameter across a boundary between two adjacent twin textures as opposed to two adjacent twins. We fabricated c-axis Josephson tunnel junctions across two texures in a manner identical to that of twin boundary junctions, and investigated $I_c(\mathbf{B})$ for fields applied perpendicularly and parallel to the texture boundary. The resulting two $I_c(\mathbf{B})$ patterns from two different crystals are shown in Fig. 5.3. Figure 5.3 (a) shows conventional Fraunhofer patterns for fields applied parallel and perpendicular to the texture boundary. These data indicate that a global s-wave order parameter does not reverse its sign across the boundary as opposed to a reproducible sign reversal in the twin boundary case. Therefore, a heavily twinned crystal can, in principle, be in a global, orthorhombically induced $(s + d)$ state. However, similar data obtained in another experiment, which is shown in Fig. 5.3 (b), displays a local minimum at $B = 0$ indicating the sign reversal of an s-wave component across the texture boundary. The data presented in Fig. 5.3 (a) and (b) point to the existense of global $(s + d)$ domains associated with twin textures in a heavily twinned sample. This picture is somewhat similar to the existence of domains of macroscopic magnetisation in a ferromagnet. It is possible that the sign of a macroscopic s-wave component is preserved across the texture boundary making domains of a given sign larger than texture domains. Details of what occurs at the texture boundary require further exerimental as well as theoretical investigation. In particular, one needs to obtain a better understanding of what drives the sign reversal of the s-component and why in some cases the s-wave part changes its sign across the texture boundary and in some cases does not.

5.6 Conclusions

We find that junctions grown across a single twin boundary of YBCO crystals consistently exhibit a local minimum in $I_c(\mathbf{B})$ at zero magnetic field for fields applied in the plane of the crystal parallel to the twin boundary. As the magnetic field is progressively rotated in the plane of the junction, the value of $I_c(0)$ remains constant while the maxima on either side diminish. The smooth variation of $I_c(\mathbf{B})$ with magnetic field direc-

tion, its symmetry with respect to the reversal of magnetic field and bias current, and the reproducibility of the results imply that trapped flux is an extremely unlikely source of the minima. The results are entirely consistent with a predominantly $d_{x^2-y^2}$ pairing symmetry with a sign reversal of the s-wave component across the twin boundary. To our knowledge, our results provide the first and the only *direct* evidence for an existence of a $(d+s)$ mixed symmetry state in cuprates. This resolves the controversy between two conflicting sets of phase sensitive experiments and establishes that the dominant pairing in YBCO is of $d_{x^2-y^2}$ symmetry. However, our results as well as the results of previous phase sensitive tests do not provide information about the microscopic mechnism leading to the $d_{x^2-y^2}$ pairing. The question of what are the elementary exitations leading to the pairing of superconducting electrons remains open. Future investigations of the physics of high-T_c materials have yet to answer this most fundamental question.

Part II

High-T_c Gradiometers for Biomagnetic Applications

Chapter 6

Superconducting QUantum Interference Devices: principles of operation

A Superconducting QUantum Interference Device (SQUID) is the most sensitive detector of magnetic flux. Any electrical or magnetic quantity that can be converted into magnetic flux can be detected by a SQUID with a sensitivity that is higher than that of any other sensor. Because of this very important property, SQUIDs are used widely in a variety of measurement and instrumentation applications that require very high performance electronics. Applications of SQUIDs include, but are not limited to, the detection of magnetic signals from the human brain and heart, measurements of low voltages and currents in a variety of solid state experiments, detection of gravitational waves and elementary particles, and studying electric and magnetic fields at the surface of the Earth. Below, I will briefly review basic principles of operation of SQUIDs and flux-locked electronics. A detailed discussion can be found in [6].

A direct current SQUID (dc-SQUID) is a superconducting ring interrupted by two Josephson junctions. Magnetic flux threading the ring modulates the superconducting phase around the ring leading to the modulation of the critical current according to

$$I = I_c \left| cos\left(\frac{n\Phi}{\Phi_0}\right)\right|, \tag{6.1}$$

where I_c is the critical current of the device, and Φ is the applied flux. In most, but not all, applications, SQUIDs are operated in a flux-locked loop. The schematic of a dc-SQUID and

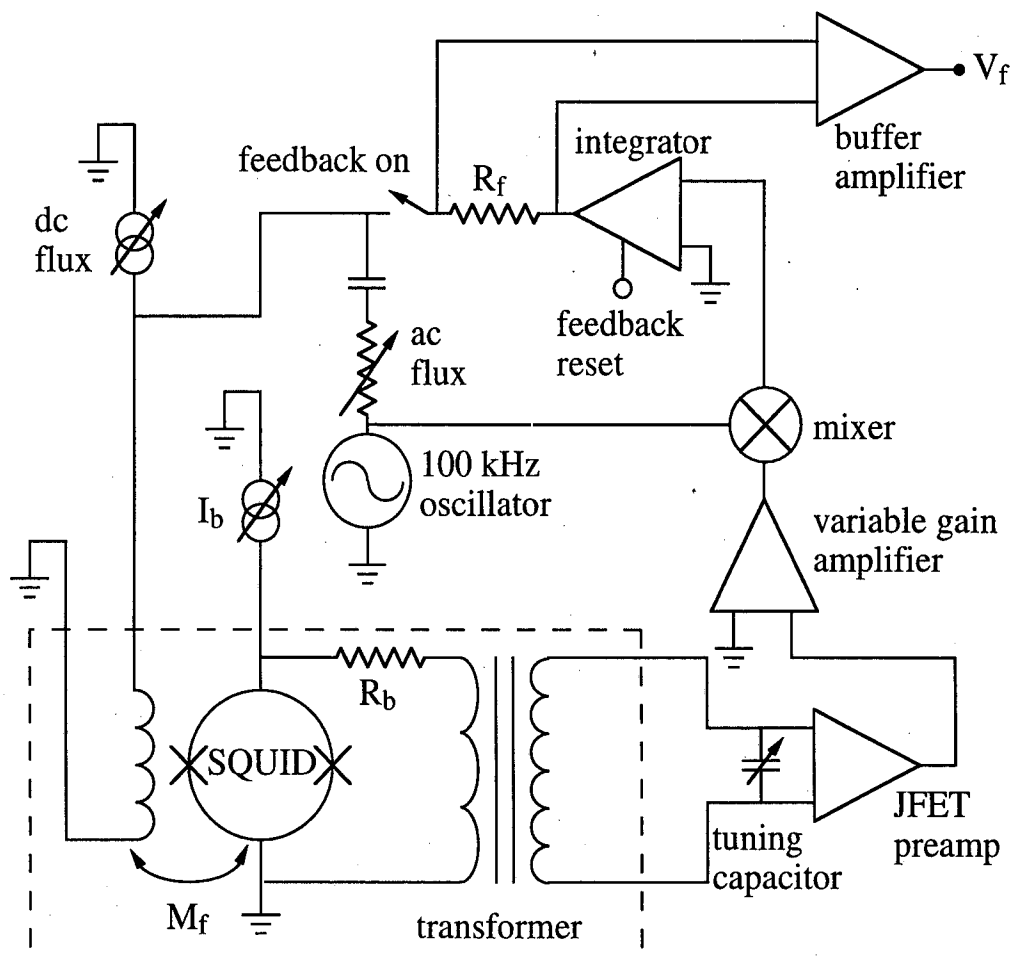

Figure 6.1: Schematic diagram of the flux-locked electronics used to operate a dc-SQUID.

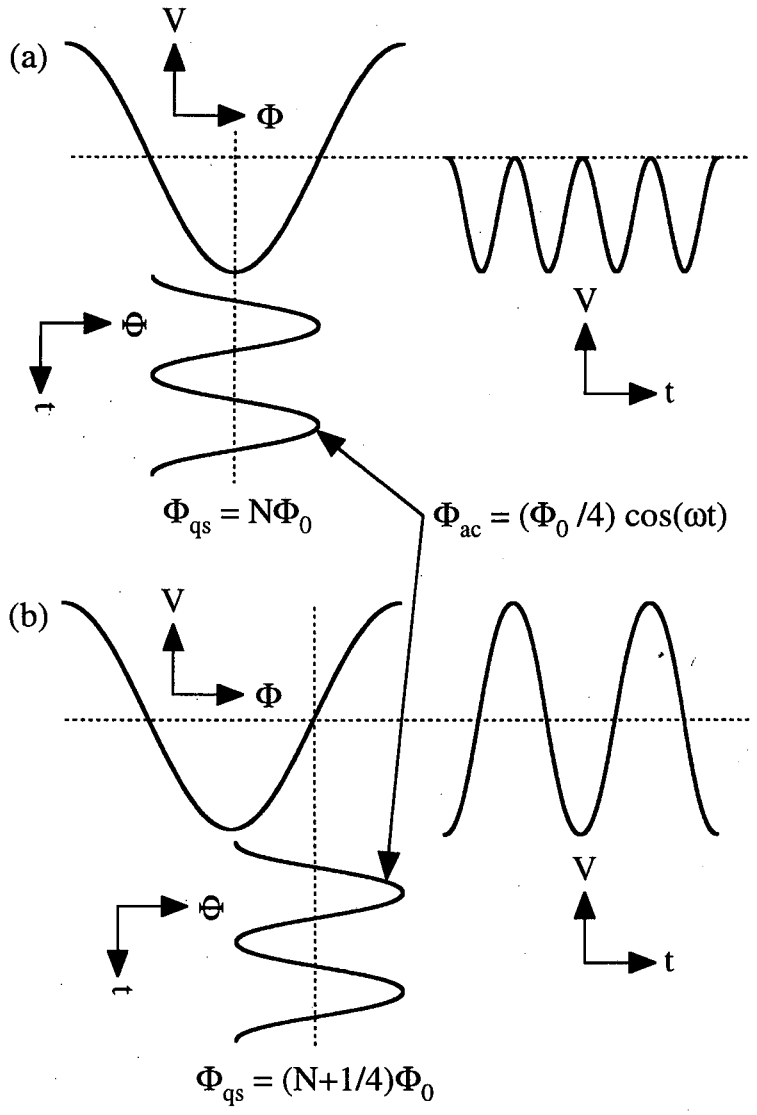

Figure 6.2: Flux modulation scheme for SQUID with (a) $\Phi_{qs} = N\Phi_0$ and (b) $\Phi_{qs} = (N + 1/4)\Phi_0$.

the flux-locked electronics used in our group is shown in Fig. 6.1. The SQUID is biased with a static current source I_b at a value above its critical current. In this case, any change in magnetic flux results in a change in the voltage across the device, leading to the voltage vs flux ($V-\Phi$) modulation curve shown in Fig. 6.2. In a flux-locked scheme, the flux threading the SQUID loop is ac-modulated at 100kHz by means of the modulation coil coupled to it via a mutual inductance M_f. The SQUID voltage is sensed by a transformer and coupled into a tuned preamplifier. In order to achieve optimum noise matching at 100kHz, the JFET-based first stage of the preamplifier is tuned by a trimming capacitor. The signal from the SQUID is amplified by a variable gain amplifier and transferred to a mixer that demodulates the signal. The demodulated signal is integrated, converted to current by a resistor R_f, and fed back to the SQUID via the modulation coil. In some applications, one can use separate coils to perform the modulation and feedback functions.

Here, I will outline the basic principles of flux-locked operation [6]. A $V-\Phi$ curve follows the periodic behavior of the critical current vs flux dependence given by Eq. (6.1); a portion of the $V-\Phi$ curve is shown in Fig. 6.2 (a). The peak-to-peak amplitude of the 100 kHz modulating flux, $\Phi_{ac}(t)$, is adjusted to $\Phi_0/2$. As shown in Fig. 6.2 (a), when the quasistatic flux contains an integer number of flux quanta, $\Phi_{qs} = N\Phi_0$, the resulting voltage is a rectified version of the input signal, *i.e.* its fundamental frequency is 200 kHz. If this signal is referenced to the 100 kHz modulation frequency, the mixer output is zero. If the quasistatic flux in the SQUID is $(N+1/4)\Phi_0$, as shown in Fig. 6.2 (b), the SQUID signal contains the 100 kHz fundamental frequency; at $\Phi_{qs} = (N+1/4)\Phi_0$, the magnitude of 100 kHz signal is a maximum. By gradually changing the quasistatic flux from $(N-1/4)\Phi_0$ to $(N+1/4)\Phi_0$, the mixer output changes from the most negative to the most positive value with the zero output corresponding to $\Phi_{qs} = N\Phi_0$. The slope of this curve at the origin is given by the transfer function $\partial V/\partial\Phi$ of the SQUID at the flux bias of $\pm\Phi_0/4$. As a rule of thumb in practical SQUID designs, we use $\partial V/\partial\Phi = \pi V_{p-p}/\Phi_0$, where V_{p-p} is the peak-to-peak modulation voltage of the SQUID. When the SQUID is used in a feedback loop, any change in the applied flux is converted to an error voltage proportional to $\partial V/\partial\Phi$, and is cancelled by a feedback current flowing through the feedback/modulation coil. The feedback resistor R_f is used to convert the error voltage to the feedback current, and the feedback current is converted into flux through the SQUID by a feedback coil coupled to it via the mutual inductance M_f. In this way, the SQUID and electronics acts as a null detector of the magnetic flux.

Chapter 7

SQUID gradiometers for biomagnetic applications

For decades Superconducting QUantum Interference Devices (SQUIDs) have been successfully used for detection of magnetic fields produced by biomagnetic sources [50]. The most notable biomagnetic applications of SQUIDs are measurements of magnetic signals from the human brain, MagnetoEncephaloGraphy (MEG), and the human heart, MagnetoCardioGraphy (MCG). In these measurements weak magnetic signals from the localized sources are detected in the presence of a much higher background noise. In order to suppress the background noise, one uses either a magnetically shielded room or spatial gradiometers, or often a combination of both. In the case of low temperature superconducting (LTS) SQUIDs, both techniques have long been established, and are now used commercially in a variety of biomagnetic applications [51, 52]. Methods of spatial gradiometry are based on the fact that a biomagnetic signal is produced by a source that can be localized near one of the gradiometer coils, whereas the background noise is present in all coils of the gradiometer and, therefore, can be rejected by signal differencing. To achieve an initial spatial filtering and noise suppression, first-order hardware gradiometers with baselines of a few cm are typically used at the front end of LTS biomagnetic systems. These first-derivative devices in LTS technology are configured either as two loops of niobium wire wound in opposition [53] or as planar thin film devices [54]. In the former case shown schematically in Fig. 7.1 the gradimeter is sensitive to the axial gradient $\partial B_z/\partial z$, and in the latter it measures an off-diagonal gradient such as $\partial B_x/\partial z$. In some cases [55], LTS biomagnetic systems utilize

magnetometers as front-end sensors and gradiometer formation is done electronically.

The development of practical high temperature superconducting (HTS) SQUIDs has received much attention since the original discovery of HTS materials more than a decade ago. It soon became evident that HTS hardware gradiometers cannot utilize the same principles as their LTS counterparts. The lack of a suitable superconducting wire precludes the development of HTS axial wirewound gradiometers. A straightforward generalization of LTS planar gradiometers to HTS technology is difficult and expensive because it requires fabrication of multiple layers of HTS thin films on large substrates. This is not a technologically viable option at this time. To overcome these problems, a number of alternative techniques for gradiometer formation have been demonstrated in HTS technology. The majority of the first-order order hardware devices [56, 57, 58, 59] involve a gradiometric coil patterned from a single layer of YBaCuO film in the form of two loops directly-coupled to the SQUID fabricated on the same chip. A second-order gradiometer based on the same principle have been demonstrated as well [60]. In an alternative approach [61, 62, 63, 64] a flux transformer consisting of two pickup loops and a mutiturn input coil are coupled to the SQUID in a flip-chip arrangement. To achieve low noise, these gradiometers must be fabricated from high quality YBaCuO films, which can be done only on small area substrates. However, the substrate size limits the baseline of the gradiometer to less than 1 cm, which is not sufficient for biomagnetic measurements in an unshielded environment. Gradiometer baselines have been enhanced by coupling a separate flux transformer fabricated on a larger substrate to a gradiometer [65, 66, 67]; baselines of up to 2.1 cm have been demonstrated using this method.

To achieve longer baselines, of the order of 10 cm, in an axial geometry gradiometers have been formed electronically by subtracting the outputs of two or more fluxed-locked SQUID magnetometers. A particularly interesting concept is the three-SQUID gradiometer [68], which has been demonstrated and implemented in a variety of applications including underwater mine detection from mobile platforms. Unshielded MCG have been demonstrated previously with electronic HTS gradiometers utilizing both rf- and dc-SQUIDS [69, 70, 71, 72, 73, 74, 75, 76]. However, electronic gradiometers are difficult to implement in a practical system, because they impose severe constraints on dynamic range, slew rate and linearity of the flux-locked electronics. These limitations ultimately limit the degree to which one can balance the system and reject background noise. To achieve sufficient balance levels, the electronic gradiometers were supplemented by mechanical balancing techniques

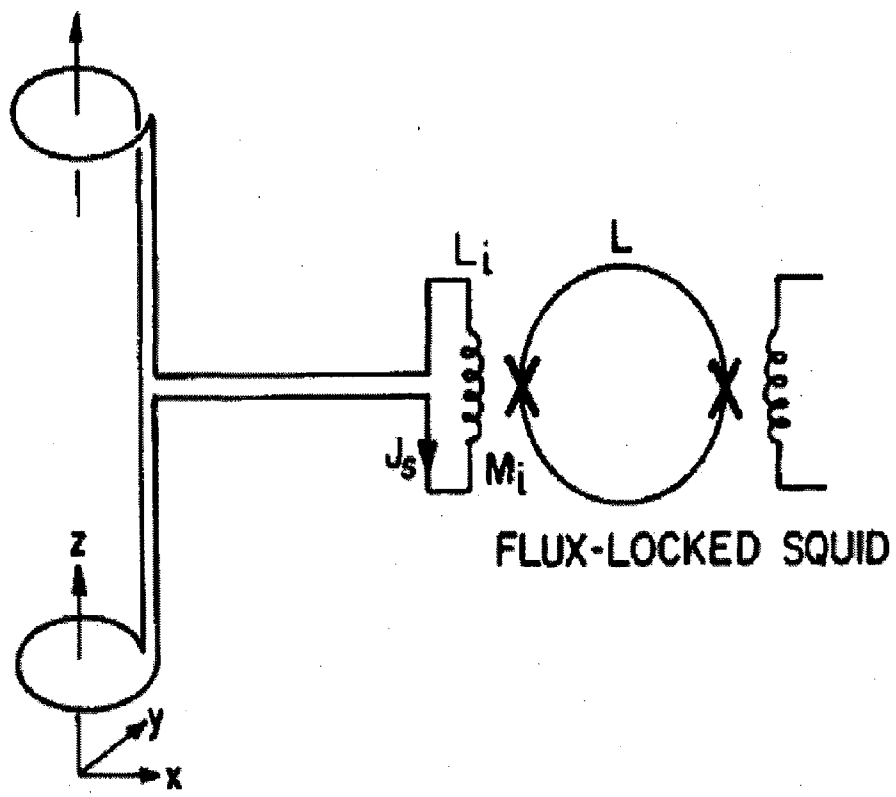

Figure 7.1: Schematic diagram of the wire-wound first-order gradiometer; from [6].

such as cardanic suspensions [69, 70] or superconducting plates [72, 73]. Mechanical balancing is not a viable solution for multichannel systems because of its complexity and limited reproducibility.

In our approach, we introduce novel techniques for the construction of long baseline hardware gradiometers in which a planar flux transformer is inductively coupled to a pickup loop of a directly coupled magnetometer. A flux transformer is patterned in a single layer of YBaCuO film deposited on a 10 cm diameter wafer, and can have outer dimensions of up to 9 cm. Both first- [77] and second-order [78] gradiometers have been demonstrated with first- and second-order baselines of 4.8 cm and 3.1 cm, respectively. In a practical first-derivative device, the flux transformer and magnetometer substrates were permanently bonded in a flip-chip arrangement, and balancing in a uniform field was achieved by trimming the pickup loop [79]. The gradiometer baseline of 48 mm and an intrinsic common mode balance of better than one part in a few hundred are comparable to those of biomagnetic LTS devices. Therefore, such HTS sensors can be used in practical systems which fully exploit design techniques and solutions developed for LTS gradiometers. We report the design and testing of such a system in which hardware gradiometers are supplemented by three orthogonally mounted reference magnetometers, and higher levels of balance are achieved in software. The overall system balance with respect to uniform field fluctuations is better than 100 ppm, enabling us to detect the magnetic signal from a human heart in an unshielded environment.

Chapter 8

High-T_C SQUIDs for unshielded operation

Reduction of excess 1/f noise in HTS SQUIDs operated in unshielded environment is essential for biomagnetism. The increase in low-frequency 1/f noise in HTS devices is caused by the thermally activated hopping of weakly pinned vortices which penetrate the YBaCuO film during cooling in the Earth's magnetic field. The most effective way of eliminating the excess noise is to design the superconducting components of magnetometers so that vortices do not enter. It has been shown [80, 81] that for a thin film of YBaCuO patterned as a line of width w the threshold field for vortex entry is approximately $B_{th} = \pi\Phi_0/4w^2$. Based on this argument, magnetometers designed for $B_{th} \approx 100$ μT have been demonstrated [82] by patterning all of the supeconducting material into a mesh with a maximum linewidth of 4 μm.

A directly coupled magnetometer is a single YBaCuO layer HTS device that has a sensitivity suitable for practical applications, and at the same time is amenable to fabrication in large quantities. It consists of a large-area pickup loop connected in parallel with a small-area SQUID fabricated on the same chip. For unshielded operation, all superconducting material in and around the small-area SQUID must be made no wider than 4 μm to avoid direct noise from vortices trapped in the vicinity of the SQUID. The large area pickup loop of the directly coupled magnetometer is expected to add negligible noise when cooled in an external field. As shown in [83], for a square pickup loop of outer and inner dimensions d_1 and d_2 and inductance L_m directly coupled to a SQUID of inductance L, the induced

screening currents contribute an indirect flux noise given by

$$S_{\Phi}^{in}(f) \approx S_{\Phi}^{U}(f)\alpha_d^2(L/L_m)^2(d_1+d_2)/(d_1-d_2). \tag{8.1}$$

Here, $S_{\Phi}^{U}(f)$ is the flux noise spectral density of an unpatterned YBaCuO film, which is typically 10^{-9} Φ_0^2/Hz [84] for YBaCuO films cooled in B_0=50 μT. Taking typical values of d_1=10mm, d_2=2 mm, L_m=4 nH, L=50 pH and α_d=0.9 we estimate $S_{\Phi}^{in} \approx 10^{-13}$ Φ_0^2/Hz, which is about 40 times lower than the typical level of white noise in our directly coupled magnetometers. This large reduction in direct noise is due to the inductance mismatch between the SQUID and the pickup loop, which enters Eq. 8.1 via the factor $L^2/L_m^2 \approx 10^{-4}$. The experimentally observed threshold field for our directly coupled magnetometers is approximately $B_{th} \approx$80 μT [85].

Our standard HTS fabrication process involves the laser deposition of a 180 nm thick film of YBaCuO on a 10×10 mm^2 $SrTiO_3$ bicrystal followed by the evaporation of a 100 nm thick film of Ag over a portion of the YBaCuO film for electrical contacts to the SQUID. The YBaCuO film is subsequently patterned by photolithography and Ar ion milling at normal incidence. We use nominal junction widths of 1 μm and 2 μm on bicrystals with 24° and 30° misorientation angles, respectively.

We used the design introduced in [82] for our slotted-washer SQUID magnetometers. A 200x200 μm^2 square washer of such a device consists of nine 4 μm wide loops separated by 8 μm wide slots. This geometry leads to an estimated SQUID inductance of 50 pH [86, 87, 88], which includes a contribution of about 10 pH from the kinetic inductance of the Josephson junctions. The electrical and magnetic characteristics of slotted-washer SQUIDs are summarized in Table 8.1. For a directly coupled magnetometer the inner and outer loop dimensions are 2 and 10 mm, respectively. The SQUID washer consists of two parallel lines, 100 μm long, 4 μm wide and 4 μm apart; this leads to an estimated SQUID inductance of 50 pH [86, 87, 88]. The electrical and magnetic characteristics of directly coupled magnetometers are summarized in Table 8.2.

Data presented in Tables 8.1 and 8.2 are representative of devices made in our laboratory for use in prototype gradiometer systems. We have not emphasized minimization of processing spreads and compliance with manufacturing tolerances, because our immediate goal was to demonstrate the principles of gradiometer and system designs. The manufacturing issues become very important if one attempts to develop multichannel HTS SQUID systems for commercial applications, in which case the reproducibility of the device speci-

Table 8.1: The electrical and magnetic properties of slotted-washer SQUIDs on 30° bicrystals.

parameter	value	units
SQUID critical current	40	μA
SQUID normal resistance	2.0	Ω
SQUID inductance, L	50	pH
$\partial V/\partial\Phi$ at working point	60	$\mu V/\Phi_0$
Effective area	0.005	mm^2
Flux noise at 1kHz	12	$\mu\Phi_0 Hz^{-1/2}$
Flux noise at 1 Hz	18	$\mu\Phi_0 Hz^{-1/2}$
Threshold field, B_{th}	80	μT

Table 8.2: The electrical and magnetic properties of directly coupled magnetometers on 24° bicrystals.

parameter	value	units
SQUID critical current	50	μA
SQUID normal resistance	1.5	Ω
SQUID inductance, L	50	pH
Pickup loop inductance, L_m	4	pH
Pickup loop area,A_m	20	mm^2
$\partial V/\partial\Phi$ at working point	60	$\mu V/\Phi_0$
Effective area	0.3	mm^2
Flux noise at 1kHz	16	$\mu\Phi_0 Hz^{-1/2}$
Flux noise at 1 Hz	24	$\mu\Phi_0 Hz^{-1/2}$
Threshold field, B_{th}	100	μT

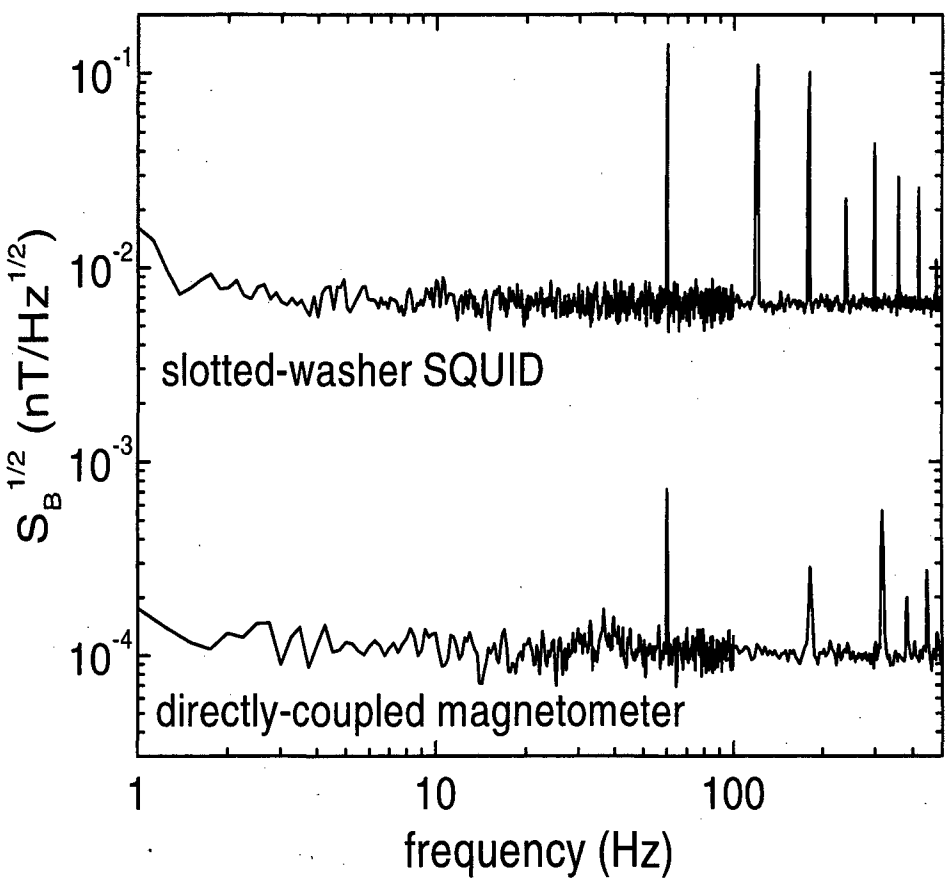

Figure 8.1: Noise spectra of slotted-washer SQUID and directly coupled magnetometer cooled in a zero field in a shielded environment.

fications should be substantially improved.

Noise spectra of directly coupled and slotted-washer magnetometers, measured in a magnetic shield, are presented in Fig. 8.1. Magnetic field sensitivities of the slotted-washer SQUID and the directly coupled magnetometer are 6 $pTHz^{-1/2}$ and 100 $fTHz^{-1/2}$, respectively, in the white noise region. The sensitivity of a slotted-washer SQUID is sufficient for an operation of the device in a reference channel of the multichannel system provided that the intrinsic noise level and balance of the front-end gradiometer are 100 $fTHz^{-1/2}$ and better than 1 part in 60, respectively.

Chapter 9

Gradiometers: principles of operation

9.1 First-order gradiometer

The principle of the gradiometer evolved from a design by Zimmerman [89] for a wire-wound, axial gradiometer coupled to a fractional-turn SQUID machined from niobium; a thin-film version was demonstrated by Matlachov *et al.* [90]. In the first-derivative gradiometer shown schematically in Fig. 9.1 (a), an asymmetric flux transformer is inductively coupled to a directly coupled magnetometer. The flux transformer consists of a pickup loop of area A_p and inductance L_p connected in series with an input loop of area A_i and inductance L_i. The input loop is inductively coupled via a mutual inductance $M=\alpha(L_m L_i)^{1/2}$ to the pickup loop of a directly coupled magnetometer which has area A_m and inductance L_m. The first-order baseline d_1 is given by the separation of the centers of the input and pickup loops.

The condition for the gradiometer to be balanced, i.e. for the magnetometer to produce zero response to the applied uniform field B_0, is found by conserving magnetic flux in the pickup loop of the magnetometer and in the flux transformer, respectively:

$$B_0 A_m - L_m J_m - M J_t = 0, \tag{9.1}$$

$$B_0(A_p + A_i) - J_t(L_p + L_i) - M J_m = 0. \tag{9.2}$$

Here, J_m and J_t are the screening supercurrents in the magnetometer and the flux transformer. To achieve the balance condition, $J_m=0$, the mutual inductance M must satisfy the

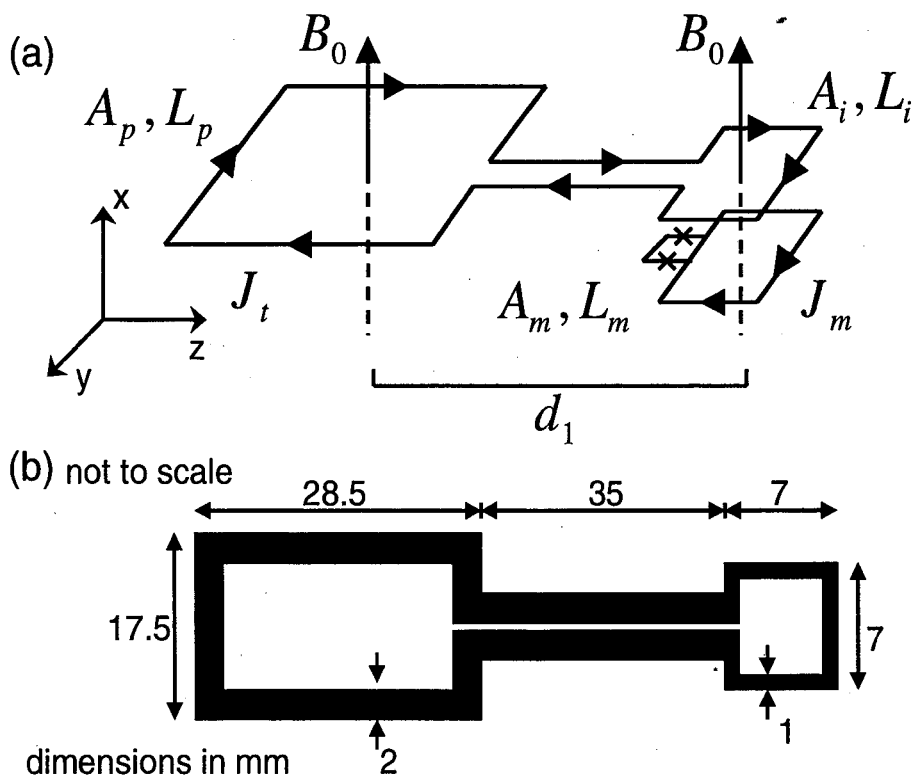

Figure 9.1: Schematic diagrams of first-order gradiometer (a) and flux transformer used in the practical device (b).

condition

$$M_{opt} = [A_m/(A_p + A_i)](L_p + L_i), \tag{9.3}$$

where $M_{opt} = \alpha_{opt}(L_m L_i)^{1/2}$ is the optimal value of M required to reject a uniform fluctuating field. The area and inductance values must be chosen so that the optimal value of the coupling constant is less than unity, $\alpha_{opt} \leq 1$. To determine the gradient response, we assume that a magnetic field δB_x is applied to one of the loops of the flux transformer. This is equivalent to applying a gradient $\partial B_x/\partial z \approx \delta B_x/d_1$ across the baseline d_1 of the flux transformer. The current response of the magnetometer is $\delta J_m = \eta \delta B_x A_m/L_m$, where

$$\eta = \frac{A_p}{A_m} \frac{L_m}{M_{opt} - (L_i + L_p)L_m/M_{opt}} \tag{9.4}$$

represents the reduction of the sensitivity to the applied field compared to that of the bare magnetometer $\delta B_x A_m/L_m$. Here, M_{opt} is the optimal value of the mutual inductance given by Eq. (9.3). In most practical cases M_{opt} is much smaller than the total inductance of the flux transformer $L_i + L_p$, which leads to $\eta = -A_p/(A_p + A_i)$. By making A_p much larger than A_i, one achieves $|\eta| \approx 1$, meaning that a gradiometer responds to a small field applied to one of its loops with the sensitivity of the bare magnetometer. This case is particularly relevant for biomagnetic measurements in which a magnetic signal is detected by one of the loops of the gradiometer.

9.2 Second-order gradiometer

The concept of the first-order gradiometer can be extended to the symmetric second-order design shown schematically in Fig. 9.2 (a). Two pickup loops of areas A_{p1} and A_{p2} and inductances L_{p1} and L_{p2} are connected in series with an input loop of area A_i and inductance L_i. The input loop is inductively coupled via a mutual inductance $M=\alpha(L_m L_i)^{1/2}$ to the pickup loop of a directly coupled magnetometer which has area A_m and inductance L_m.

We assume that a uniform magnetic field B_x with a superimposed gradient $\partial B_x/\partial z$ is applied along the baseline such that the magnetic fields at the positions of two outer loops of the flux transformer are $B_x - l_1 \partial B_x/\partial z$ and $B_x + l_2 \partial B_x/\partial z$, respectively. Here, l_1 and l_2 are the distances from the center of the input loop to the centers of the pickup loops

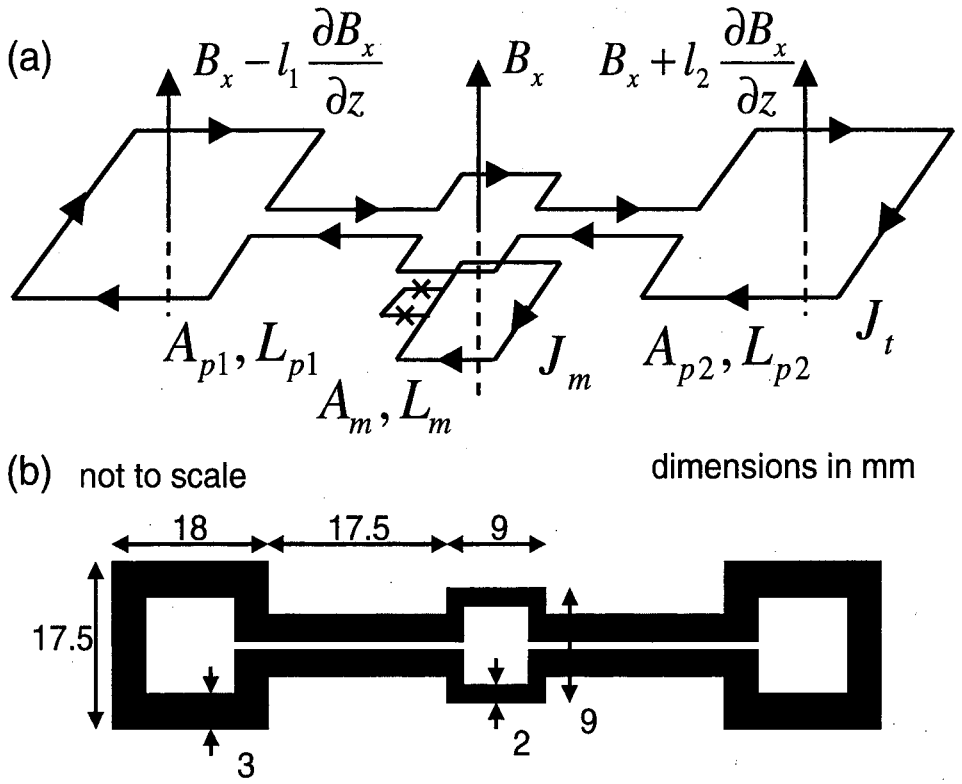

Figure 9.2: Schematic diagrams of symmetric second-order gradiometer (a) and practical transformer coil (b).

1 and 2. Flux conservation conditions in the pickup loop of the magnetometer and in the transformer become

$$B_z A_m - L_m J_m - M J_t = 0, \quad (9.5)$$

$$(B_z - l_1 \partial B_z/\partial x) A_{p1} + (B_z + l_2 \partial B_z/\partial x) A_{p2} + B_z A_i - J_t(L_{p1} + L_{p2} + L_i) - M J_m = 0. \quad (9.6)$$

Here, J_m and J_t are the screening supercurrents in the magnetometer and transformer. The condition for the rejection of the first-order gradient is evident from Eq. (9.6), where the current in the flux transformer J_t is insensitive to $\partial B_x/\partial z$ provided $l_1 A_{p1} = l_2 A_{p2}$. Balance in a uniform field, $J_m = 0$ is achieved by choosing the appropriate value of the mutual inductance,

$$M_{opt} = [A_m/(A_{p1} + A_{p2} + A_i)](L_{p1} + L_{p2} + L_i), \quad (9.7)$$

which is similar to Eq. (9.3) for the first-derivative device. As in the case of Eq. (9.3), $\alpha_{opt} = M_{opt}/(L_m L_i)^{1/2}$ must be chosen to be less than unity, $\alpha_{opt} \leq 1$.

A second-order gradiometer can be configured either as symmetric $l_1 = l_2$ or as an asymmetric $l_1 \neq l_2$ device. For a symmetric flux transformer we set $l_1 = l_2 = l$ and $A_{p1} = A_{p2} = A_p$; the second-order baseline d_2 is given by the separation of the centers of the input and one of the pickup loops, $d_2 = l$. To assess the sensitivity of the symmetric device, consider a magnetic field δB_x applied to one pickup loop of the flux transformer. The current induced in the magnetometer loop is $\delta J_m = \eta \delta B_x A_m / L_m$, where

$$\eta = \frac{A_p}{A_m} \frac{L_m}{M_{opt} - (L_i + 2L_p) L_m / M_{opt}} \quad (9.8)$$

represents the reduction in the sensitivity compared with the value $\delta B_x A_m / L_m$ for the bare magnetometer. In the limits $M_{opt} \ll 2L_p$ and $A_i \ll 2A_p$, we find $\eta \approx 1/2$, indicating that the sensitivity of the symmetric second-order gradiometer is one-half that of the bare magnetometer or the first-order gradiometer.

9.3 Practical considerations for gradiometer fabrication

Several nonidealities in the gradiometer designs were neglected in the discussion above but are important in practical devices. One of them arises from the finite areas and inductances of the striplines used to connect coils in the flux transformer. The effects of the stripline area and inductance are to increase the area and inductance of the pickup loop to

which the stripline is connected. To include the effects of finite areas and inductances of striplines, one can substitute $A'_p = A_p + A_{sp}$ and $L'_p = L_p + L_{sp}$ for the areas and inductances of the pickup loops A_p and L_p in Eqs. (9.1)-(9.8) above. Here, A_{sp} and L_{sp} are the area and inductance of the stripline. In our practical designs discussed below, we choose A_{sp} and L_{sp} to be much smaller than A_p and L_p in order for the striplines not to influence the values of α_{opt} and η. If one is not careful with the choice of A_{sp} and L_{sp}, the modified values of A'_p and L'_p and the distributed nature of the striplines will lead to an imbalance of the device and to a decrease in the effective baseline.

Another nonideal behavior is due to an imperfect placement of the input coil of the flux transformer over the pickup loop of the directly coupled magnetometer. If the magnetometer and transformer substrates are not perfectly parallel to each other, the device becomes sensitive to in-plane components of an applied magnetic field which cannot be rejected by adjusting the value of the mutual inductance. If the vertical separation between the magnetometer and transformer substrates varies by δh over the length w of the magnetometer chip, the gradiometer will be sensitive to an in-plane field with a coefficient proportional to $\delta h/w$. For $\delta h/w \approx 10^{-3}$ and w=1 cm, δh must be of the order of 10 μm. To correct for the residual sensitivity to in-plane fields, we use three orthogonally mounted magnetometers in our multichannel system described below.

In the hardware second-order gradiometer, the in-plane misalignment of the centers of the input coil and the magnetometer by δx results in a residual sensitivity to a first-order gradient which is proportional to $\delta x/d_2$. Here, d_2 is the second-order baseline. We do not use any additional methods to correct for the residual sensitivity to first-order gradients, and rely only on the accuracy with which we can assemble the device. If one wishes to maintain $\delta x/d_2 \approx 10^{-3}$ than the substrates must be aligned to within about 30 μm. This accuracy is achievable in flipchip devices discussed below with the help of alignment marks on the flux transformer.

Chapter 10

Gradiometers: practical realizations

Flux transformers were fabricated at Conductus, Inc. from a 260 nm thick YBCO film coevaporated onto a 100 mm diameter r-plane sapphire wafer buffered with a CeO_2, and patterned by photolithography and etching in a 0.05% aqueous solution of HNO_3. The fabrication procedure for directly coupled magnetometers used in gradiometers was described in chapter 8. Testing of individual devices was done without magnetic shielding while the gradiometer was immersed in liquid nitrogen. A gradiometer was mounted on the lower end of a fiberglass cryogenic probe with its baseline oriented vertically along the z axis. The SQUID, flux modulated at 256 kHz, was operated in a flux-locked loop.

To balance a gradiometer in a uniform field, we placed it in the center of a 1.1 m diameter Helmholtz pair with with the axis of the coils perpendicular to the plane of the device. To achieve a maximum uniformity of the field in the center of the Helmholtz pair we used single-turn circular coils. Numerical modeling of the field distribution in the 1.1 m diameter Helmholtz pair shows that even if the gradiometer was misaligned by as much as 5 mm in any direction, the values of $2l\partial B_x/B_x\partial z$ and $l^2\partial^2 B_x/B_x\partial z^2$ produced by the coils were below 10^{-5} for $l = 6cm$. Uniformity of the field can also be influenced by the imperfect fabrication of twisted pairs of wires connected to the coils and by screening currents induced in nearby metallic objects - effects that are very difficult to model quantitatively. The relatively crude calibration of the Helmholtz pair with the flux gate magnetometer yielded a uniformity better than 100 ppm over a 6 cm distance in the center.

To characterize the balance of the first-order gradiometer with respect to an out-of-plane B_x in the absence of eddy currents, we write the magnetometer response in the form

$$R^{(1)} = C_x^{(0)} B_x + \frac{\partial B_x}{\partial z} d_1, \tag{10.1}$$

where d_1 is a first-order baseline, and $C_x^{(0)}$ is a common mode coefficient that defines the balance of the gradiometer with respect to B_x. Here, the value of $C_x^{(0)}$ is normalized to the response to the first-order gradient. In the case of a second-order device, Eq. (10.1) becomes

$$R^{(2)} = C_x^{(0)} B_x + C_{xz}^{(1)} \frac{\partial B_x}{\partial z} d_1, + \frac{\partial^2 B_x}{\partial z^2} d_2^2 \tag{10.2}$$

where d_2 is a second-order baseline, and $C_{xz}^{(1)}$ is a common mode coefficient that defines the balance of the gradiometer with respect to $\partial B_x / \partial z$. Here, values of $C_x^{(0)}$ and $C_{xz}^{(1)}$ are normalized to the response to the second-order gradient. To test our gradiometers and to determine the common mode coefficients experimentally, we applied an alternating current to the calibrated source of the magnetic field, for example the Helmholtz pair, and measured the output of the flux-locked SQUID using a lock-in detector with a noise bandwidth of 26 mHz.

10.1 Mechanical first-order gradiometer

In order to test the concept of the first-order gradiometer, we fabricated the flux transformer as shown in Fig. 9.1 (b). The baseline, given by the separation of the centers of the input and pickup loops, is approximately d_1=48 mm. We estimate the inductance and the area of the pickup loop to be $A_p \approx$411 mm^2 and $L_p \approx$ 50nH, and of the input loop to be $A_i \approx$36 mm^2 and $L_i \approx$ 9 nH. For the directly coupled magnetometer described in chapter 8, we estimate A_m=20 mm^2 and L_m=4 nH. From Eq. (9.3), these parameters lead to the optimum values of the mutual inductance M_{opt} and coupling constant α_{opt} of 2.4 nH and 0.43, respectively. From Eq. (9.4), we find η=0.95, indicating that the presence of the flux transformer reduces the intrinsic sensitivity of the magnetometer by only 5%. If we account for the finite area and inductance of the stripline, we obtain α_{opt}=0.47 and η =0.96, where we used $A_{sp} \approx$70 mm^2 and $L_{sp} \approx$14 nH for the stripline area and inductance, respectively.

We mounted the magnetometer and the flux transformer face to face, separated by a 2.5 μm thick mylar sheet. Two substrates were planarized with respect to each other using BeCu springs that maintained their elasticity at 77 K. The flux transformer was attached to a fiberglass mount, the position of which we could adjust in z direction from outside the dewar by means of a differential screw. The positioning accuracy of the differential screw was about 0.5 μm allowing us to vary the mutual inductance *in situ* to obtain the balance condition of Eq. (9.3).

The response of the magnetometer to a fixed 100 Hz magnetic field is plotted in Fig. 10.1 as a function of the relative separation between the centers of the input loop of the flux transformer and the pickup loop of the magnetometer. Using the lock-in technique, we observe both the in-phase and quadrature components in the magnetometer signal. As we slide the flux transformer towards the center hole of the magnetometer, the in-phase output progressively decreases and drops sharply to 0.85 pT, which corresponds to a rejection of the applied field of 100 nT, shown as a dashed line in Fig. 10.1 (a), by more than a factor of 10^5. As we continue to move the flux transformer, the in-phase signal changes sign and increases in magnitude. The change of sign is clearly evident from the data plotted on the linear scale in Fig. 10.1 (b). The magnitude of the quadrature component in an unbalanced gradiometer is about 100 times lower than the in-phase signal, and it can be minimized by an additional factor of about 100 by adjusting the position of the flux transformer. However, the maximum suppression of the quadrature signal, also accompanied by the sign change, occurs at a different separation than that corresponding to the in-phase signal. This result suggests that the quadrature signal is caused by higher-order gradients that are partly canceled by choosing a different value of the mutual inductance. At the zero crossing point in Fig. 10.1 (b), the quadrature component varies nonlinearly with the separation, implying that it has higher order gradient components. On the other hand, the in-phase component varies linearly with separation near the optimum balance point, with the slope of 50 pT/μm; thus, the observed cancellation corresponds to an error of about 0.05 μm in the separation. However, we emphasize that such a degree of cancellation is impossible to achieve in a controllable manner, and it is also unstable with time even for a stationary gradiometer. A more typical value that we can obtain routinely lies somewhere between 50 and 100 ppm. The maximum balance level determined for an in-phase component represents the intrinsic common mode balance of the device with respect to the out-of-plane fields, i.e. the coefficient $C_x^{(0)}$ in Eq. (10.1).

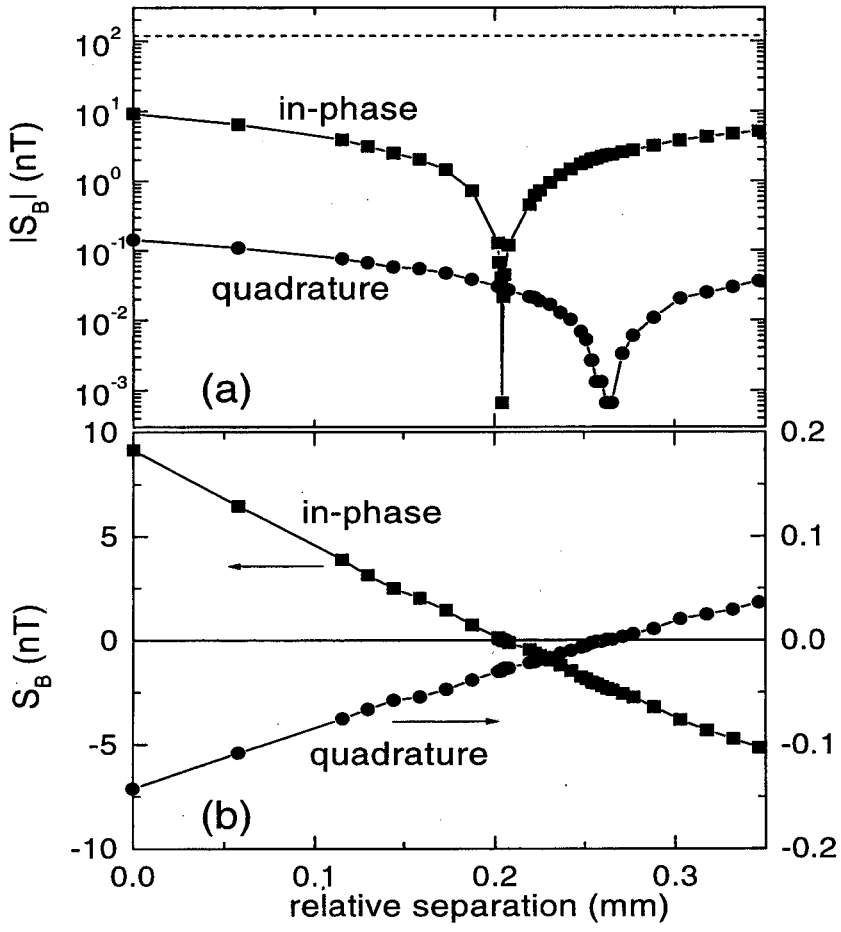

Figure 10.1: Calibration of first-order gradiometer in a uniform field; (a) magnitude of the signal $\|S\|$ and (b) signal S from the magnetometer vs the relative horizontal separation of the centers of the magnetometer pickup loop and the input loop of the flux transformer (arbitrary zero). Dashed line in (a) is the magnitude of a 100 Hz perpendicular magnetic field.

The rejection of the uniform field applied in the plane of the gradiometer is an important criterion needed to characterize the device fully. To evaluate the response in the y direction, we first rotated the unbalanced gradiometer by approximately 90° to locate the precise angle θ_m at which the minimum response to the applied field occurred. We restored the gradiometer to its original position, such that the field is perpendicular to the plane of the device, and balanced the device for a maximum rejection of the in-phase signal. Then, we rotated the device back to θ_m and recorded the magnitude of the in-phase signal. This procedure yielded a rejection of the field in the y direction by a factor of 1400. This value represents the intrinsic common mode balance in the y direction, and is due to an imperfect planarity of magnetometer and flux transformer substrates.

We measured the response of the balanced gradiomter to a gradient field $\partial B_x/\partial z$ produced by a pair of long parallel wires placed vertically below the dewar in the plane of the gradiometer. This arrangement takes advantage of the stray field produced by a return path of the current compared to measurements with a single wire. We passed a 100 Hz current through one wire and back through the other to produce a gradient $\partial B_x/\partial z$ that falls off as $1/z^3$, where z is the distance between the centerline of the two wires and the centerline of the gradiometer. As we progressively change the distance x from 0.09 m to 1.1 m the response of the gradiometer, shown in Fig. 10.2, decreases by three orders of magnitude. The least-squares fit of the data on a log-log plot in Fig. 10.2 yields a slope of -2.976±0.028, which is very close to the expected value of -3. The calculated response of an ideal gradiometer with a slope of -3 is shown as the solid line in Fig. 10.2, which clearly crosses all the data points. This measurement proves that our gradiometer is a first-derivative device with a very low common mode with respect to out-of-plane fields. We note that the limited range over which we can vary z prevents us from making precise estimates of the common mode response from this data. As an illustration of the estimate of the upper limit, we plot the lower portion of the data in Fig. 10.2 along with the calculated response from a gradiometer with the common mode $C_x^{(0)}$=0.01, shown as the dashed line, in the inset of Fig. 10.2. The dashed line lies above the measured data indicating that only common modes of 0.01 or higher would have been distinctly noticeable in these measurements.

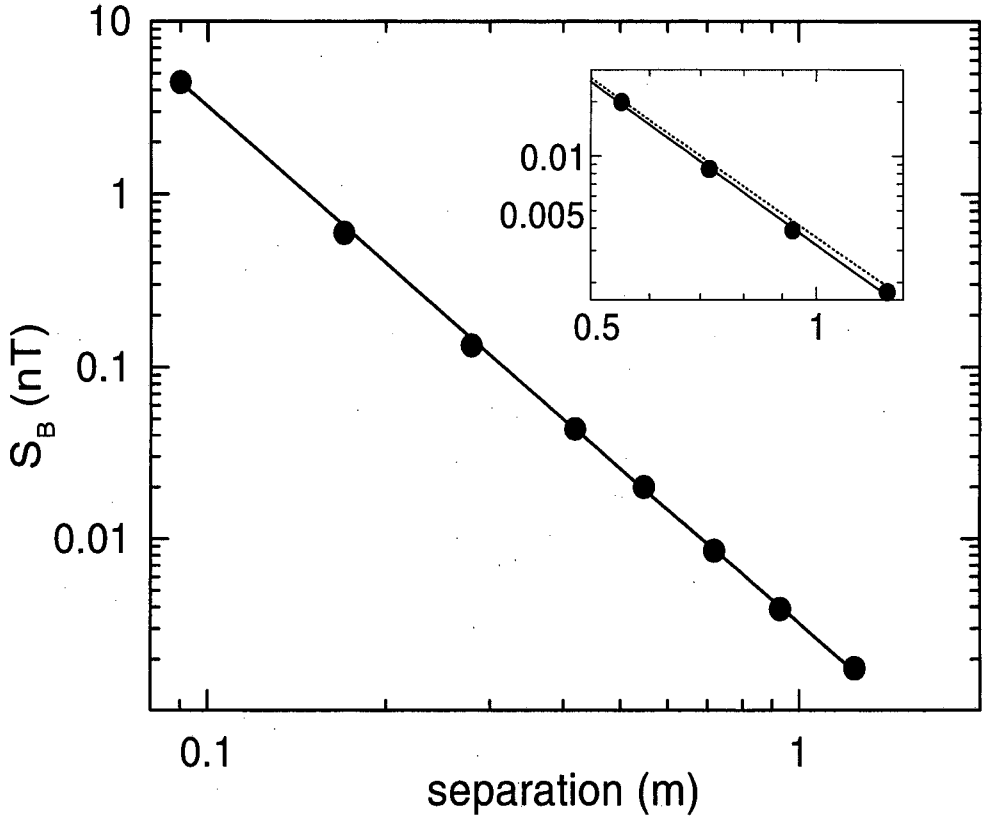

Figure 10.2: Signal from the magnetometer vs separation from two parallel wires (circles). The solid line is the response expected from the ideal first-order gradiometer. The dashed line in inset is the gradiometer response with $C_x^{(0)} = 0.01$.

10.2 Mechanical second-order gradiometer

We have fabricated and tested a symmetric second-order gradiometer as shown schematically in Fig. 9.2. The separation of the centers of the two pickup loops is 62 mm; thus the baseline of the second-order gradiometer is 31 mm. We chose $A_{p1} = A_{p2} \approx$ 218 mm^2, $L_{p1} = L_{p2} \approx$ 31 nH, $A_i \approx$ 49 mm^2, and $L_i \approx$ 9 nH. These parameters lead to estimated values of the mutual inductance M_{opt} ≈2.9 nH and the coupling constant α_{opt} ≈0.49. The sensitivity to a small field applied to one of the outer loops is $\eta \approx 0.46$. If we account for finite areas and inductances of striplines, we obtain $\alpha_{opt} = 0.48$ and $\eta = 0.47$, where we used $A_{sp1} = A_{sp2} \approx 52.5$ mm^2 and $L_{sp1} = L_{sp2}$ ≈7 nH for the areas and inductances of the striplines connected to A_{p1} and A_{p2} , respectively.

We mounted the gradiometer on a probe that allowed us to change the vertical separation between the magnetometer and flux transformer by means of a wedge that we could adjust from outside the dewar. This arrangement enabled us to vary the mutual inductance while maintaining the symmetry required to reject the first-order gradient. The positioning accuracy along the x axis of 0.5 μm was the same as for the first-order gradiometer with horizontal translation along the z axis.

Figure 10.3 (a) shows the magnitude $\|S\|$ of the in-phase and quadrature rms signals versus the relative separation of the magnetometer and flux transformer in response to an applied 100 Hz field from the Helmholtz pair. The magnitude of the field is constant, and is shown in Fig. 10.3 (a) as a dashed line. At the separation corresponding to an optimum value of the mutual inductance given by Eq. (9.7) the in-phase signal is reduced by a factor of 10^5. The quadrature signal exhibits a minimum at a different separation than the in-phase signal, with a reduction of only about 400. We notice the remarkable similarity between the in-phase balancing curves for the first-order gradiometer with horizontal adjustment, in Fig. 10.1 (a) and (b), and for the second-order gradiometer with vertical adjustment, in Fig. 10.3 (a) and (b). This is an indication that different methods of adjusting the mutual inductance lead to the same behavior in rejecting of the applied field; the only effect that matters is achieving the optimal value of the mutual inductance. However, the quadrature signals for the first- and second-order gradiometers behave quite differently. First of all, the minimum in the quadrature signal in Fig. 10.3 (a) occurs on the other side of the minimum in the in-phase signal compared to the data for the first-order gradiometer in Fig. 10.1 (b). The other noticeable feature is that the quadrature curve in Fig. 10.3 (b)

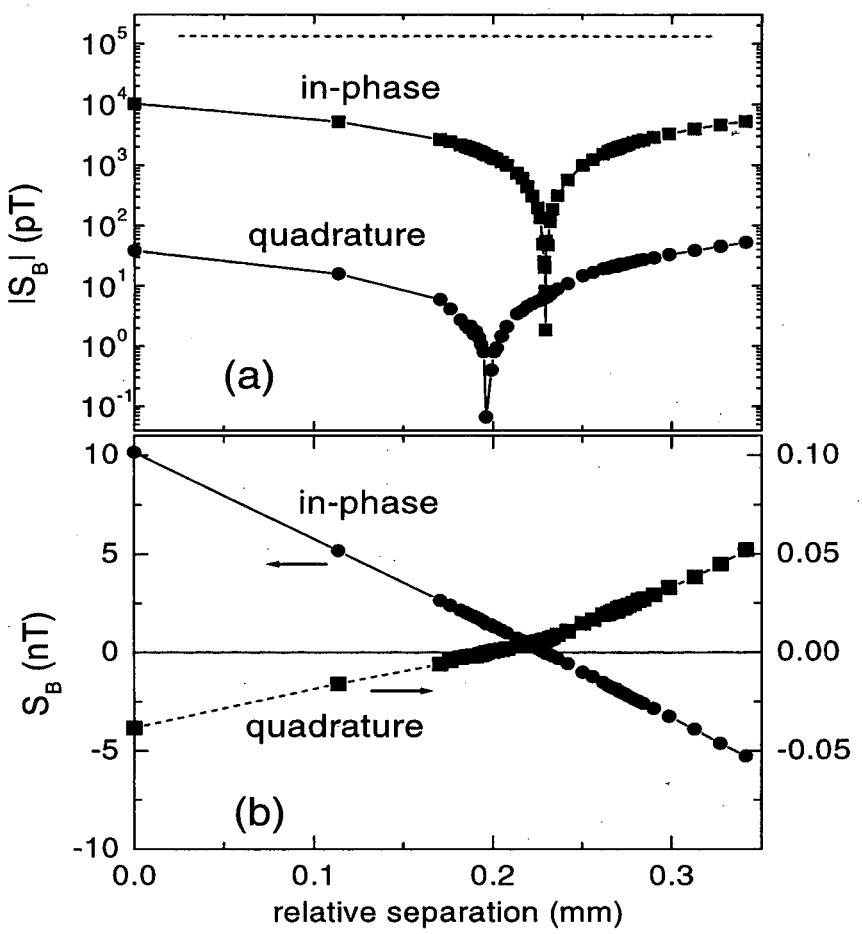

Figure 10.3: Calibration of the second-order gradiometer in a uniform field; (a) magnitude of the signal $\|S\|$ and (b) the signal S from the magnetometer vs the vertical separation between the magnetometer and the flux transformer (arbitrary zero). Dashed line in (a) is the magnitude of a 100 Hz perpendicular magnetic field.

starts at a lower value when the flux transformer is far away from the magnetometer (zero relative separation), and behaves more nonlinearly than the quadrature curve in Fig. 10.1 (b). The observed behavior is consistent with a model in which the quadrature component is caused by eddy currents that couple differently to the gradiometer coils [52] causing a gradient-like signal. The quadrature responses of the first- and second-order gradiometers differ because the second-order device rejects the first-derivative signal by its symmetry, and therefore, the second-derivative signal becomes the highest order gradient which has to be partly canceled by adjusting α. The highest rejection of the in-phase component is close to a factor of 10^5. However, as in the case of the first-order gradiometer, a more typical value for the common mode along the x axis is about 50 ppm.

To determine the accuracy with which our gradiometer responds only to $\partial^2 B_x/\partial z^2$, we performed calibration experiments with two parallel wires as described in section 10.1. A second-order gradient from two parallel wires $\partial^2 B_x/\partial z^2$ is expected to fall off as $1/z^4$, where z is the distance between the centerline of the two wires and the centerline of the gradiometer. Figure 10.4 shows the output of the flux-locked loop vs. z. A least squares fit yields a slope of -3.900 ± 0.028, compared with the expected value of -4. The systematic deviation arises from a common mode response to either B_x or $\partial B_x/\partial z$, or both. Imposing a response to $\partial^2 B_x/\partial z^2$ in Eq. (10.2) that scales as $1/z^4$, we can fit the data in Fig. 10.4 with $C_x^{(0)} = 1.7 \times 10^{-3}$, assuming the deviation is due solely to B_x, or with $C_{xz}^{(1)} = 1.4 \times 10^{-2}$, assuming the deviation is due solely to $\partial B_x/\partial z$. Since the common mode $C_x^{(0)}$ measured in the Helmholtz pair was no more than 5×10^{-5}, we conclude that the deviation from $1/z^4$ arises from a common mode in the first-gradient. This response implies that the flux transformer was misaligned relative to the magnetometer by as much as 0.5 mm. Given our technique of mechanically moving the SQUID while maintaining an alignment with respect to the flux transformer, a misalignment of 0.5 mm is entirely possible. Another drawback of mechanically adjusting the second-order gradiometer is that the magnetometer and transformer substrates were not in direct contact at the position of the optimum balance; thus, the planarity of the magnetometer and transformer substrates was determined by the accuracy of the motion mechanism as well. We measured the response to the in-plane field in a manner similar to the first-order gradiometer and found an in-plane common mode with respect to the uniform field of 1.6×10^{-3}. We note that given the precision of our mechanical assembly such a low value of the common mode is rather fortuitous. In order to achieve low values of in-plane common mode reproducibly, one has

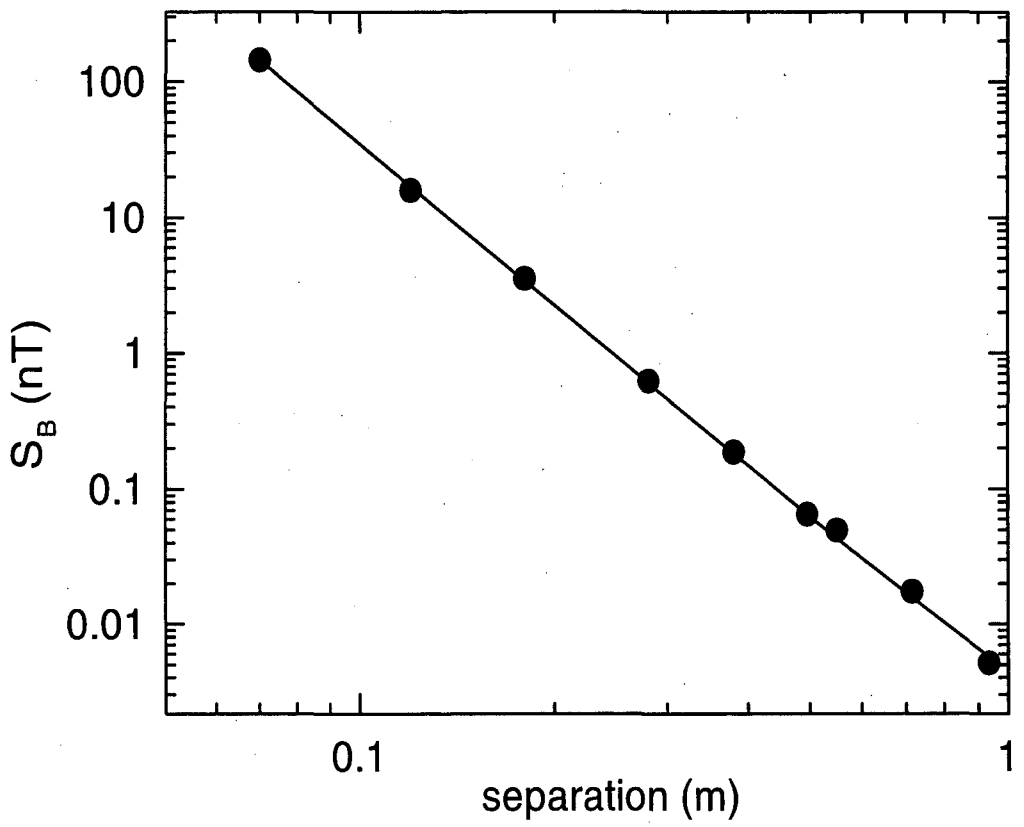

Figure 10.4: Signal S from the magnetometer vs separation from two parallel wires. The line assumes that the deviation from the slope of -4 arises solely from the common mode in the first-gradient with $C_{xz}^{(1)} = 1.4 \times 10^{-2}$.

to make specific arrangements for planarizing the two substrates with respect to each other.

10.3 First-order flipchip gradiometer

Although the techniques of mechanical balancing described above sufficed to demonstrate the gradiometer principles, they are not viable options for practical biomagnetic systems where any mechanical balancing, even if made stable and reproducible, prohibitively increases the system complexity. To demonstrate the applicability of our gradiometers to practical biomagnetic applications, we introduced a first-order device [79] in which a planar flux transformer was permanently bonded to a directly-coupled magnetometer in a flipchip arrangement. A photograph of the assembled flipchip gradiometer is shown in Fig. 10.5.

Prior to fabrication of these flipchip devices, we tested our predictions for the optimum mutual inductance and coupling constant by mechanically balancing the first-order gradiometer in a uniform field. In this experiment the centers of a magnetometer and an input loop were aligned and the vertical separation between the substrates was varied to achieve balance. The results are shown in Fig. 10.6 where the in-phase response of the gradiometer to a 12 Hz, 75.5 nT rms field is reduced to 15 pT rms, resulting in a balance of 1 part in 5000. For the values of inductances and areas chosen, this level of balance occurs when the separation between the two substrates is $716\mu m$. In a separate experiment, we measured the coupling constant α between an input coil of the flux transformer and a directly coupled magnetometer by passing a 12 Hz ac current through the planar YBaCuO coil, which was identical to the input loop of the flux transformer. By varying the vertical separation between the coil and the magnetometer and recording the magnetometer response, we determined the values of α, which are also shown in Fig. 10.6. The value of α at the point of optimal balance is 0.46, which is in good agreement with $\alpha_{opt} \doteq 0.43$ estimated from device parameters.

Having determined the dependence of the balance and α on the separation, we fabricated and tested a permanently assembled flipchip gradiometer. We used the same parameter values for areas and inductances as those of the mechanical first-order gradiometer described in section 10.1. Prior to bonding, both substrates were coated with a 1 μm thick varnish layer to allow for the possibility of disassembling the device by soaking it in acetone. Using alignment marks on both substrates, we positioned the magnetometer relative to the flux transformer to an accuracy of approximately 20 μm with the aid of an

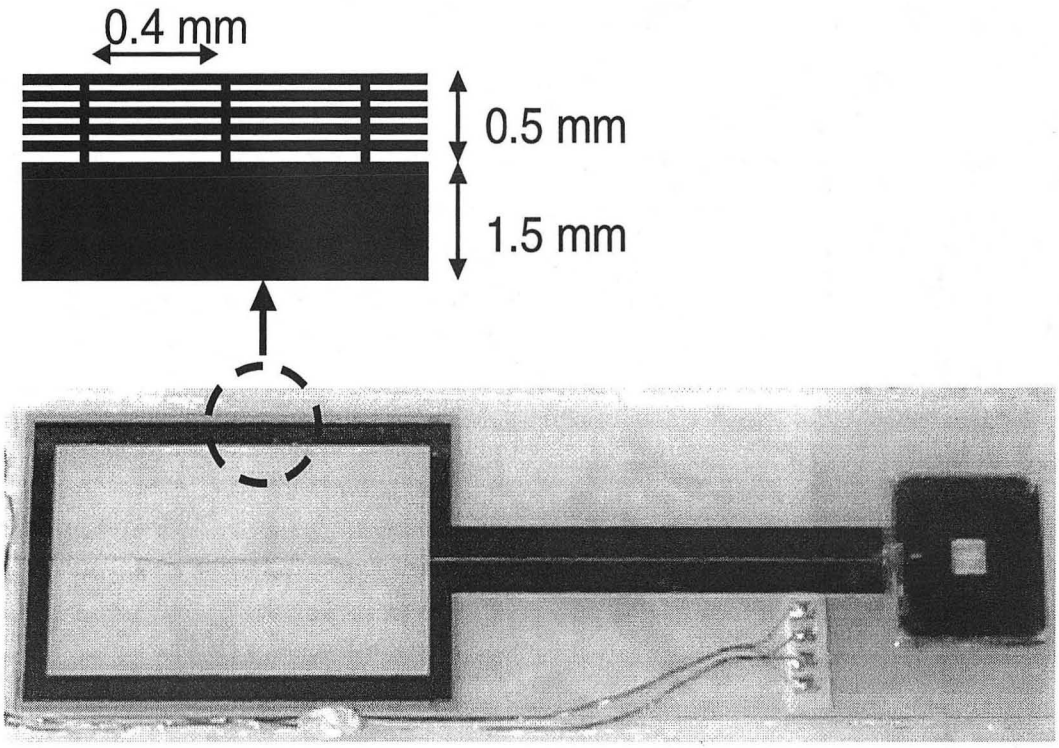

Figure 10.5: Photograph of first-order flipchip gradiometer showing details of the trimming grid.

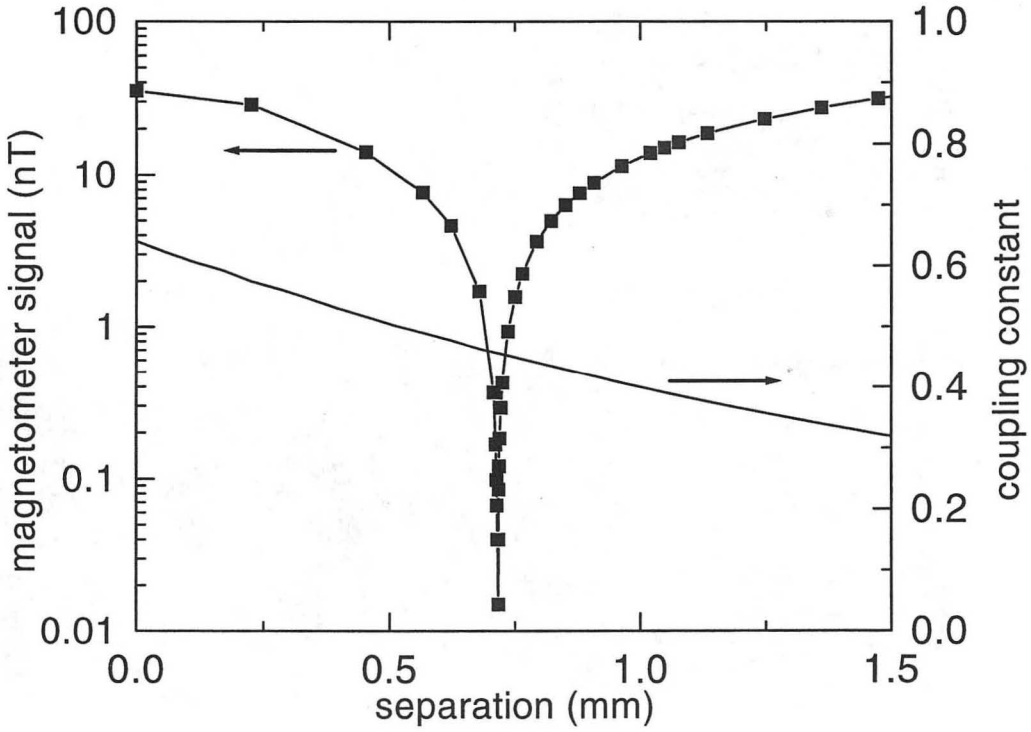

Figure 10.6: Response of the first-order gradiometer to uniform field, and coupling constant α as a function of the separation between the magnetometer and the flux transformer.

optical microscope. The two substrates were bonded together with the rear side of the magnetometer against the film of the flux transformer, using epoxy approximately 10 μm thick. The separation between the two YBaCuO films is 500 μm, which is mostly determined by the thickness of the magnetometer substrate. According to the data in Fig. 10.1 for 500 μm separation, the mutual inductance M is higher than the optimal value M_{opt} given by Eq. (9.3) for the chosen device parameters. In order for us to be able to increase the value of M_{opt} to match the value of M, which was fixed by bonding, we patterned a trimming grid around the edge of the pickup loop as shown in Fig. 10.5. The effect of trimming is to decrease the linewidth of the pickup loop, which results predominately in an increase in the value of the pickup loop inductance L_p leading to an increase in M_{opt} according to Eq. (9.3).

We balanced the gradiometer by applying a 12 Hz magnetic field perpendicular to the plane of the device. A 1.14 m diameter Helmholtz pair was used as a source of the field, which was uniform to better than 100 ppm over the 5 cm baseline. After determining the degree of imbalance, we brought the gradiometer back to room temperature and etched away one line along the left and right edges of the pickup loop. Then we cooled the device back to 77 K and recorded new level of balance. Knowing the correspondence between the improvement in balance and the length of the line trimmed away, we repeated the trimming procedure iteratively, typically two or three times, to achieve a balance with respect to out-of-plane fields of 1 part in a few hundred. We determined the in-plane balance in the y direction by turning the gradiometer through 90° and in the z direction by means of a second Helmoltz pair. The observed values of the in-plane balance were better than one part in a hundred, and we made no further attempts to improve them in hardware.

The reduction in the ambient noise achieved with an intrinsic balance of better than one part in a hundred in any direction is shown in Fig. 10.7. The upper (gray) trace shows the magnetic field noise in our laboratory measured by a slotted-washer SQUID magnetometer: the 60 Hz spike is approximately 10 nT rms, and the noise at 2 Hz is about 50 pTHz$^{-1/2}$. The lower (black) trace is the noise measured by an unshielded flipchip gradiometer, and shows that the 60 Hz spike and the noise at 2 Hz have been reduced by two orders of magnitude. Above 60 Hz, the background noise in the gradiometer is close to that measured in a superconducting shield for the same directly coupled magnetometer, as shown in Fig. 10.7.

A gradiometer becomes sensitive to eddy currents if a conducting object is located

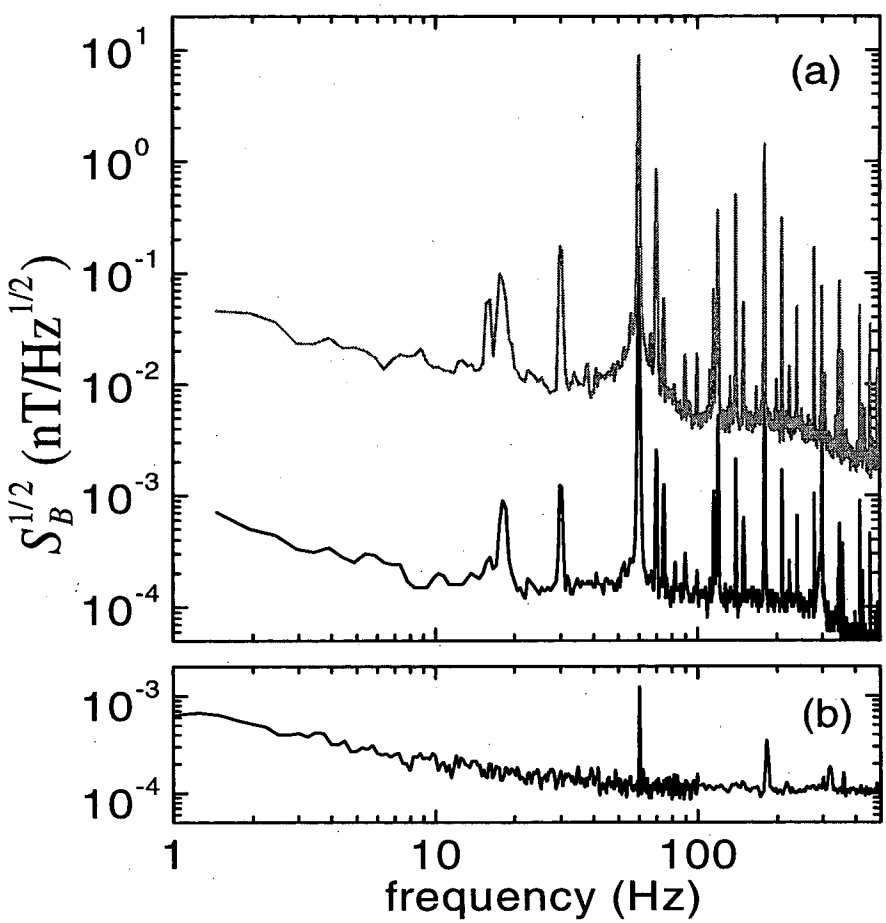

Figure 10.7: Noise spectra of (a) unshielded magnetometer (gray) and gradiometer (black), and (b) shielded directly coupled magnetometer used in gradiometer.

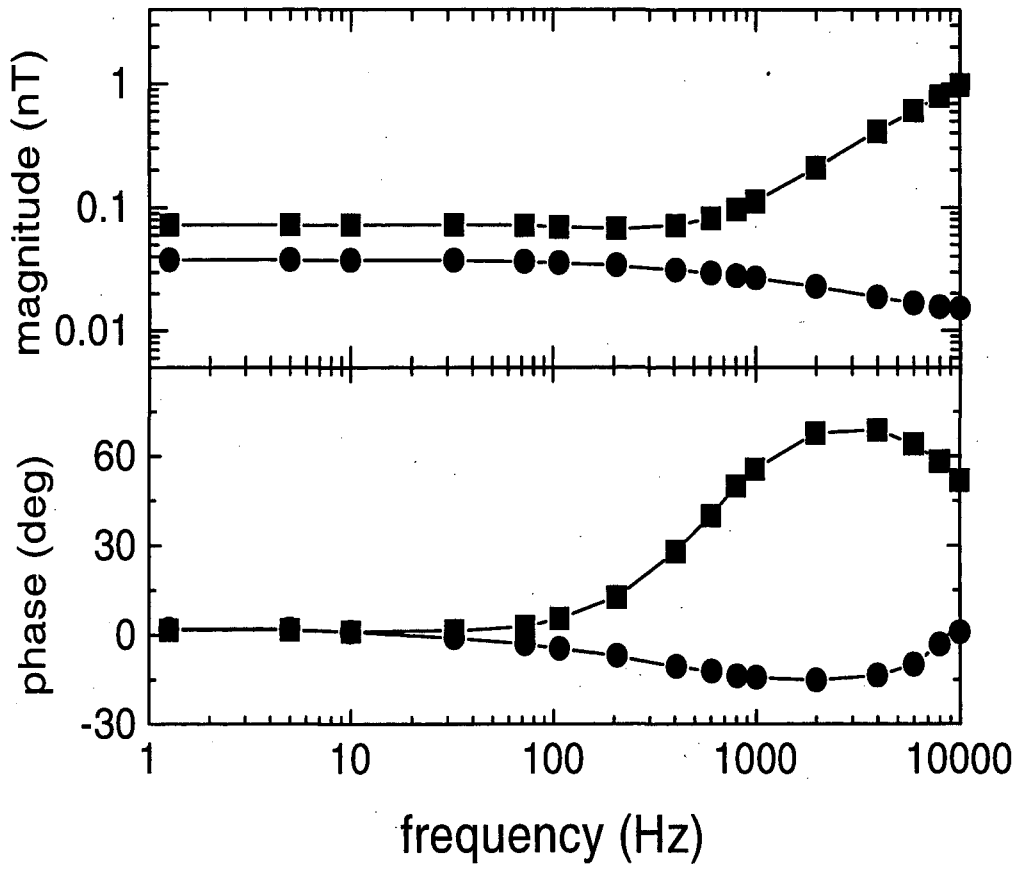

Figure 10.8: Magnitude (a) and phase (b) of the frequency response of the flip-chip gradiometer to a uniform field measured in a styrofoam flask (circles) and in a biomagnetic dewar (squares).

in the vicinity of the gradiometer in such a way that an induced screening current couples different amount of magnetic flux to the gradiometer loops. These effects result in an imbalance of the gradiometer and produce a quadrature component in the response to an applied field [52]. When gradiometers are operated in a multichannel system, phase shifts produced by the quadrature response limit the degree to which one can balance gradiometers electronically using reference magnetometers. We minimized the eddy current responses in our system by moving all conducting objects away from the gradiometer. Unfortunately, our biomagnetic dewar manufactured by BTi Inc. also contained metallic parts that served as a source of eddy currents. The effects of eddy currents are clearly evident in the frequency response of the gradiometer to a uniform field presented in Fig. 10.8, where the squares correspond to data taken in the BTi dewar. Eddy currents produce an increase in the magnitude of the signal at frequencies above 1000 Hz and a phase change above 100 Hz of as much as 70°. For comparison, the frequency response measured in a styrofoam flask is shown as circles in Fig. 10.8 where the magnitude and phase variations at high frequencies are considerably less pronounced. From the frequency dependence measured in the BTi dewar, Fig. 10.8, we estimate phase shifts of 1° and 5° at 10 Hz and 100 Hz, respectively. If the suppression of the uniform field is 1 part in 1000, as shown in Fig. 10.8 (a), and further improvements in balance are achieved electronically, phase shifts at 10 Hz and 100 Hz limit the minimum achievable common mode in the magnetic field to 18 ppm, and 87 ppm, respectively.

Finally, we consider whether an intrinsic common mode of $C^{(0)} \approx 0.1\%$, for all three directions of the magnetic field, and $C^{(1)}_{xz} \approx 0.1\%$, for the second-derivative device, could be realized in the manufacturing process without trimming. The data in Fig. 10.1 and in Fig. 10.3 imply that a balance of 1 part in a 1000 with respect to out-of-plane fields requires a positioning accuracy in all three directions of about 5 μm. The in-plane common mode of 0.1% requires that the separation between substrates be controlled to within 10 μm to insure the two substrates are parallel to each other. In a hardware second-derivative device, a first-order gradient balance of 0.1% requires that a flux transformer be placed over a magnetometer with an accuracy of 30 μm. Therefore, one achieves $C^{(0)} \approx 0.1\%$ and $C^{(1)}_{xz} \approx 0.1\%$ if a bonding accuracy can be reproducibly controlled within 5 μm in all three directions. This accuracy is achievable with commercial flipchip bonders [91], where specifications for the alignment and separation accuracy are typically 1 μm.

Chapter 11

Multichannel system for MagnetoCardioGraphy

11.1 System description

We built and tested a multichannel system in which two first-order gradiometers were supplemented with three orthogonally mounted reference magnetometers. A schematic diagram of the system and a photograph of the cryogenic part of the probe are shown in Fig. 11.1 (a) and (b), respectively. The gradiometers are mounted vertically one above the other. We could vary the distance between the two gradiometers thereby changing the value of the second-order baseline d_2. We used $d_2 = 7.5$ cm in all of the experiments discussed below, although Fig. 11.1 (b) shows $d_2 = 5$ cm. The center of the input loop of the lower gradiometer, which detected the MCG signals, is located approximately 15 mm from the outside of our biomagnetic dewar. The distance from the center of the baseline of the lower gradiometer to the z-axis reference magnetometer is $2d_2 + d_{ref} = 36.5$ cm.

All parts of the probe were machined out of fiberglass in order to eliminate metallic components as much as possible. We used thin wall CuNi tubes for shielding the wires connecting the SQUIDs to flux-locked electronics. Measurements were carried out in a biomagnetic dewar manufactured by BTi, Inc.. The dewar was supported by a wooden structure which supported a circular 1.14 m diameter and a square 1.13 m Helmholtz pair used to calibrate the system. The system was located in the basement of our building where the levels of rf interference are low, allowing us to avoid using an rf shield around the system.

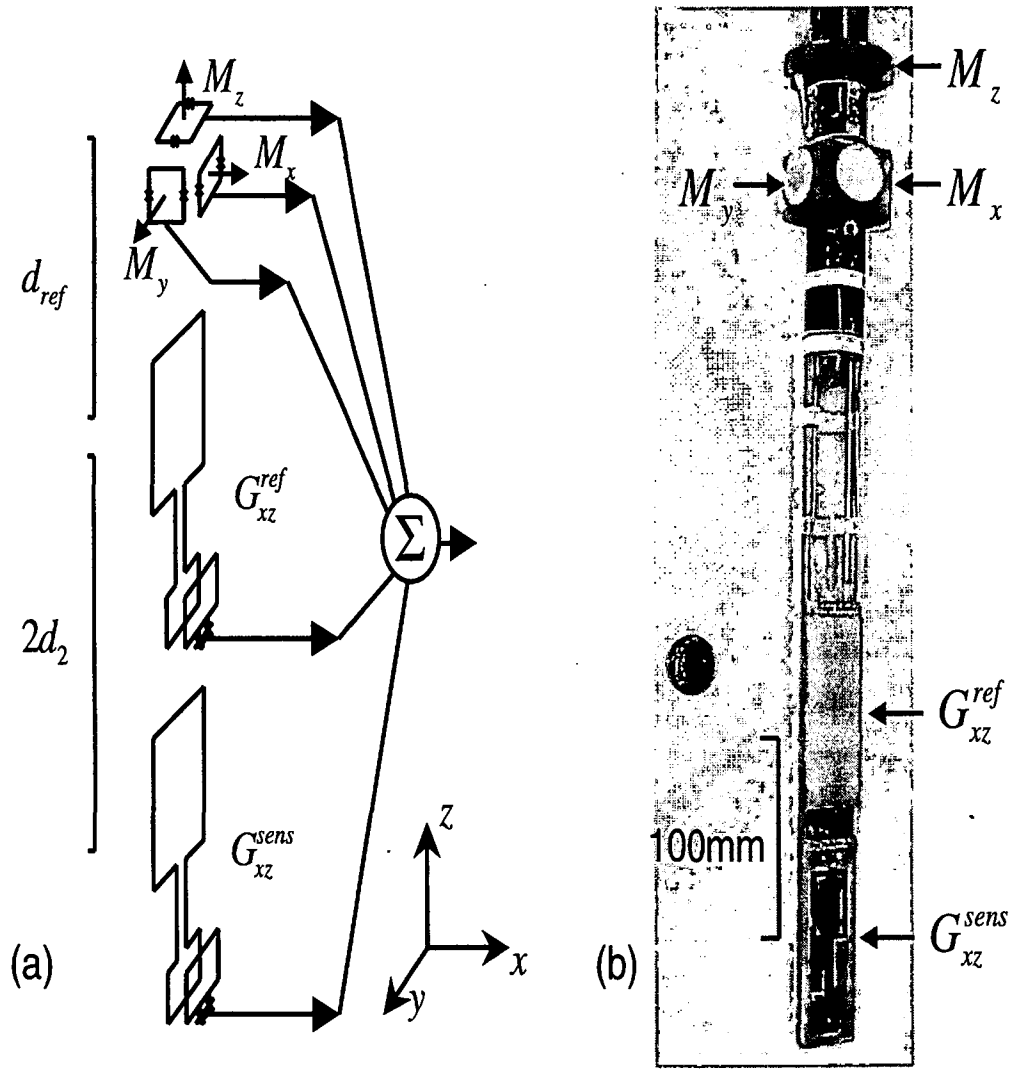

Figure 11.1: Schematic diagram (a) and a photograph (b) of the five channel system.

Both gradiometers and the three magnetometers were encapsulated in hermetically sealed capsules containing heaters made from manganin wire. We could raise the temperature of each device above T_c and slowly cool it to 77 K in the static magnetic field of the Earth. The purpose of this thermocycling procedure is to eliminate flux vortices trapped in and around SQUID washers and Josephson junctions.

The five-channel probe was immersed in liquid nitrogen. The SQUIDs were operated using flux-locked electronics manufactured by Conductus, Inc. with a 256 kHz flux modulation and a bias reversal at 2 kHz. The real time control of the SQUID electronics as well as the data acquisition and analysis were done in software using an IBM PC compatible computer. The data from the five SQUID channels were acquired using a 16 bit, 20 ksamples/s analog-to-digital converter with a sampling frequency of 4 ksamples/s per channel. To prevent aliasing we used a single pole anti-aliasing filter in each channel with a corner frequency $f_{-3dB} = 300$ Hz. To minimize phase shifts in the process of data acquisition we adjusted f_{-3dB} to 300 Hz individually in each channel. However, residual phase shifts and discretization errors associated with the digital gain control limited the accuracy of balancing in software to 1 part in 250.

The noise of the slotted-washer SQUIDs used in the reference channels must not dominate the system noise when the signals from the reference magnetometers are subtracted from the gradiometer signals. Knowing the intrinsic noise and the field common mode of the hardware gradiometers we determined the minimum sensitivity required for the reference magnetometer. If a gradiometer is balanced to 1 part in 100 in hardware, then to completely cancel the noise signal, which is present in both the gradiometer and reference channels, one subtracts the signal of the reference magnetometer attenuated by the same factor of 100 from the gradiometer signal. During the subtraction process, uncorrelated noise power from the reference magnetometer is scaled down by the square of the attenuation factor, 10^4 in this example, and added to the noise power of the gradiometer. Therefore, the intrinsic noise of the reference magnetomer must be not more than 100 times higher than the gradiometer noise to avoid dominating the noise. The sensitivity of our directly coupled magnetometers in the white noise region is in the range of 100 fTHz$^{-1/2}$; thus, the intrinsic noise of the reference magnetometers must be lower than 10 pTHz$^{-1/2}$. The sensitivities of slotted-washer SQUIDs, which are typically 5-6 pTHz$^{-1/2}$ in the white noise region as shown in Fig. 8.1, satisfied our requirements for use in the reference channels.

11.2 System calibration and performance

To assess the performance of a gradiometer system of the order n, one defines a set of common mode and eddy current vectors [52], which characterize the residual sensitivity of the device to a uniform field and gradients of order lower than n. In order to fully describe the common mode and eddy current response of the first-derivative system, we extend Eq. (10.1) to the three dimensional case as follows:

$$R^{(1)} = \mathbf{C}^{(0)}\mathbf{B} + \mathbf{E}\frac{d\mathbf{B}}{dt} + \frac{\partial B_x}{\partial z}d_1, \tag{11.1}$$

where d_1 is the baseline, $\partial B_x/\partial z$ is the first-order gradient applied along the baseline, and $\mathbf{C}^{(0)}$ and $\mathbf{E}$ are the field common mode and eddy currents vectors, respectively.

The three components of $\mathbf{C}^{(0)}$, $C_x^{(0)}$, $C_y^{(0)}$ and $C_z^{(0)}$ are the inverses of the values of the balance measured during calibration in a uniform field applied along the x, y and z axes, respectively. For two gradiometers incorporated in our multichannel system, we found $C_x^{(0)} = 3.1 \times 10^{-3}$, $C_y^{(0)} = 3.1 \times 10^{-3}$ and $C_z^{(0)} = 5 \times 10^{-3}$ for one gradiometer and $C_x^{(0)} = 1.3 \times 10^{-3}$, $C_y^{(0)} = 3.8 \times 10^{-3}$ and $C_z^{(0)} = 6.6 \times 10^{-3}$ for the other.

One can improve the common mode response by subtracting the outputs of the orthogonal reference magnetometers appropriately weighted by the components of the common mode vector from the gradiometer signal. For the improved response of the gradiometer balanced with references $R_{bal}^{(1)}$, we can write

$$R_{bal}^{(1)} = \mathbf{C}^{(0)}\mathbf{B} - \mathbf{cb} + \mathbf{E}\frac{d\mathbf{B}}{dt}, + \frac{\partial B_x}{\partial z}d_1 \tag{11.2}$$

where $\mathbf{b}$ is the magnetic field vector measured by the three orthogonally mounted magnetometers and $\mathbf{c}$ is the vector of the balancing coefficients c_x, c_y and c_z. In an ideal case $c_x = C_x$, $c_y = C_y$ and $c_z = C_z$ and the common mode response due to magnetic field is completely eliminated by balancing the system with reference magnetometers.

However, the eddy current response is proportional to $d\mathbf{B}/dt$, and cannot be eliminated using references because it is phase shifted by 90° relative to the applied signal. Phase shifts in the flux-locked electronics or in the data acquisition channels also appear as eddy current terms thereby contributing to the residual imbalance. The degree of the residual imbalance in a balanced gradiometer can be characterized via the balanced common mode vector $\mathbf{C}_{bal}^{(0)}$ as follows:

$$R_{bal}^{(1)} = \mathbf{C}_{bal}^{(0)}\mathbf{B} + \frac{\partial B_x}{\partial z}d_1. \tag{11.3}$$

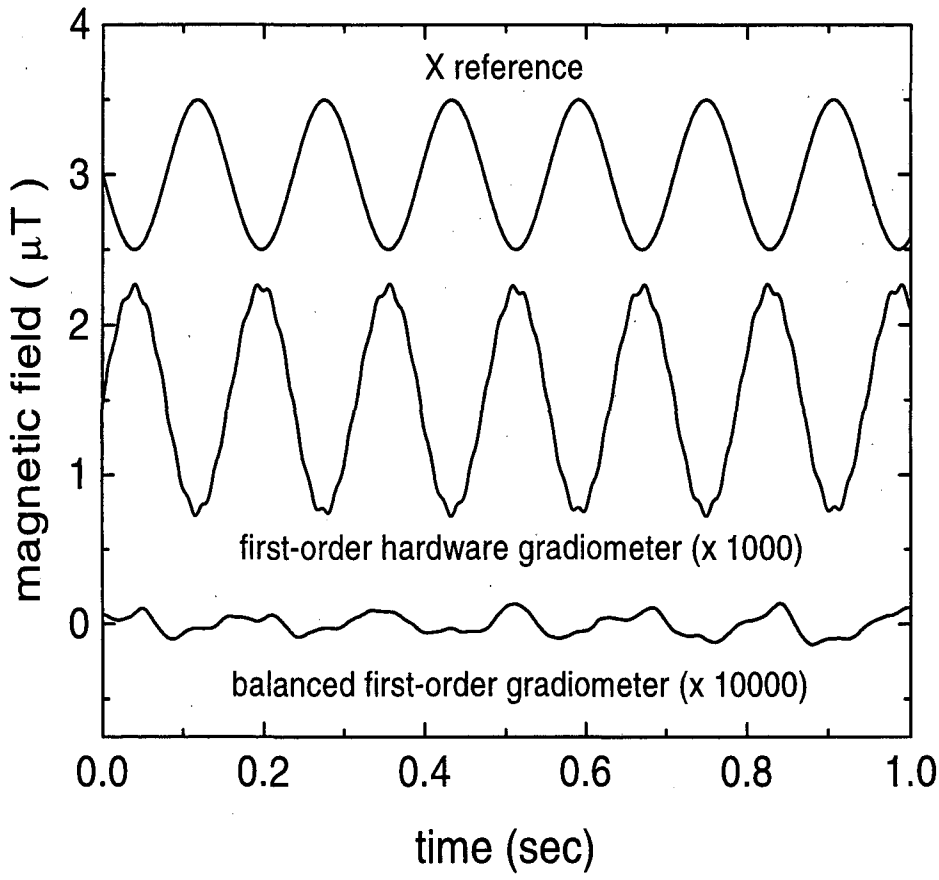

Figure 11.2: Attenuation of 6 Hz signal in the x direction (upper trace) by hardware gradiometer without (middle trace) and with (lower trace) subtraction of reference magnetometer.

To assess the degree to which we can improve the balanced common mode $\mathbf{C}_{bal}^{(0)}$, we applied a 6 Hz, 1 μT peak-to-peak signal perpendicularly to the plane of the gradiometer as shown in Fig. 11.2 where we plot the signal of the x-axis reference magnetometer. This signal is reduced in a hardware gradiometer by a factor of about 700. By subtracting the signals of the x-axis reference and hardware gradiometer, the balanced output has been reduced to a peak-to-peak value of 20 pT, corresponding to an attenuation of the applied magnetic field to 20 ppm. This degree of cancellation is consistent with measurements of the phase shifts in the gradiometer shown in Fig. 10.8, where we estimated the minimum achievable common mode to be 18 ppm at 10 Hz.

A suppression of an applied field to 100 ppm or better using references results in a suppression of the ambient noise. Figure 11.3 demonstrates the cancellation of the low frequency interference produced by the motion of the elevator in our building. In Fig. 11.3 one observes a clear correlation between signals in the gradiometer and in the z-axis reference magnetometer; the highest common mode in this gradiometer was measured along the z-axis, $C_z^{(0)} = 6.6 \times 10^{-3}$. When the reference output was subtracted from the gradiometer output, the interfering signal was suppressed down to the noise level of the gradiometer, corresponding to an attenuation of better than 100 ppm. We emphasize that this method of noise suppression applies only to correlated signals simultaneously present in the gradiometer and reference channels. An uncorrelated noise, such as a random telegraph signal observed only in the gradiometer channel, in Fig. 11.3, cannot be eliminated by balancing with references.

The balancing coefficients c_x, c_y and c_z can be chosen adaptively to fulfill a certain criterion for system performance. For example, adaptive balancing is used frequently in real time MCG measurements where the coefficients are chosen to maximize the signal to noise ratio of the cardiac signal. Another example involves the adaptive choice for the coefficients if one is trying to cancel a correlated interfering signal produced by a known source. This approach is typically used to balance the system for a maximum suppression of the 60 Hz peak. To test the adaptive algorithm in our system, we applied a uniform field of 1 μT peak-to-peak amplitude along the x axis and varied the frequency from 1 to 50 Hz. Figure 11.4 shows the results of the experiment where the hardware gradiometer signal is suppressed by a factor of about 1200 compared to the signal from the x-axis reference. The applied signal is observed in all reference channels due to the imperfect orthogonality of the

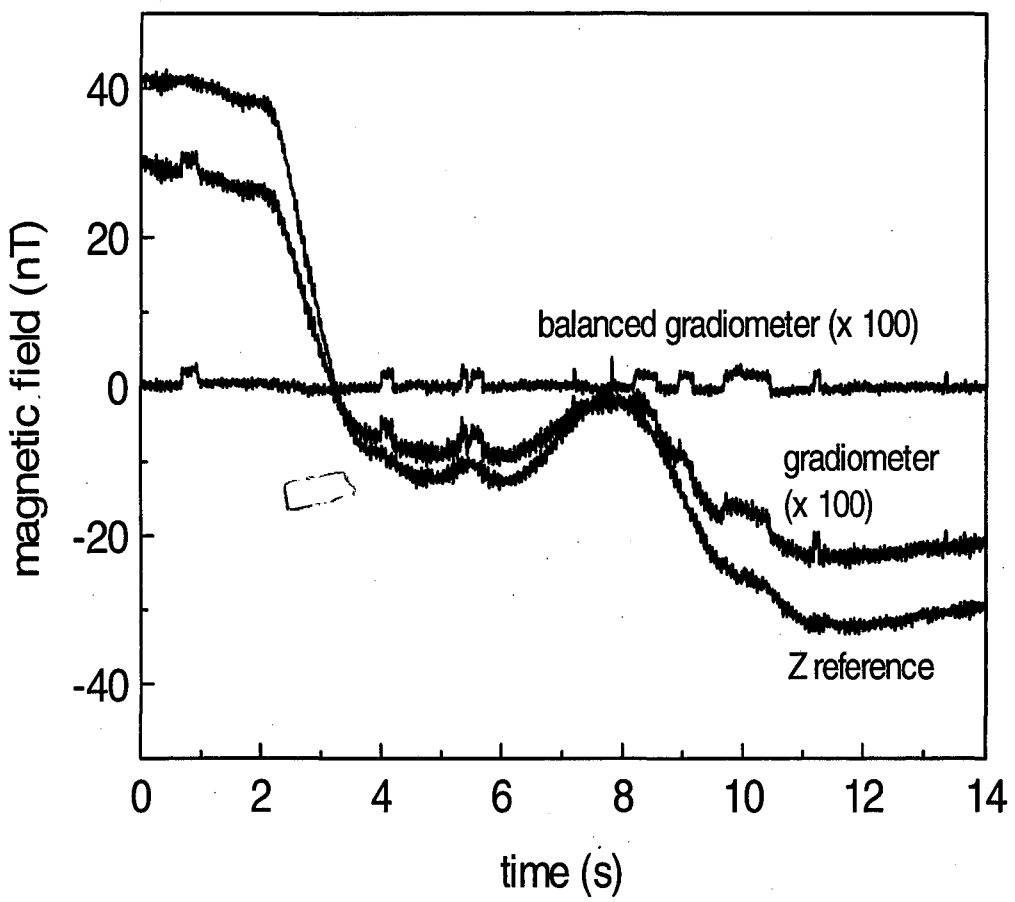

Figure 11.3: Cancellation of low frequency signal produced by the motion of the elevator. Uncorrelated random telegraph signal in the gradiometer channel cannot be eliminated using references.

reference magnetometers. To form a balanced gradiometer, the balancing coefficients were chosen using an adaptive algorithm for the maximum cancellation of an applied signal. The data in Fig. 11.4 for the balanced gradiometer show a complete cancellation of the sweep signal down to the noise level of the magnetometer. This degree of cancellation corresponds to a balance of better than 50 ppm at any frequency between 1 and 50 Hz, which is also consistent with measurements of the phase shifts in Fig. 10.8.

Ambient noise signals contain components proportional to the first- and higher-order gradients. These components become dominant when a gradiometer is highly balanced with respect to uniform fields using reference magnetometers. To reject gradient signals, one has to resort to the formation of higher-order gradiometers. In our system, we formed a second-order gradiometer by subtracting the outputs of two first-order gradiometers in software. To demonstrate the operation of the second-derivative device, we performed calibration measurements with the two parallel wires as described in the section 10.1 for the mechanical first-order gradiometer. The results of the calibration procedure for two first-order gradiometers are shown in Fig. 11.5 (a). The signal from the lower gradiometer decays with a slope of -3.007 ± 0.005. The observed distance dependence is in good agreement with the expected response of the gradiometer with a common mode signal of -3×10^{-3}, which was obtained during the calibration in a uniform field. Similarly, the upper gradiometer signal has a slope of -3.019 ± 0.009, which is also in good agreement with the expected common mode signal of -1.6×10^{-3}. The expected dependences for the upper and lower gradiometers with $C_x^{(0)} \approx -1.6 \times 10^{-3}$ and $C_x^{(0)} \approx -3 \times 10^{-3}$, respectively, are plotted as solid lines in Fig. 11.5 (a).

For the second-derivative device formed in software, we obtained an exponent of -4.348 ± 0.041. We expect the exponent value of -4.256 ± 0.044 for the ideal second-order gradiometer formed by subtraction of two first-order gradiometers with baselines of 4.8 cm separated by 15 cm. The common mode signal of the second-order gradiometer is the difference of the common mode signals of the two first-derivative devices, and is equal to $C_z^{(0)} \approx -1.4 \times 10^{-3}$. Knowing the value of $C_x^{(0)}$, we fit the data in Fig. 11.5 with $C_x^{(0)} \approx -1.4 \times 10^{-3}$ and a common mode coefficient in the first-order gradient of about $C_{xz}^{(1)} \approx 1.13 \times 10^{-2}$, as shown by the solid line in Fig. 11.5 (b). The limited range over which we were able to arrange the wires relative to the gradiometer prevents us from making more precise estimate for $C_{xz}^{(1)}$. However, we emphasize that this calibration procedure is important in establishing that our multichannel gradiometer is indeed a second-order system

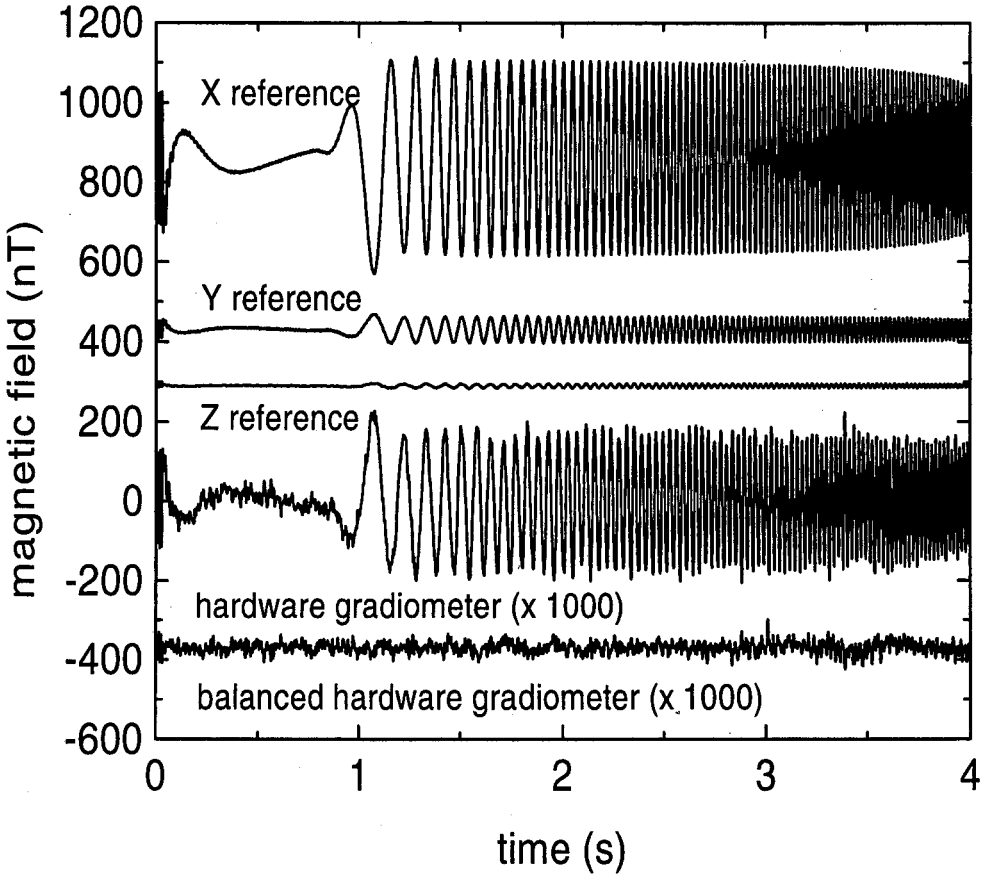

Figure 11.4: Cancellation of the uniform field signal using an adaptive algorithm. Frequency of the applied signal is swept from 1 to 50 Hz.

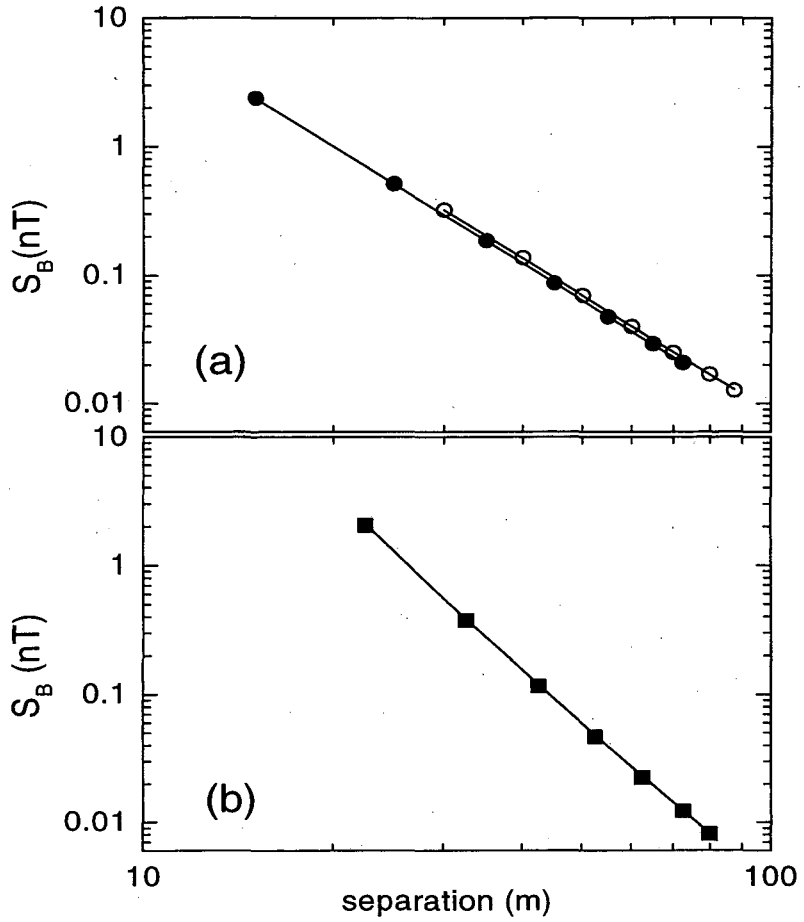

Figure 11.5: Calibration of the software second-order gradiometer with two parallel wires. Solid and open circles in (a) are signals of lower and upper first-order gradiometers, respectively. The lines in (a) demonstrate effects of $C_x^{(0)} \approx -3 \times 10^{-3}$ and $C_x^{(0)} \approx -1.6 \times 10^{-3}$ in the simulated response of first-order gradiometers. Squares in (b) correspond to the second-order gradiometer formed in software. The line in (b) assumes $C_x^{(0)} \approx -1.4 \times 10^{-3}$ and $C_{xz}^{(1)} \approx 1.13 \times 10^{-2}$ for the second derivative device.

with an upper limit on the first-order common mode coefficient $C_{xz}^{(1)} \approx 1.13 \times 10^{-2}$.

Noise spectra for the balanced first- and second-order gradiometers are shown in Fig. 11.6 as gray and black traces, respectively. Common mode corrections with references were formed in software in both cases. We notice that all peaks in the noise spectrum of the second-order gradiometer are reduced compared to those of the first-order device, indicating that a first-order gradient is present in all correlated noise signals. The magnitude of the first-order gradients in the ambient noise, which are suppressed by the action of the second-order gradiometer, depends on the noise environment at the location of the system. For example, the magnitude of the 60 Hz spike is reduced by a factor of about 5 in Fig. 11.6. We compare the heights of the 60 and 180 Hz spikes in the noise spectra of the x-axis reference (gray trace in Fig. 10.7) to those of the balanced second-order gradiometer (black trace in Fig. 11.6). We observe that the power line interference at 60 and 180 Hz is suppressed by factors of 500 and 200, respectively. These results can be contrasted with the recent data of [76], where the second-order axial gradiometer was adaptively balanced for a maximum suppression of the 50 Hz power line fundamental. In [76], first and third harmonics of 50 Hz were suppressed by factors of 2000 and 22, respectively. Notice that the additional suppression of the fundamental by a factor of 4 results in an increased response of the third harmonic by a factor of about 10. The most important drawback of adaptive balancing with respect to suppressing power line signals is the temporal instability of the external noise. As demonstrated in [52], the environmental noise is constantly changing, and, therefore adaptively chosen coefficients must be readjusted once every few minutes to account for changes in the environment. The approach widely adopted in commercial LTS systems is to balance the system for a minimum common mode response using coefficients obtained by calibrating with known sources. In a system with a small number of channels, such as our own system, one can use adaptive control of the coefficients during data acquisition in software to achieve a maximum signal-to-noise ratio of the cardiac signal. Additionally, we use filtering techniques in the data processing software to suppress noise at the power line frequency and its harmonics.

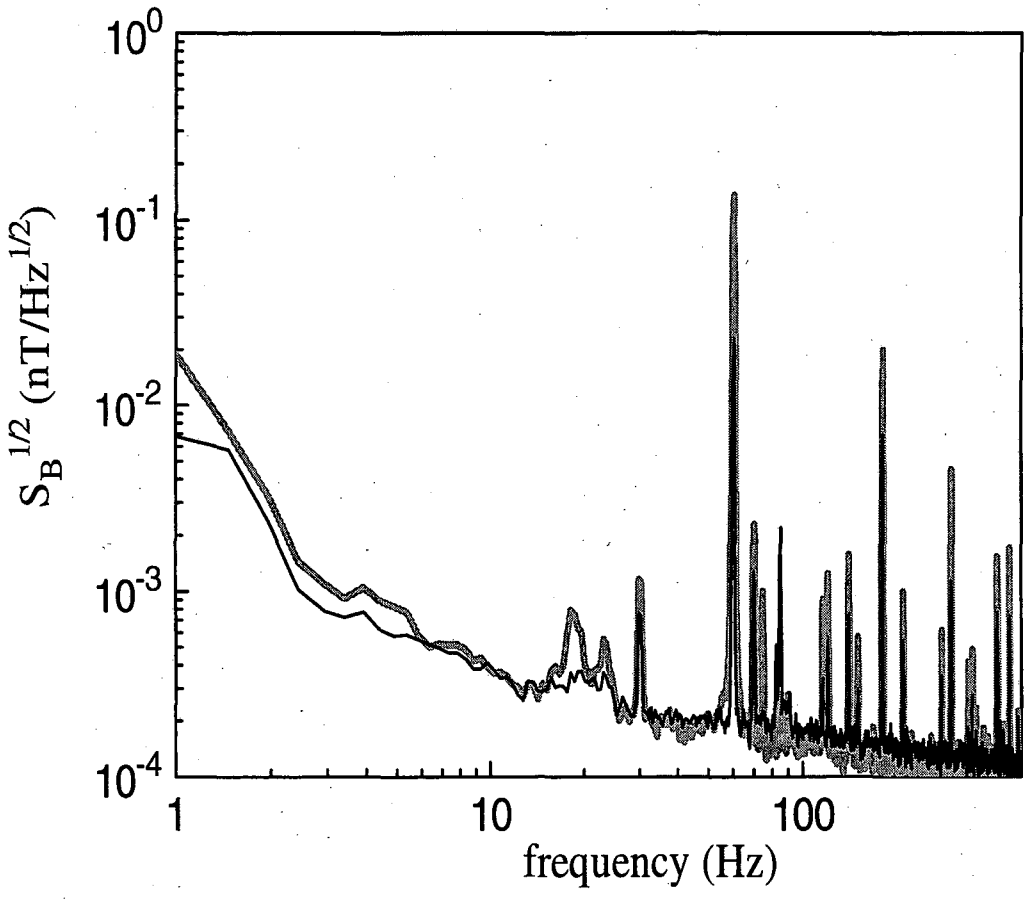

Figure 11.6: Unshielded noise spectra as measured by hardware first-order gradiometer (gray) and second-order gradiometer balanced in software (black).

Chapter 12

MagnetoCardioGraphy in an unshielded environment

To assess the suitability of gradiometers for MCG measurements, we compare the signal-to-noise ratio of our second-order system to that of the hardware second-order device described in section 10.2. We assume that the cardiac signal is produced by a current flowing along the y direction in the plane of the gradiometer. The vertical distances between the current path and the centers of the baselines of the lower and upper gradiometers are r_1 and r_1'; for the hardware second-order gradiometer this distance is r_2. The ratio of the signal-to-noise of the hardware gradiometer to that of the software second-order system is given by

$$\xi_{wire} = \frac{(S/N)^{(2)}_{hardware}}{(S/N)^{(2)}_{software}} = \frac{2d_2^2/r_2^2}{d_1/r_1^2 - d_1/r_1'^2} \times \sqrt{2} \tag{12.1}$$

where d_1 and d_2 are first- and second-order baselines of hardware devices, and the factor of $\sqrt{2}$ is due to the quadratic sum of noise powers when the signals of two first-order gradiometers are subtracted. The baselines of our devices are $d_1 = 4.8$ cm and $d_2 = 3.1$ cm, and we assume $r_1 = 8$ cm, $r_1' = 23$ cm, and $r_2 = 9$ cm for distances relevant for MCG measurements. From these parameter values we estimate $\xi_{wire} = 0.56$. We also estimate the signal-to-noise ratio if the source of the cardiac signal is a magnetic dipole oriented along the y axis separated from gradiometers by the same distances as the current path in

the previous example. In this case, we find

$$\xi_{dipole} = \frac{(S/N)^{(2)}_{hardware}}{(S/N)^{(2)}_{software}} = \frac{4d_2^2/r_2^5}{d_1/r_1^4 - d_1/r_1'^4} \times \sqrt{2}. \tag{12.2}$$

Using $d_1 = 4.8$ cm, $d_2 = 3.1$ cm, $r_1 = 8$ cm, $r_1' = 23$ cm and $r_2 = 9$ cm as in the previous example, we obtain $\xi_{dipole} = 0.8$. Assuming that the MCG signal is the superposition of signals produced by magnetic and current dipoles, the estimates carried out above indicate that one achieves higher signal-to-noise ratios with the software system.

For MCG measurements, signals from the reference gradiometer and the three magnetometers, weighted by balancing coefficients, were added to the signal from the sensing gradiometer. The power line interferences at 60 Hz, 120 Hz and 180 Hz were digitally filtered by third-order elliptic notch filters centered at these frequencies. Additionally, a third-order bandpass filter was used to limit the bandwidth of the MCG measurements to between 0.3 and 47 Hz. All the SQUIDs were heated above T_c and slowly cooled down to 77 K immediately before the MCG measurements.

For MCG recordings healthy human subjects were located on their back underneath the tail of the biomagnetic dewar. The vertical distance between the chest and the tail of the dewar was of the order of 1 cm. Referring to the coordinate system in Fig. 11.1, the position of the subject relative to the dewar was adjusted in the x-y plane to maximize the height of the QRS peak in an MCG signal. The MCG data were recorded in real time. We also had the option of saving raw data from all five channels in a file and analyzing it off-line to look for an improvement in the signal-to-noise ratio. We used identical software algorithms for on- and off-line analysis; the same software had been used previously with axial electronic gradiometers [74].

Figure 12.1 shows the results of our MCG measurements in the particularly harsh magnetic environment created by the operation of an optical trap at about 0.5 Hz in a neighboring laboratory. The noise signal is present in all three reference channels with a maximum peak-to-peak amplitude in the x channel (upper trace) of about 10 nT. The hardware gradiometer attenuates this signal by a factor of about 300. The formation of the second-order gradiometer and the common mode field cancellation eliminates the interfering signal very effectively, and recovers the heart signal (lower trace). This unaveraged signal shown in Fig. 12.2 distinctly shows the QRS peak followed by a small T wave. The signal-to-noise ratio was further improved by averaging, using an electrocardiogram as a trigger.

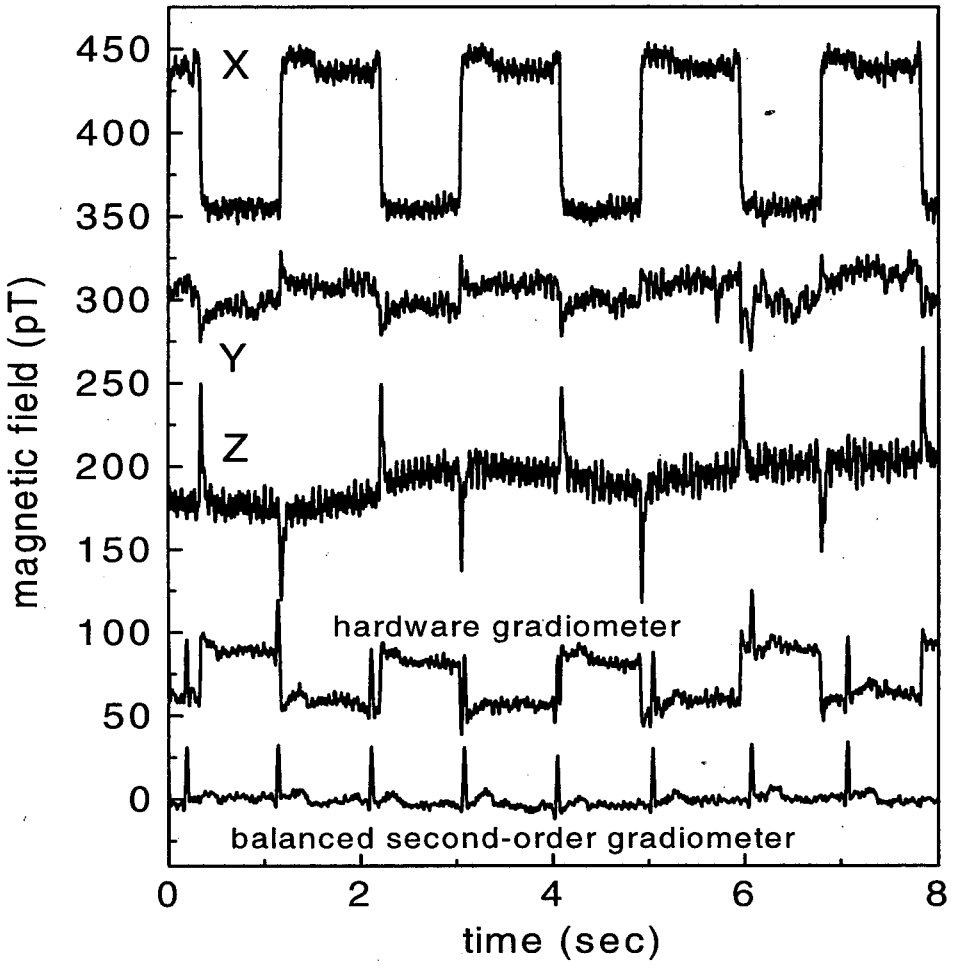

Figure 12.1: Measurement of magnetocardiogram in an unshielded environment in the presence of a 10 nT interfering signal. Signals from x, y and z references are divided by 100. Bandwidth 0.3-47 Hz, notch filters at 60 and 180 Hz, no averaging.

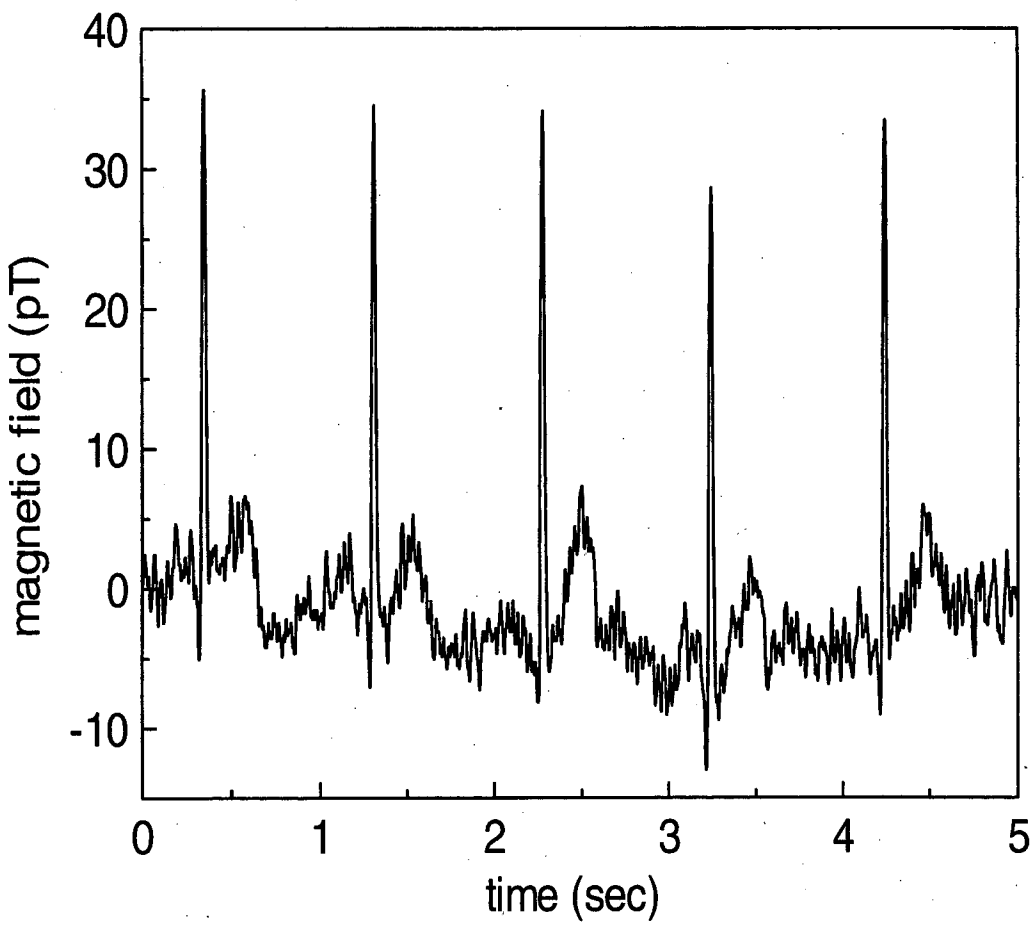

Figure 12.2: Unshielded magnetocardiogram detected in 0.3-47 Hz bandwidth without averaging.

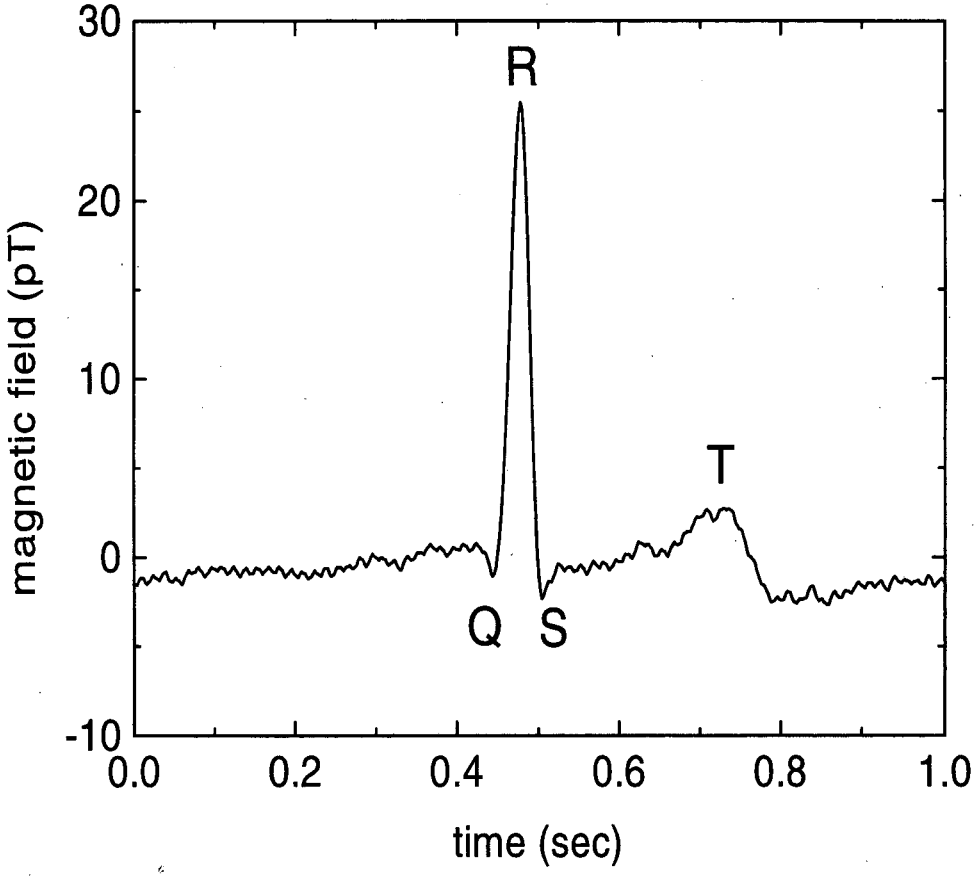

Figure 12.3: Unshielded magnetocardiogram averaged 119 times; bandwidth 0.3-47 Hz.

An example of an MCG averaged 119 times is presented in Fig. 12.3. We note that the magnitude of the QRS peak and the T wave measured tangentially to the chest are smaller than those obtained with axial gradiometers.

Chapter 13

Conclusions and future directions

We have introduced long-baseline hardware gradiometers that can be used as the front-end of HTS biomagnetic systems to perform initial rejection of ambient noise, thereby reducing the demand for high slew rate, linearity and dynamic range of the flux-locked electronics. Further improvements in balance in a multichannel system are achieved electronically or in software. This is a highly successful approach to the design of practical biomagnetic systems, which has been widely used in LTS technology [52].

Our hardware gradiometer is the single most important element in the system, allowing us to utilize a variety of techniques for higher-order gradiometer formation developed for LTS gradiometers. The flux transformer patterned in a single layer of YBaCuO is a simple device and could be made in large quantities with baselines approaching 10 cm using an existing technology. One can use lower quality sintered YBaCuO films on inexpensive polycrystalline substrates [92], thereby reducing the materials cost. We have shown previously [83, 93] that the 1/f flux noise produced in the transformer does not degrade the low frequency noise of the devices because of the inductance mismatch between the SQUID and the pickup loops of the transformer. We have also solved the problem of an excess 1/f noise in single-layer SQUID magnetometers cooled in an Earth's field [81, 82] by making linewidths of the superconducting components equal to 4 μm.

Directly coupled magnetometers are ideally suited for use in gradiometers. They are routinely fabricated at present by a number of groups, and their intrinsic field sensitivities approach those of multilayer devices [94]. The fact that the sensitivity of the magnetometer is not significantly reduced by the presence of the flux transformer, along with the long baselines of first-order gradiometers makes the use of these devices partic-

ularly appealing in HTS technology where sensitivity is at a premium. Enhancement of the sensitivity of the magnetometers can be achieved with the aid of multilayer devices [93, 95, 96] or flux focusing plates. However, these improvements will result in increased complexity, which could negatively impact manufacturability of the gradiometers.

We have also introduced a practical first-order gradiometer in which the flux transformer and magnetometer substrates were permanently assembled in a flip-chip arrangement. Balancing of the device was achieved by trimming the pickup loop - a straightforward procedure that could be eliminated in the manufacturing process by using commercial flip-chip bonders with an alignment accuracy of 1 μm [91]. Flip-chip gradiometers packaged in hermetically-sealed capsules with heaters are self-contained modules that could easily be handled by technicians without specific training. The intrinsic balance of better than 1 part in 100 and a baseline of 48 mm make these devices ideal for use in practical biomagnetic systems.

We built and tested the five channel system for MagnetoCardioGraphy in which two such gradiometers were supplemented by three orthogonally mounted reference magnetometers. The residual response to a uniform magnetic field was reduced to the level of 100 ppm or better using references. The second-order gradiometer was formed in software by subtracting the outputs of two first-derivative devices to reject a first-order gradient applied along the baseline of the device by a factor of 100. With this system, we successfully detected magnetic signals from the human heart in an unshielded environment without averaging.

The approach used in the design and implementation of our system can be extended to higher order systems that utilize arrays of gradiometers with their planes located perpendicularly to the chest or, for a small number of channels, with their planes parallel to the chest to measure the radial component of the field. The bandwidth used in our MCG recordings, 0.3 to 47 Hz, can be extended to 150 or 300 Hz as desirable in clinical cardiology. Additional suppression of power line interference, which is necessary for operation in a wider bandwidth, could be accomplished in systems of the higher order. Alternatively, in a low-order portable system, one can achieve the power line cancellation by using the advanced algorithms for data processing that have already been developed and tested in LTS systems [52, 97]. Our hardware gradiometers can be fabricated with baselines of up to 9 cm, which makes them attractive for application to fetal MCG. [98].

Bibliography

[1] I. Giaver, H. R. Hart, and K. Megerle, "Tunneling into superconductors at temperatures below 1 K", *Phys. Rev.* **126**, 941 (1962).

[2] L. Solymar, *Superconductive Tunnelling and Applications*, Wiley-Interscience, Inc., 1972.

[3] J. Annett, N. Goldenfeld, and A. Leggett, "Expertimental constraints on the pairing state of the cuprate superconductors: an emerging consensus", in *Physical Properties of High Temperature Superconductors*, edited by D. M. Ginsberg, New Jersey, 1996, World Scientific.

[4] D. A. Wollman, D. J. V. Harlingen, D. J. Giapintzakis, and D. M. Ginsberg, "Evidence for $d_{x^2-y^2}$ Pairing from the magnetic field modulation of $YBa_2Cu_3O_{7-x}$-Pb Josephson junctions", *Phys. Rev. Lett.* **74**, 797 (1995).

[5] A. G. Sun, D. A. Gajewski, M. B. Maple, and R. C. Dynes, "Observation of Josephson pair tunneling between a High-T_c cuprate $YBa_2Cu_3O_{7-\delta}$ and a conventional superconductor (Pb)", *Phys. Rev. Lett.* **72**, 2267 (1994).

[6] J. Clarke, "SQUID Fundamentals", in *SQUID Sensors: Fundamentals, Fabrication and Applications, NATO ASI Series*, edited by H. Weinstock, Dordrecht, 1996, Kluwer Academic.

[7] M. Tinkham, *Introduction to Superconductivity*, Robert E. Krieger Publishing Company, Inc., 1975.

[8] J. R. Schrieffer, *Theory of Superconductivity*, Reading, Mass. : Benjamin/Cummings Pub. Co., 1983.

[9] E. L. Wolf, *Principles of Electron Tunneling Spectroscopy*, New York : Oxford University Press, 1985.

[10] A. Barone and G. Paterno, *Physics and Applications of the Josephson Effect*, New York : Wiley, 1982.

[11] J. G. Bednorz and K. A. Mueller, "[Possible high T_c superconductivity in the Ba-La-Cu-O system]", *Z. Phys. B* **64**, 189 (1986).

[12] E. Dagotto, "Correlated electrons in high-temperature superconductors", *Rev. Mod. Phys.* **66**, 763 (1994).

[13] D. J. Scalapino, "The case for $d_{x^2-y^2}$ pairing in cuprate superconductors", *Phys. Rep.* **250**, 329 (1995).

[14] S. Chakravarty, A. Sudbo, P. W. Anderson, and S. Strong, "Interlayer tunneling and gap anisotropy in high-temperature superconductors", *Science* **261**, 337 (1993).

[15] G. Kotliar, "Resonating valence bonds and d-wave superconductivity", *Phys. Rev. B* **37**, 3664 (1988).

[16] D. S. Rokhsar, "Pairing in doped spin liquids: anyon versus d-wave superconductivity", *Phys. Rev. Lett.* **70**, 493 (1993).

[17] R. B. Laughlin, Stanford University preprint, 1994.

[18] D. N. Basov, R. Liang, D. A. Bonn, W. N. Hardy, B. Dabrowski, M. Quijada, D. B. Tanner, J. P. Rice, D. M. Ginsberg, and T. Timusk, "In-plane anisotropy of the penetration depth in $YBa_2Cu_3O_{7-x}$ and $YBa_2Cu_4O_8$ superconductors", *Phys. Rev. Lett.* **74**, 598 (1995).

[19] W. N. Hardy, D. A. Bonn, D. C. Morgan, R. Liang, and K. Zhang, "Precision measurements of the temperature dependence of lambda in $YBa_2Cu_3O_{6.95}$: strong evidence for nodes in the gap function", *Phys. Rev. Lett.* **70**, 3999 (1993).

[20] Z.-X. Shen, D. S. Dessau, B. O. Wells, D. M. King, W. E. Spicer, A. J. Arko, D. Marshall, L. W. Lombardo, A. Kapitulnik, P. Dickinson, S. Doniach, J. diCarlo, A. G. Loeser, and C. H. Park, "Anomalously large gap anisotropy in the a-b plane of $Bi_2Sr_2CaCu_2O_{8+\delta}$", *Phys. Rev. Lett.* **70**, 1553 (1993).

[21] J. A. Martindale, S. E. Barrett, K. E. O'Hara, C. P. Slichter, W. C. Lee, and D. M. Ginsberg, "Magnetic-field dependence of planar copper and oxygen spin-lattice relaxation rates in the superconducting state of $YBa_2Cu_3O_{7-x}$", *Phys. Rev. B* **47**, 9155 (1993).

[22] T. P. Devereaux, D. Einzel, B. Stadlober, R. Hackl, D. H. Leach, and J. J. Neumeier, "Electronic raman scattering in high-T_c superconductors: a probe of $d_{x^2-y^2}$ pairing", *Phys. Rev. Lett.* **72**, 396 (1994).

[23] J. Kane, Q. Chen, K.-W. Ng, and H.-J. Tao, "Observation of a-b plane gap anisotropy in $Bi_2Sr_2CaCu_2O_{8+\delta}$ with a low temperature scanning tunneling microscope", *Phys. Rev. Lett.* **72**, 128 (1994).

[24] K. A. Moler, D. J. Baar, J. S. Urbach, R. Liang, W. N. Hardy, and A. Kapitulnik, "Magnetic field dependence of the density of states of $YBa_2Cu_3O_{6.95}$ as determined from the specific heat", *Phys. Rev. Lett.* **73**, 2744 (1994).

[25] V. B. Geshkenbein, A. I. Larkin, and A. Barone, "Vortices with half magnetic flux quanta in "heavy-fermion" superconductors", *Phys. Rev. B* **36**, 235 (1987).

[26] M. Sigrist and T. M. Rice, "Paramagnetic effect in high T_c superconductors - a hint for d-wave superconductivity", *J. Phys. Soc. Jpn.* **61**, 4283 (1992).

[27] D. A. Wollman, D. J. V. Harlingen, W. C. Lee, D. M. Ginsberg, and A. J. Leggett, "Experimental determination of the superconducting pairing state in YBCO from the phase coherence of YBCO-Pb DC SQUIDs", *Phys. Rev. Lett.* **71**, 2134 (1993).

[28] D. A. Brawner and H. R. Ott, "Evidence for an unconventional superconducting order parameter in $YBa_2Cu_3O_{6.9}$", *Phys. Rev. B* **50**, 6530 (1994).

[29] A. Mathai, Y. Gim, R. C. Black, A. Amar, and F. C. Wellstood, "Experimental proof of a time-reversal-invariant order parameter with a π shift in $YBa_2Cu_3O_{7-\delta}$", *Phys. Rev. Lett.* **74**, 4523 (1995).

[30] C. C. Tsui, J. R. Kirtley, C. C. Chi, L. S. Yu-Jahnes, A. Gupta, T. Shaw, , J. Z. Sun, and M. B. Ketchen, "Pairing symmetry and flux quantization in a tricrystal superconducting ring of $YBa_2Cu_3O_{7-\delta}$", *Phys. Rev. Lett.* **73**, 593 (1994).

[31] J. R. Kirtley, C. C. Tsui, J. Z. Sun, C. C. Chi, L. S. Yu-Jahnes, A. Gupta, M. Rupp, and M. B. Ketchen, "Symmetry of the order parameter in the high-T_c superconductor $YBa_2Cu_3O_{7-\delta}$", *Nature* **19**, 373 (1995).

[32] A. S. Katz, A. G. Sun, R. C. Dynes, and K. Char, "Fabrication of all thin-film $YBa_2Cu_3O_{7-\delta}$/Pb Josephson tunnel junctions", *Appl. Phys. Lett.* **66**, 105 (1995).

[33] J. Lesueur, M. Aprili, A. Goulon, T. J. Horton, and L. Dimoulin, "Evidence for a Josephson tunnel current in all in situ c-$YBa_2Cu_3O_{7-\delta}$/Pb junctions", *Phys. Rev. B* **55**, 3298 (1997).

[34] A. G. Sun, A. Truscott, A. S. Katz, R. C. Dynes, B. W. Voal, and C. Gu, "Direction of tunneling in Pb/I/$YBa_2Cu_3O_{7-\delta}$ tunnel junctions", *Phys. Rev. B* **54**, 6734 (1996).

[35] R. Kleiner, A. S. Katz, A. G. Sun, R. Summer, , D. A. Gajewski, S. H. Han, S. I. Woods, E. Dantsker, B. Chen, K. Char, M. B. Maple, R. C. Dynes, and J. Clarke, "Pair tunneling from c-axis $YBa_2Cu_3O_{7-\delta}$ to Pb: evidence for s-wave component from microwave induced steps", *Phys. Rev. Lett.* **76**, 2161 (1996).

[36] Y. Tanaka, "Josephson effect between s wave and $d_{x^2-y^2}$ wave superconductors", *Phys. Rev. Lett.* **72**, 3871 (1994).

[37] K. A. Kouznetsov, A. G. Sun, B. Chen, A. S. Katz, S. R. Bachcall, J. Clarke, R. C. Dynes, D. A. Gajewski, S. H. Han, M. B. Maple, J. Gianpintzakis, J.-T. Kim, and D. M. Ginsberg, "c-axis Josephson Tunneling between $YBa_2Cu_3O_{7-\delta}$ and Pb: direct evidence for mixed order parameter symmetry in a high-T_c superconductor", *Phys. Rev. Lett.* **79**, 3050 (1997).

[38] L. F. Schneemeyer, J. V. Waszczyk, T. Siegrist, R. B. van Dover, L. W. Rupp, B. Batlogg, and D. W. Murphy, "Superconductivity in $YBa_2Cu_3O_{7-\delta}$ single crystals", *Nature* **328**, 601 (1987).

[39] J. P. Rice, B. G. Pazol, D. M. Ginsberg, T. J. Morgan, and M. B. Weissman, "Growth and processing of single crystal superconducting $YBa_2Cu_3O_{7-\delta}$", *J. Low Temp. Phys.* **72**, 345 (1988).

[40] L. M. Paulius, B. W. Lee, M. B. Maple, and P. K. Tsai, "Preparation and characterization of $Y_{1-x}Pr_xBa_2Cu_3O_{7-\delta}$ single crystals", *Physica C* **230**, 255 (1994).

[41] J. Giapintzakis, D. M. Ginsberg, and P.-D. Han, "A method for obtaining single domain superconducting $YBa_2Cu_3O_{7-\delta}$ single crystals", *J. Low Temp. Phys.* **77**, 155 (1989).

[42] J. Valles, R. C. Dynes, A. M. Cucolo, M. Gurvitch, L. F. Schneemeyer, J. P. Garno, and J. V. Waszcyak, "Electron tunneling into single crystals of $YBa_2Cu_3O_{7-\delta}$", *Phys. Rev. B* **44**, 11986 (1991).

[43] D. J. V. Harlingen, "Phase sensitive tests of the symmetry of the pairing state in the high-temperature superconductors - evidence for $d_{x^2-y^2}$ symmetry", *Rev. Mod. Phys.* **67**, 515 (1995).

[44] J. H. Xu, J. H. Miller, and C. S. Ting, "π-vortex state in a long $0-\pi$ junction", *Phys. Rev. B* **51**, 11958 (1995).

[45] J. R. Kirtley, K. A. Moler, and D. J. Scalapino, "Spontaneous flux and magnetic-interference patterns in 0-π Josephson junctions", *Phys. Rev. B* **56**, 886 (1997).

[46] D. F. Agterberg and M. Sigrist, "Asymmetric magnetic field interference patterns in $0-\pi$ Josephson junction", *Phys. Rev. Lett.* **80**, 2689 (1998).

[47] H. H. Zappe, "Determination of the current density distribution in Josephson tunnel junctions", *Phys. Rev. B* **11**, 2535 (1975).

[48] S. R. Bahcall, "Boundary effects and the order parameter symmetry of high-T_c superconductors", *Phys. Rev. Lett.* **76**, 3634 (1996).

[49] M. Sigrist, K. Kuboki, P. A. Lee, A. J. Millis, and T. M. Rice, "Influence of twin boundaries on Josephson junctions between high-temperature and Conventional Superconductors", *Phys. Rev. B* **53**, 2835 (1996).

[50] S. J. Williamson and Kaufman, "Biomagnetism", *J. Magnetism and Magn. Mat.* **22**, 129 (1981).

[51] M. Hämäläinen, R. Hari, R. Ilmoniemi, J. Knuutila, and O. Lounasmaa, "Magnetoencephalography-theory, instrumentation, and applications to noninvasive studies of the working human brain", *Rev. Mod. Phys.* **65**, 413 (1993).

[52] J. Vrba, "SQUID Gradiometers in real environments", in *SQUID Sensors: Fundamentals, Fabrication and Applications, NATO ASI Series*, edited by H. Weinstock, Dordrecht, 1996, Kluwer Academic.

[53] J. E. Zimmerman and N. V. Frederick, "Miniature ultrasensitive superconducting magnetic gradiometer and its use in cardiography and other applications", *Appl. Phys. Lett.* **19**, 16 (1971).

[54] M. B. Ketchen, W. M. Goubau, J. Clarke, and G. B. Donaldson, "Superconducting thin-film gradiometer", *J. Appl. Phys.* **49**, 4111 (1978).

[55] D. Drung, "The PTB 83-SQUID system for biomagnetic applications in a clinic", *IEEE Trans. Appl. Supercond.* **5**, 2112 (1995).

[56] S. Knappe, D. Drung, T. Schurig, H. Koch, M. Klinger, and J. Hinken, "A planar $YBa_2Cu_3O_{7-x}$ gradiometer at 77 K", *Cryogenics* **32**, 881 (1992).

[57] V. Zakosarenko, F. Schmidl, H. Schneidewind, L. Dorrer, and P. Seidel, "Thin-film DC SQUID gradiometer using a single $YBa_2Cu_3O_{7-x}$ layer", *Appl. Phys. Lett.* **65**, 779 (1994).

[58] R. Schmidl, S. Wunderlich, L. Dörrer, H. Specht, S. Linzen, H. Schneidewind, and P. Seidel, *IEEE Trans. Appl. Supercond.* **7**, 2756 (1997).

[59] V. Schultze, R. Stolz, R. Ijsselsteijn, V. Zakosarenko, , L. Fritzsch, F. Thurm, E. Il'ichev, and H.-G. Meyer, "High-T_c DC-SQUID system for nondestructive evaluation", *IEEE Trans. Appl. Supercond.* **7**, 3473 (1997).

[60] S.-G. Lee, Y. Hwang, B.-C. Nam, J.-T. Kim, and I.-S. Kim, "Direct-coupled second-order superconducting quantum interference device gradiometer from single layer of high temperature superconductor", *Appl. Phys. Lett.* **73**, 2345 (1998).

[61] W. Eidelloth, B. Oh, R. P. Robertazzi, W. J. Gallagher, and R. H. Koch, "$YBa_2Cu_3O_{7-\delta}$ thin-film gradiometers: fabrication and performance", *Appl. Phys. Lett.* **59**, 3473 (1991).

[62] M. N. Keene, S. W. Goodyear, N. G. Chew, R. G. Humphreys, J. S. Satchell, J. A. Edwards, and K. Lander, "Low-noise $YBa_2Cu_3O_{7-\delta}$-$PrBa_2Cu_3O_7$ multiturn flux transformers", *Appl. Phys. Lett.* **64**, 366 (1994).

[63] M. N. Keene, N. J. Exon, R. G. Humphreys, and N. G. Chew, "The influence of ambient magnetic environments on high-T_c superconducting quantum interference device gradiometers", *J. Appl. Phys.* **79**, 8783 (1996).

[64] G. M. Daalmans, "HTS DC SQUIDs for practical applications", *Appl. Supercond.* **3**, 399 (1995).

[65] L. R. Bär, G. M. Daalmans, K. H. Barthel, L. Ferchland, M. Selent, M. Kühnl, , and D. Uhl, "Single-layer and integrated YBCO gradiometer coupled SQUIDs", *Supercond. Sci. Technol.* **9**, A87 (1996).

[66] M. I. Faley, U. Poppe, K. Uran, H.-J. Krause, H. Soltner, R. Hohmann, D. Lomparski, R. Kutzner, R. Wordenweber, H. Bousack, A. I. Braginski, V. Y. Slobodchikov, A. V. Gapelyuk, V. V. Khanin, and Y. V. Maslennikov, "Dc-SQUID magnetometers and gradiometers on the basis of quasiplanar ramp-type Josephson junctions", *IEEE Trans. Appl. Supercond.* **7**, 3702 (1997).

[67] Y. J. Tian, S. Linzen, F. Schmidl, L. Dörrer, R. Weidl, , and P. Seidel, "High-T_c directly coupled direct current SQUID gradiometer with flip-chip flux transformer", *Appl. Phys. Lett.* **74**, 1302 (1999).

[68] R. H. Koch, J. R. Rozen, J. Z. Sun, and W. J. Gallagher, "Three SQUID gradiometer", *Appl. Phys. Lett.* **63**, 403 (1993).

[69] Y. Tarvin, Y. Zhang, M. Mück, A. I. Braginski, and C. Heiden, "$YBa_2Cu_3O_{7-\delta}$ thin films SQUID gradiometer for biomagnetic measurements", *Appl. Phys. Lett.* **62**, 1824 (1993).

[70] Y. Tarvin, Y. Zhang, W. Wolf, and A. I. Braginski, "A second-order SQUID gradiometer operating at 77 K", *Supercond. Sci. Technol.* **7**, 265 (1994).

[71] H. J. M. ter Brake, N. Janssen, J. Flokstra, D. Vedelhius, and H. Rogalla, "Multichannel heart scanner based on high-T_c SQUIDs", *IEEE Trans. Appl. Supercond.* **7**, 2545 (1997).

[72] J. Borgmann, P. David, G. Ockenfuss, R. Otto, J. Schubert, W. Zander, and A. I. Braginski, "Electronic high-temperature radio frequency superconducting quantum

interference device gradiometers for unshielded environment", *Rev. Sci. Instrum.* **68**, 2730 (1997).

[73] J. Borgmann, P. David, H.-J. Krause, R. Otto, and A. I. Braginski, "Compensation techniques for high-temperature superconducting quantum interference device gradiometers operating in unshielded environment", *Rev. Sci. Instrum.* **68**, 3082 (1997).

[74] J. Borgmann, A. P. Rijpma, H. J. M. ter Brake, H. Rogalla, and P. David, "Highly balanced gradiometer systems based on HTS-SQUIDs for the use in magnetically unshielded environment", *IEEE Trans. Appl. Supercond.* **9**, 3680 (1999).

[75] D. F. He, H.-J. Krause, Y. Zhang, M. Bick, H. Soltner, N. Wolters, W. Wolf, and H. Bousack, "HTS SQUID magnetometer with SQUID vector reference for operation in unshielded environment", *IEEE Trans. Appl. Supercond.* **9**, 3684 (1999).

[76] Y. Zhang, G. Panaitov, S. G. Wang, N. Walters, R. Otto, J. Schubert, W. Zander, H.-J. Krause, and H. Bousack, "An HTS SQUID gradiometer using superconducting coplanar resonators for operation in unshielded environment", (1999), (preprint).

[77] E. Dantsker, O. M. Fröhlich, S. Tanaka, K. Kouznetsov, J. Clarke, Z. Lu, V. Matijasevic, and K. Char, "High-T_c superconducting gradiometer with a long base line asymmetric flux transformer", *Appl. Phys. Lett.* **71**, 1712 (1997).

[78] A. Kittel, K. A. Kouznetsov, R. McDermott, B. Oh, and J. Clarke, "High-T_c superconducting second-order gradiometer", *Appl. Phys. Lett.* **73**, 2197 (1998).

[79] K. A. Kouznetsov, J. Borgmann, and J. Clarke, "High-T_c second-order gradiometer for magnetocardiography in an unshielded environment", *Appl. Phys. Lett.* **75**, 1979 (1999).

[80] J. R. Clem, private communication, 1999.

[81] E. Dantsker, S. Tanaka, P.-A. Nilsson, R. Kleiner, and J. Clarke, "Reduction of 1/f noise in high-T_c dc superconducting quantum interference devices cooled in an ambient magnetic field", *Appl. Phys. Lett.* **69**, 4099 (1996).

[82] E. Dantsker, S. Tanaka, and J. Clarke, "High-T_c SQUIDs with slots or holes: low 1/f noise in ambient magnetic fields", *Appl. Phys. Lett.* **70**, 2037 (1997).

[83] M. J. Ferrari, J. J. Kingston, F. C. Wellstood, and J. Clarke, "Flux noise from superconducting $YBa_2Cu_3O_{7-x}$ flux transformers", *Appl. Phys. Lett.* **58**, 1106 (1991).

[84] M. J. Ferrari, M. Johnson, F. C. Wellstood, J. J. Kingston, T. Shaw, and J. Clarke, "Magnetic flux noise in copper oxide superconductors", *J. Low Temp. Phys.* **94**, 15 (1994).

[85] H.-M. Cho, R. McDermott, B. Oh, K. A. Kouznetsov, A. Kittel, J. H. M. Jr., and J. Clarke, "Low-frequency noise in field-cooled, directly coupled magnetometers", *IEEE Trans. Appl. Supercond.* **9**, 3294 (1999).

[86] M. B. Ketchen and J. M. Jaycox, "Ultra-low noise tunnel junction dc SQUID with tightly coupled planar input coil", *Appl. Phys. Lett.* **40**, 736 (1982).

[87] M. B. Ketchen, W. J. Gallagher, A. W. Kleinsasser, S. Murphy, and J. R. Clem, in *Proceedings of SQUID'85*, edited by H. D. Hahlbohm and H. Lübbig, Berlin, 1985, Walter de Gruyter.

[88] R. Cantor, "DC SQUIDs: Design, Optimization, and Practical Applications", in *SQUID Sensors: Fundamentals, Fabrication and Applications, NATO ASI Series*, edited by H. Weinstock, Dordrecht, 1996, Kluwer Academic.

[89] J. Zimmermann, "SQUID instruments and shielding for low-level magnetic measurements", *J. Appl. Phys.* **48**, 702 (1977).

[90] A. N. Matlashov, V. P. Koshlelets, P. V. Kalashnikov, Y. E. Zhuravlev, V. Y. Slobodchikov, S. A. Kovtonyuk, , and L. V. Flippenko, "High sensitive magnetometers and gradiometers based on DC SQUIDs with flux focuser", *IEEE Trans. Magn.* **MAG-27**, 2963 (1991).

[91] Research Devices Inc., Piscataway, NJ.

[92] T. W. Button, N. M. Alford, F. Wellhofer, F. Shields, T. C. Abell, and F. S. Day, "The Processing and Properties of High-T_c thick films", *IEEE Trans. Magn.* **MAG-27**, 1434 (1991).

[93] D. Koelle, A. H. Miklich, E. Dantsker, F. Ludwig, D. T. Nemeth, J. Clarke, W. Ruby, and K. Char, "High performance DC SQUID magnetometers with single layer $YBa_2Cu_3O_{7-x}$ flux transformers", *Appl. Phys. Lett.* **63**, 3630 (1993).

ERNEST ORLANDO LAWRENCE BERKELEY NATIONAL LABORATORY
ONE CYCLOTRON ROAD | BERKELEY, CALIFORNIA 94720

Prepared for the U.S. Department of Energy under Contract No. DE-AC03-76SF00098

ABY574
LBL Libraries